Modified Inherent Strain Method for Predicting Residual Deformation in Metal Additive Manufacturing

by

Xuan Liang

B.S., Tsinghua University, 2011

M.S., Tsinghua University, 2015

Submitted to the Graduate Faculty of the

Swanson School of Engineering in partial fulfillment

of the requirements for the degree of

Doctor of Philosophy

University of Pittsburgh

2020

UNIVERSITY OF PITTSBURGH

SWANSON SCHOOL OF ENGINEERING

This dissertation was presented

by

Xuan Liang

It was defended on

June 18, 2020

and approved by

Wei Xiong, Ph.D., Assistant Professor, Department of Mechanical Engineering and Materials Science

Xiayun Zhao, Ph.D., Assistant Professor, Department of Mechanical Engineering and Materials Science

Kevin P. Chen, Ph.D., Paul E. Lego Chair Professor, Department of Electrical and Computer Engineering

Dissertation Director: Albert C. To, Ph.D., William Kepler Whiteford Professor, Department of Mechanical Engineering and Materials Science

Modified Inherent Strain Method for Predicting Residual Deformation in Metal Additive Manufacturing

Xuan Liang, Ph.D.

University of Pittsburgh, 2020

Additive manufacturing (AM) of metal components has seen rapid development in the past decade, since arbitrarily complex geometries can be manufactured by this technology. Due to intensive heat input in the laser-assisted AM process, large thermal strain is induced and hence results in significant residual stress and deformation in the metal components. To achieve efficient simulation for metal printing process, the inherent strain method (ISM) is ideal for this purpose, but has not been well developed for metal AM parts yet.

In this dissertation, a modified inherent strain method (MISM) is proposed to estimate the inherent strains from detailed process simulation. The obtained inherent strains are employed in a layer-by-layer static equilibrium analysis to simulate residual distortion of the AM part efficiently. To validate the proposed method, single-walled builds deposited by directed energy deposition (DED) process are studied first. The MISM is demonstrated to be accurate by comparing with full-scale detailed process simulation and experimental results.

Meanwhile, the MISM is adapted to powder bed fusion (PBF) process to enable efficient yet accurate prediction for residual stress and deformation of large components. The proposed method allows for calculation of inherent strains accurately based on a small-scale simulation of a small representative volume. The extracted mean inherent strains are applied to a part-scale model layer-by-layer to simulate accumulation of residual deformation. Accuracy of the proposed method

for large components is validated by comparison with experimental results, while excellent computational efficiency is also shown.

As further applications, the MISM is extended to deal with efficient simulation for residual deformation of thin-walled lattice support structures with different volume densities. To achieve this goal, asymptotic homogenization is employed to obtain the homogenized inherent strains and elastic modulus given the specific laser scanning strategy and process parameters for fabricating those thin-walled lattice support structures. Accuracy of the homogenization-based layer-by-layer simulation have been validated by experiments. Moreover, the enhanced layer lumping method (ELLM) is developed to further accelerate the layer-by-layer simulation to the largest extent for metal builds produced by PBF. By using tuned material property models, good accuracy can be ensured while directly lumping the equivalent layers in the layer-wise simulation.

Table of Contents

List of Tables

List of Figures

Preface

Five years ago, when I first arrived at the University of Pittsburgh, I never expected the experience of pursuing my doctoral degree would be so unforgettable. I feel very lucky to reach the end of my study successfully. I would like to thank many people who give generous support to me in the completion of this dissertation.

First, I would like to give my sincere gratitude to my advisor, Prof. Albert C. To for his insightful guidance and full support for the completion of my dissertation. I got a lot of benefit from the discussions with Prof. To in the past years. Moreover, He encouraged me to attend many academic conferences to practice my presenting and communicating skills. These experiences are extremely unforgettable in my life.

Second, I would like to say sincere thanks to my committee members, Prof. Wei Xiong, Prof. Xiayun Zhao, and Prof. Kevin P. Chen, for their serving on my committee regardless of a tight time schedule. They gave a lot of insightful comments on my research work. Their valuable suggestions have greatly improved the quality of my dissertation.

Third, I also would like to thank my colleagues in the computational mechanics group for their kind collaboration and patient help. I would like to give my gratitude to many past and current members: Dr. Pu Zhang, Dr. Qingcheng Yang, Lin Cheng, Qian Chen, Wen Dong, Hao Deng, Shawn Hinnebusch, Dr. Hai T. Tran, and among others, for generous sharing of their expertise. I also want to thank Ran Zou and Shuo Li in Prof. Kevin P. Chen's group for their nice collaboration. Moreover, I would like to thank Brandon Blasko and Andrew Holmes in the Swanson Center for Product Innovation of University of Pittsburgh for their help in the experiments.

In particular, I would like to give acknowledgement to funding support from Army SBIR, and technical support from commercial companies including ANSYS, Materials Science Corporation (MSC) and Oberg Industry, etc. Specifically, I would like to thank my collaborators, Jason Oskin and John Lemon from Oberg Inc., for their help in some of the experiments involved in this dissertation.

At last, I want to owe my deepest and sincere gratitude to my wife and my parents. Without their endless support and encouragement, it would not be possible for me to stick to the end and complete my dissertation. Your love and support give me the largest power and help me move forward with courage in my life.

1.0 Introduction

The primary goal of this dissertation is to propose an efficient simulation method that can predict residual stress and deformation of large metal components fabricated by the AM process. The main focus of the simulation method lies in the thermal and mechanical analysis involving elastic and elastoplastic mechanics. As a further application, efficient simulation of thin-walled metal lattice structures is also studied in order to show the excellent performance and large potential of the proposed method in real practice. The motivation, background and research objective are presented in this chapter.

1.1 Metal Additive Manufacturing (AM)

Restricted by its subtractive nature, it is difficult to employ machining techniques to produce metal parts with complex geometries, especially those with internal features. However, the demand for complex-shaped parts has increased rapidly since metal parts consisted of microscopic structures (e.g. cellular structures) have been shown to have excellent mechanical performance under certain conditions [1, 2]. Therefore, additive manufacturing (AM) has received much interest lately and is considered an important technique for fabricating complex-shaped workpieces [3, 4]. In modern AM processes, the CAD model of a part is sliced into many thin layers, where each layer is “printed” successively in a bottom-up manner [5-10]. In this way, any complex geometry can be produced by AM. For example, AM has been employed to print complex structures [2, 11] designed by topology optimization [11-16].

On the one hand, powder bed fusion (PBF) process is currently the most popular AM process for manufacturing complex metal components. For example, selective laser melting (SLM), direct metal laser sintering (DMLS) and electron beam melting (EBM) are powder bed based. A metal part is sliced into planar layers and then built from bottom up in a powder bed. Thin layers of metal powder are spread over a clamped build plate by a moving roller or spreader as shown in Figure 1.1. Each thin layer is fused by laser or electric beam via a micro-welding process [17] in a pass-by-pass manner following the prescribed scan paths and patterns. Metal powder fusion only occurs in those areas where a raster motion of the laser or electric beam heat source involves. Rapid melting and solidification of metal powders occurs in the scan tracks, forming the final metal components.

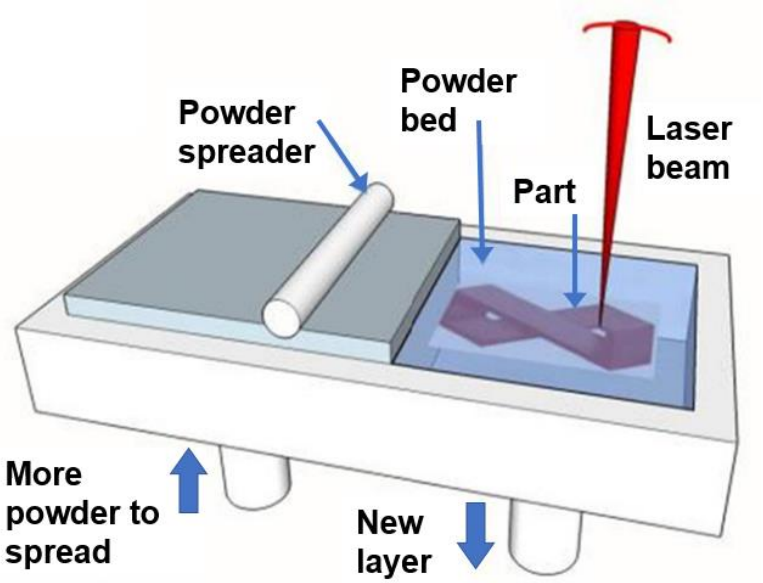

Figure 1.1 Typical Schematic Diagram of PBF Drocess Using Laser Heat Source [4]

On the other hand, directed energy deposition (DED) is the other category of metal AM processes. It is more suitable for making repairs, adding features to an existing component, or even

making parts with different materials during the same build. A representative DED process is the LENS (Laser Engineered Net Shaping) [18-20], which is based on feeding powder into the melt pool created by a high energy laser beam. Figure 1.1 illustrates an example stemming from the use of LENS that will be employed in this dissertation.

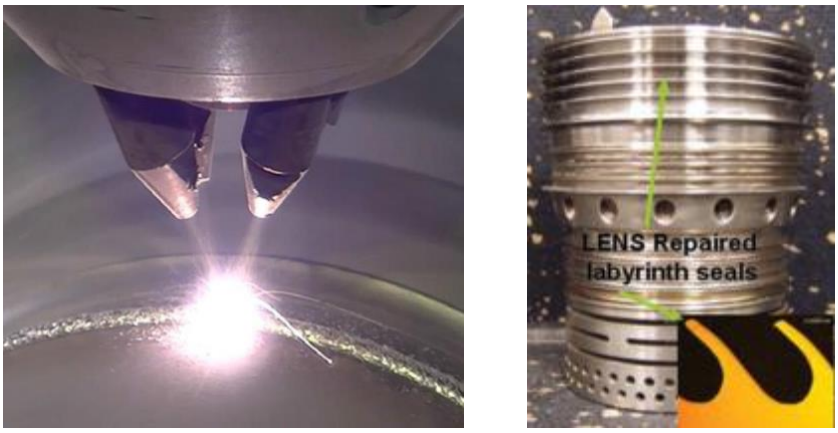

(a) (b)

Figure 1.2 Successful Repair Case Studies Using the (a) Optomec LENS System: (b) Inconel 718 Compressor Seal [18]

1.2 Thermomechanical Simulation for Metal AM

At the macroscopic scale, different metal AM processes that employ a high-energy heating source are generally based on similar physical processes involving melting and solidification of metal. Hence in a typical metal AM process, large temperature gradient and high cooling rate occurs due to intensive heat input and large local energy density, which consequently lead to large thermal strains and residual stress or distortion in an AM metal part [21-23].

Unless post stress relief is performed, removal of substrate or support structures after printing would result in further deformation of the AM part and residual stress and strain would redistribute [24]. In order to predict the residual distortion and stress introduced into the part by an AM process, since the physical process of AM has some commonalities with the metal welding phenomenon, some simulation methods focused on the metal welding problem have been extended for metal AM processes [25-29]. Numerical approaches employing the finite element analysis (FEA) have been implemented [29-33]. Based on the simulations, optimization of laser scanning strategies, build-up directions, or design of support structures could be further investigated [34].

Part-scale AM process simulation to compute residual stress and distortion is very time-consuming since it is a long time-scale problem involving transient heat transfer, non-linear mechanical deformation, and addition of large amount of materials [27-29]. Depending on the material under consideration, either a fully coupled or decoupled thermomechanical analysis can be employed. For example, in a decoupled analysis, the thermal analysis is first performed to acquire the temperature distribution at each time step, followed by assigning the obtained thermal load as temperature field at the corresponding step in the mechanical analysis [35, 36]. Obviously, the entire process simulation becomes increasingly time-consuming as large amount of materials are being deposited, and as a result, the size of the modeled part or the number of depositing layers is severely limited. The required simulation time ranges from several hours to days, or even weeks. In order to enable practical AM process simulation, the simulation time must be reduced radically.

1.3 Inherent Strain Method (ISM)

Decades ago, the inherent strain method (ISM) [37-41] was developed and established to enable fast estimation of residual distortion/stress in metal welding. Both simulation and experimental results validate the accuracy and efficiency of the ISM for predicting residual distortion/stress of simple metal welding. Another computationally efficient method inspired by the inherent strain theory is the method of applied plastic strain [42, 43]. It utilizes 2D elastoplastic simulation to calculate the plastic strain and then apply it as an equivalent mechanical load to the 3D model to evaluate residual distortion/stress. Both the inherent strain and applied plastic strain method are capable of significantly reducing the computational cost of the thermomechanical simulation [43, 44]. However, the physical process of AM is much more complicated compared with simple metal welding. Attempts to directly apply the inherent strain or the applied plastic strain method to the AM process have failed to obtain accurate residual distortion or stress of builds with multiple deposition layers. In recent years, some other approaches based on the inherent strain theory have been developed, and the computed inherent strain is imposed onto a macro-scale model to obtain mechanical deformation [45-47]. This method is easy to implement and computationally fast, but it is a challenge to achieve good accuracy in predicting residual distortion at part scale [48].

1.4 Research Objectives

1.4.1 Establishment of the MISM for DED Process

Detailed thermomechanical simulation of powder-fed LENS process is numerically implemented and validated first as the basic knowledge for AM process. Then the MISM is proposed to estimate the inherent strains accurately from detailed AM process simulation for fast residual distortion simulation of single-walled structures produced by the representative DED process in LENS. These singled-walled structures considered here are composed of laser scan lines deposited on top of each other but not on their sides, except at the connections where two walls join with each other. Obviously, the purpose of considering only these geometrically simple structures is to simplify the problem and model formulation for fast residual distortion prediction. A challenge of doing the same for complex-topological structures is expected to build on top of the model proposed in this dissertation. As a natural extension, the concept of mean inherent strain vector will be proposed which will be extracted from the two-layer and three-layer line deposition models. Numerical examples will demonstrate the mean inherent strain can be applied to simple wall depositions containing more layers to accurately predict residual deformation much faster. A small-scale simulation model is further proposed to extract the mean inherent strain for applying to different single-walled DED parts and predicting residual deformation efficiently.

1.4.2 MISM Adapted to PBF Process

The MISM will be adapted to the PBF DMLS process and employed to predict the residual distortion of the large and complex metal components efficiently. The MISM will be adapted

carefully to the specific physical phenomena in the DMLS process. The detailed procedure of extracting the inherent strain based on small-scale thermomechanical simulation will be demonstrated. Also, the way that the mean inherent strain vector is obtained and assigned to different large-scale builds will be explained. Numerical examples will be provided to validate the proposed method by comparing its prediction with experimental measurement of DMLS double cantilever beam and the complex canonical component. Computational efficiency of the proposed method will also be shown.

1.4.3 Homogenization-Based MISM for Thin-walled Lattice Structures

The effective inherent strains for thin-walled lattice support structures will be figured out based on asymptotic homogenization given the specific process parameter and laser scanning strategy. Meanwhile, the effective mechanical property like elastic modulus of the lattice support structured of different volume densities will also be obtained. The homogenized inherent strains and mechanical properties will be fully employed to enable efficient analysis in the layer-by-layer simulation for large components with support structures. This novel idea will adapt the proposed MISM to more scenarios such as other types of lattice support structures involved in the PBF fabricating process.

1.4.4 Enhanced Layer Lumping Lethod (ELLM) for Simulation Accelerating

The enhanced layer lumping method (ELLM) is developed in order to accelerate the layer-wise simulation to the largest extent, while ensuring good simulation prediction at the same time for the large metal components produced by PBF. The residual stress/strain evolution history due

to layer-wise material addition in the meso-scale modeling. Considering the observed evolution feature, tuned material property models (MPMs) are proposed to control the stress level when many equivalent layers are activated and deformed simultaneously in the layer-by-layer simulation. The simulation results obtained through the ELLM with tuned MPMs are validated by comparison to experimental results. The computational times for different ELLM cases are also shown, which indicates the greatly accelerated simulation by the proposed method.

2.0 Modified Inherent Strain Method (MISM) for DED Process

2.1 Governing Equations of Thermomechanical Simulation

Since the inherent strains have to be extracted based on the history of mechanical strain, a detailed thermomechanical simulation for the metal AM has been fully developed, and the key governing equations are briefly reviewed below. In order to ensure accuracy of the extracted inherent strains, the detailed process model has to satisfy a few characteristics. For example, it should be able to capture the exact peak temperature of any concerned material point in the AM process, since it will influence the mechanical strains of the intermediate state. Therefore, a reasonable heat source model should be employed to capture the shape of the melt pool. Meanwhile, sufficient number of load steps should be used to simulate the detailed laser scanning path. Otherwise, the temperature distribution, especially the far-field temperature, obtained by the thermal analysis may not match the experimental measurement. Moreover, the effects of the evolving mechanical boundaries on the inherent strains extracted cannot be fully considered without enough simulation steps. The number of load steps should be determined based on element size and physical parameters of the heat source such as the laser penetration depth. New elements in each thin layer are activated in each load step to simulate the material depositing process. Some elements are possibly not activated if coarse load steps are employed in the detailed process simulation. To avoid this problem, the number of load steps is first estimated roughly by dividing the deposition layer length by the radius of the laser beam. Then denser load steps have to be employed to ensure that all the elements in a layer will be activated step by step. This is general

rule for considering the least number of load steps are needed to ensure good accuracy for the detailed process model.

2.1.1 Thermal Analysis

Assume a Lagrangian frame Ω and a material point located by $\boldsymbol{r}(\boldsymbol{r} \in \Omega)$ as the reference. Given thermal energy balance at time t, the governing equation can be formulated as follows [36]:

$$\rho C_p \frac{dT(\boldsymbol{r},t)}{dt} = -\nabla \cdot \boldsymbol{q}(\boldsymbol{r},t) + Q(\boldsymbol{r},t), \boldsymbol{r} \in \Omega \tag{2.1}$$

where ρ denotes the material density; C_p denotes the specific heat capacity; T denotes the temperature field; $\boldsymbol{q}$ denotes the thermal flux vector and Q denotes the internal heat source.

Expression of the thermal flux vector $\boldsymbol{q}$ can be written as:

$$\boldsymbol{q} = -k\nabla T \tag{2.2}$$

where k is the thermal conductivity coefficient and ∇T indicates the temperature change. Material properties such as thermal conductivity coefficient and specific heat capacity are usually temperature dependent.

The internal heat source Q exerts a significant influence on the thermal modeling of the AM process, since the heat input is the fundamental cause of the residual distortion and stress. Different mathematical models have been proposed in the literature [49-52] to construct equations of the heat source. The difference between those models is generally different number of degrees of freedom. Among the heat source models, the double ellipsoidal model [53] has been widely used [33, 35, 54-56], which may be the most sophisticated model proposed so far. The pattern of the heat generation rate is assumed to be Gaussian. However, those equations are generally proposed under a specific condition and should be modified to match the actual size of the melt

pool. Acceptable ways for comparing parameter fitting of the heat source model in order to match the geometry in the micrograph can be found in the references [55, 56].

For the thermal analysis, the initial condition regarding the temperature is assigned as follows:

$$T(\boldsymbol{r}, 0) = T_0(\boldsymbol{r}, 0), \boldsymbol{r} \in \Omega \tag{2.3}$$

Equations corresponding to different types of thermal boundary conditions in the AM process are generally classified into three categories:

$$T = \bar{T},\ \boldsymbol{r} \in \Gamma_D^T \tag{2.4}$$

$$-k\nabla T \cdot \boldsymbol{n} = \bar{q},\ \boldsymbol{r} \in \Gamma_N^T \tag{2.5}$$

$$-k\nabla T \cdot \boldsymbol{n} = h(T - T_a), \boldsymbol{r} \in \Gamma_R^T \tag{2.6}$$

Equation (2.4) gives the Dirichlet boundary condition on the boundary Γ_D^T where the temperature field is prescribed as $\bar{T}$. Equation (2.5) gives the Neumann boundary condition on the boundary Γ_N^T, whereas the heat flux is defined with the normal vector $\boldsymbol{n}$ to Γ_N^T; Equation (2.6) shows the Robin boundary condition where the surface heat convection with the convection coefficient *h* between the ambient temperature T_a and the surface temperature T is applied on Γ_R^T. There is no overlap among Γ_D^T, $\Gamma_N^T$and Γ_R^T and $\Gamma_D^T \cup \Gamma_N^T \cup \Gamma_R^T = \partial\Omega^T$.

2.1.2 Mechanical Analysis

Quasi-static mechanical analysis is generally implemented to calculate the mechanical response such as the residual distortion and stress for AM builds. The temperature history obtained by the abovementioned thermal analysis is applied to the model as an external load and boundary

constraint. The governing equation corresponding to the quasi-static mechanical analysis can be written as follows:

$$\nabla \cdot \boldsymbol{\sigma} + \boldsymbol{b} = \mathbf{0}, \boldsymbol{r} \in \Omega \tag{2.7}$$

where $\boldsymbol{\sigma}$ denotes the stress tensor and $\boldsymbol{b}$ represents the body force vector of the model. As for the boundary conditions, the Dirichlet and Neumann boundary conditions will be considered, as formulated in Eqs. (2.8) and (2.9) in the following:

$$\boldsymbol{u} = \bar{\boldsymbol{u}}, \boldsymbol{r} \in \Gamma_D^M \tag{2.8}$$

$$\boldsymbol{\sigma} \cdot \boldsymbol{n} = \bar{\boldsymbol{t}}, \boldsymbol{r} \in \Gamma_N^M \tag{2.9}$$

where $\boldsymbol{u}$ denotes the displacement vector and is prescribed $\bar{\boldsymbol{u}}$ on the mechanical boundary Γ_D^M. In Eq. (2.9), dot product of the stress tensor $\boldsymbol{\sigma}$ and normal vector $\boldsymbol{n}$ is the surface traction vector, which is prescribed $\bar{\boldsymbol{t}}$ on the mechanical boundary Γ_N^M.

In this dissertation, the temperature dependent elastic-plastic material model is utilized in order to be better consistent with practical mechanical behavior of metal materials in the AM process. The constitutive equation of the material model can be written as follows:

$$\sigma_{ij} = C_{ijkl}(E_{kl} - E_{kl}^p - E_{kl}^{th}) \tag{2.10}$$

where C_{ijkl} denotes the fourth-order tensor of elasticity; E_{kl}, E_{kl}^p, and E_{kl}^{th} represent the total, plastic and thermal strain, respectively. The associate J_2 plasticity model with temperature-dependent mechanical properties is used in the analysis. The details of the process model can be found in Ref. [55].

2.1.3 Element Activation Method

In an AM process, materials are deposited in a layer-by-layer manner. The elements in each of the deposited layers do not have any contribution to the FEA until the heat source arrives. As the heat source moves sufficiently close, the elements surrounding the laser spot will be deposited. When the deposition ends, all the elements involved in the deposition are activated and contribute to the thermal and mechanical analysis. For this purpose, the birth and death element activation method [35, 55, 57] is utilized in this dissertation. Advantages of the birth and death element technique include the following two aspects. On the one hand, no ill-conditioning problem will be introduced to the matrix of structural global stiffness and mass. On the other hand, only the degrees of freedom of active elements are involved, which contributes to a relatively small algebraic system to solve.

Nevertheless, the element birth and death technique has the following disadvantages. First, it is not easy to implement the method into the commercial FEA software through user-defined subroutines. Second, renumbering of the equations and re-initialization of the solver are performed every time new elements are activated, which will negate savings of the computational cost.

In addition, an element activation criterion is required to determine whether an element needs to be activated in the simulation. A feasible activation criterion combined with the double ellipsoid heat source model is employed in this dissertation. The inactive elements are activated where the heat power is higher than 5% of the maximum value at the ellipsoid center [55].

2.1.4 Experimental Setup for Validation of Process Modeling

The LENS 450 metal AM system (Optomec, Albuquerque, NM) used to perform the experiment is shown in Figure 2.1, and the material being printed is a titanium alloy called Ti-6Al-4V (Ti64).

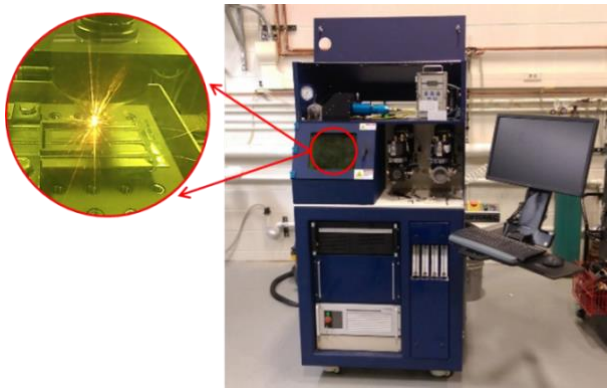

Figure 2.1 The Optomec LENS 450 Metal Printer

A fixture that mounts onto the build platform is designed to hold a small substrate for deposition, which acts as a cantilever that allows residual deformation to be measured (see Figure 2.2(a)). The LENS system allows the input of the exact build path and process parameters such as the laser power, scanning velocity, and powder feed rate. After printing is completed, 3D laser scanning device shown in Figure 2.2(b) is utilized to measure the residual distortion of the part in the vertical direction. Before measuring the residual distortion, a calibration test against the laser scanning device should be performed first. Difference between two scanned configurations of an identical part is taken as the system error of the measurement. It suggests that the measurement error of the 3D laser scanning device is ±0.075 mm.

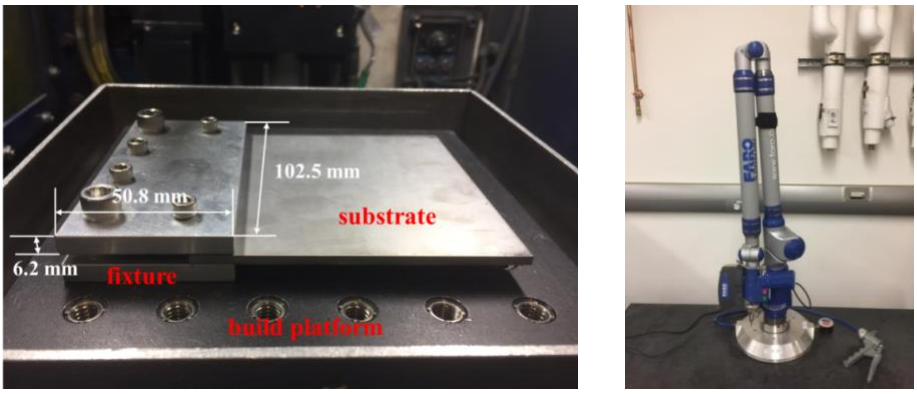

(a) (b)

Figure 2.2 Experimental Setup: (a) the Fixture and Substrate (b) the 3D Laser Scanning Device

Before the fixture and substrate are mounted onto the build platform in the chamber of the LENS machine, the bottom surface of the undeformed substrate is scanned as a reference. After a metal part has been deposited onto the substrate, bottom surface of the deformed substrate is scanned for a second time to compare with the reference. Accuracy of the detailed LENS process model of Ti64 has been validated [55], in which specific material parameters, heat source, and boundary conditions can be found. Hence only a few details about the detailed process model are provided below, and interested reader is referred to Ref. [55] for further details.

2.2 Inherent Strain Theory

2.2.1 Original Theory

The original theory of inherent strain is briefly reviewed here based on literature on welding mechanics [39, 58]. In the micro-welding process, the material along the weld path will

first be heated, melted, and then solidified in a short time span, which would result in large temperature gradient and complex deformation path. As a result, thermal strain, mechanical strain (both elastic and plastic), and strain due to phase change will be generated and re-equilibrated throughout the welded part. Since the strain caused by phase change is relatively small compared with the other two kinds of strains, it is usually ignored when computing the inherent strain [35, 36]. (However, if necessary, the inherent strain formulation involving phase change can be accessed as well [49, 54].) After welding is completed, the welded part cools to the ambient temperature.

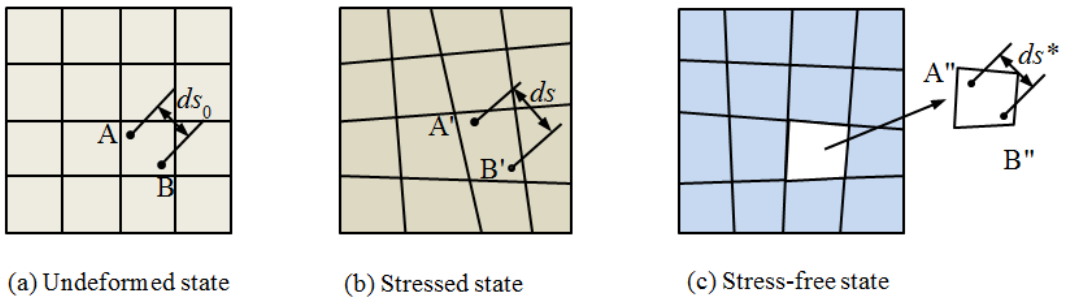

Figure 2.3 Original Definition of Inherent Strain for Welding Mechanics

Now consider two material points A and B in close proximity with each other within a micro- solid as shown in Figure 2.3. The distance between the two points is assumed to be ds_0 and ds at the standard and stressed state before and after the welding process, respectively. Then after the residual stress is relieved via relaxation by removing the infinitesimal element containing the two points (see Figure 2.3(c)), the distance between the two points becomes ds^*. By definition, the inherent strain in the element is defined as the residual strain in the stress-relieved state with reference to the undeformed state in Figure 2.3(a) before the welding process takes place:

$$\varepsilon^* = (ds^* - ds_0)/ds_0 \tag{2.11}$$

After the welding process, the metal part is cooled down to the ambient temperature and thermal strain in the part vanishes. Since the reference temperature employed here is always the ambient temperature of the entire system, thermal strain is not concerned and only mechanical strain is involved. Equation (2.1) can be rearranged as follows:

$$\varepsilon^* = (ds - ds_0)/ds_0 - (ds - ds^*)/ds_0 \tag{2.12}$$

Given that ds approximates ds_0 under assumption of infinitesimal deformation, Eq. (2.12) can be further written as:

$$\varepsilon^* = \underbrace{(ds - ds_0)/ds_0}_{\varepsilon} - \underbrace{(ds - ds^*)/ds}_{\varepsilon_e} \tag{2.13}$$

where the first term on the right-hand side is the total mechanical strain ε after the welding is finished, while the second term is the mechanical elastic strain ε_e, which is directly proportional to the stress released.

Practical application of the original inherent strain theory to welding problems makes a key assumption that the elastic strain is insignificant compared to the plastic strain. Hence it follows from Eq. (2.13) that all the elastic strains vanish and the inherent strain ε^* becomes equal to the plastic strain ε_p generated from the welding process [39-41]:

$$\varepsilon^* = \varepsilon_p \tag{2.14}$$

From this assumption, components of the inherent strain caused by welding can be determined relatively easily through a relatively small-scale welding process simulation of a straight line via FEA, or measured directly from welding experiment. This conventional method applies the inherent strains as the initial strains in the weld regions (i.e., heat affected zone (HAZ) along the welding path [40, 44]) of an elastic finite element model, in order to compute its

distortion through a single static analysis. This approach has been shown to be accurate for solving simple welding problems consisted of isolated weld lines [39-41].

For AM problems, the assumption that the elastic inherent strain is insignificant is somewhat invalid and inaccurate for modeling residual stress and distortion in AM parts, because the physical process of AM is quite different from simple metal welding. On the theoretical side, the key assumption that the elastic strain generated by the welding process vanishes is generally not valid for AM parts. During the AM process, new depositions will become mechanically constrained, since new mechanical boundaries continue to emerge with deposition of new tracks and layers. After multiple layers of materials are printed, the mechanical constraints for the previously deposited layers reach a steady state. The elastic strain in the AM process will go into distortion of the remaining AM build. Thus, the inherent strain must contain terms related to elastic strains, in addition to the plastic strain given in Eq. (2.14) in the original theory.

2.2.2 Modified Theory for AM

In order to overcome these issues, a modified inherent strain theory [59] is proposed to estimate the inherent strains from detailed process simulation of an AM part. The physical basis of the proposed modified inherent strain theory is discussed here. Figure 2.4 schematically illustrates the stress-strain history induced at a material point (black dot), where the heat source passes through and creates a HAZ during an AM process. The starting point of the illustration is when the material point of interest is experiencing the highest temperature due to the heating. For convenience of discussion, assume the material point is both stress free and strain free (Figure 2.4A). A large temperature gradient will appear in front of the heat source center [24-26]. As the heat source moves away to the left (Figure 2.4B), the material point of interest cools down and

solidifies rapidly and experiences a significant amount of shrinkage (compressive strain) but very small compressive stress. The reason is because the yield stress at elevated temperature is very small, and thus the material point of interest yields easily and rapidly, resulting in a large compressive plastic strain. As the heat source moves further away, cooling at the point of interest slows down while the material ahead has just solidified and is undergoing large shrinkage, which induces non-linear tensile stress and strain onto the material point of interest. The tensile stress would reach a maximum point (Figure 2.4C). If this were a simple welding problem, the inherent strain can be obtained by relaxing the solid to a stress-free state, and then use the resulting compressive strain as the inherent strain [37, 39]. Different from the simple welding problem, the elastic strain in each deposited layer in an AM process is significantly affected by the evolving mechanical boundaries as additional materials are being deposited. The effect due to the evolving mechanical boundaries on the elastic inherent strain must be accounted for.

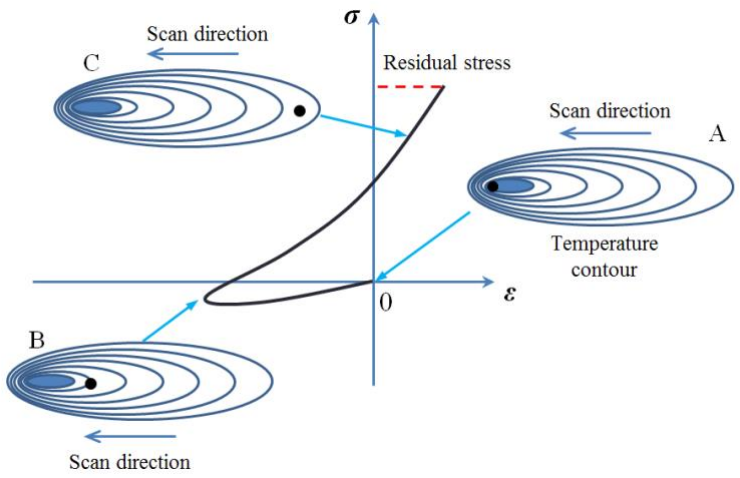

Figure 2.4 Schematic Illustration of Mechanical Strain Induced at a Material Point during a Simple Welding Process

To simplify the formulation of the modified inherent strain model, consider a simple two-line-layer deposition case in Figure 2.5, where one line is deposited on top of a cantilever beam, followed by deposition of another line on top of the first line. For the purpose of computing the inherent strain induced at a material point in the bottom layer, two distinct mechanical states, an intermediate state and a steady state, are defined as follows. The intermediate state is defined as the state when the heat source just passes by and the local (compressive) mechanical strain reaches the largest amplitude (cf. Figure 2.5(b)), whereas the steady state is when the temperature of the whole system cools to the ambient temperature (see Figure 2.5(c)). The modified inherent strain is defined as the difference between the total mechanical strain at the intermediate state and the elastic strain at steady state.

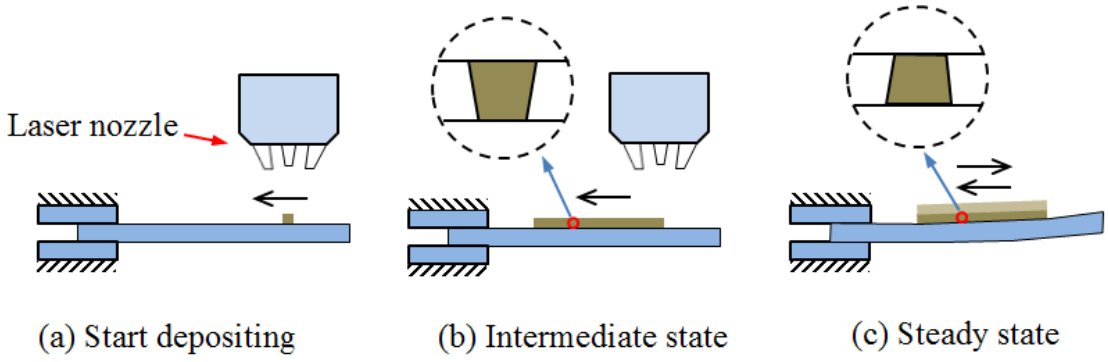

Figure 2.5 Two States for the First Layer of a 2-Layer Deposition: (a) Depositing Starts from Right Side; (b) Mechanical Boundary for the Concerned Material Points (Red Circle) Is Considered as Stable after the First Layer Is Deposited; (c) The Entire Part Reaches the Final Steady State

The inherent strain can be expressed mathematically as:

$$\varepsilon^{In} = \varepsilon_{t_1}^{Plastic} + \varepsilon_{t_1}^{Elastic} - \varepsilon_{t_2}^{Elastic} \tag{2.15}$$

which can also be rearranged as:

$$\varepsilon^{In} = \varepsilon_{t_1}^{Total} - \varepsilon_{t_2}^{Elastic} \tag{2.16}$$

where t_1 and t_2 denote the time corresponding to the intermediate and steady state for the point of interest, respectively. $\varepsilon_{t_1}^{Plastic}$, $\varepsilon_{t_1}^{Elastic}$ and $\varepsilon_{t_1}^{Total}$ represent the plastic, elastic, and total mechanical strain at the intermediate state, respectively, while $\varepsilon_{t_2}^{Elastic}$ represents the elastic strain at the steady state.

Why are these two specific mechanical states chosen? The compressive mechanical strain of a material point at the intermediate state is the direct result of rapid solidification of the melt pool and thus contributes significantly to the inherent strain. The mechanical strain generated up to that state is highly localized and has not spread to its neighboring material yet. What follows is that the material point of interest continues to cool at a much slower rate, and the negative change in thermal strain gradually converts into positive change in elastic strain (i.e. tensile strain), which represents another key contribution to the inherent strain. Note that this change is non-isotropic since it depends on the mechanical boundaries surrounding the point of interest. This is the reason why the elastic strain at steady state is selected for computing the inherent strain.

In the proposed model, only the normal strains are extracted. Indeed, shearing deformation also has some influence on the final residual distortions. However, since the layer thickness is usually much smaller compared with the other two dimensions, the shear stress to the previously deposited lower layers induced by a newly generated upper layer is very limited. As a result, the shearing deformations caused by the thermal shrinkage of the upper layers are neglected in this dissertation. The results in this dissertation demonstrate that it is acceptable to ignore the shear strains. It will be demonstrated that the model presented above is valid not only for two-line deposition, but for multiple-line deposition on top of each other in the LENS process. Validation

of the model will be achieved by comparing with results obtained from detailed process simulation and deformation experiment.

2.2.3 Assignment of the Modified Inherent Strain

After the modified inherent strains of the elements involved have been obtained through Eq. (2.16), it is necessary to propose a way to load the strains into the static equilibrium model. In the original ISM, residual deformation of the welded components was estimated by a linear elastic model using the inherent strains as the initial strains. However, it has been demonstrated that the original method of applying inherent strains in a pure elastic analysis cannot obtain a good accuracy when directly applied to the additive manufacturing process. In this dissertation, the modified inherent strains will be employed in a nonlinear elastic-plastic model in the fast method. Since the inherent strains cannot be applied directly as an external load to a finite element model in commercial FEA codes, one feasible way is to apply the inherent strains ε^{In} as thermal strains ε^{Th} through the following equations [44]:

$$\varepsilon_i^{Th} = \varepsilon_i^{In},\ i = x, y, z \tag{2.17}$$

$$\varepsilon_j^{Th} = \alpha_j \Delta T, j = x, y, z \tag{2.18}$$

where α_j denotes the equivalent coefficient of thermal expansion (CTE) and ε_i^{Th} represents the equivalent thermal strain in the *j*th direction in the Cartesian coordinate system. ΔT is the temperature change and is taken as unity in this dissertation.

As the modified inherent strains of some elements are compressive and negative, the values assigned for the corresponding CTEs are also negative. Although this may seem unphysical, the resulting deformation obtained from this method is valid. After the CTEs of all the elements in

the HAZ are assigned, a unit temperature change is applied to the HAZ as an external load. This is followed by performing a static equilibrium analysis to compute the residual distortion. Since the numerical static analysis is performed just once, the proposed method can save most of the computational time compared with the detailed process simulation.

2.3 Validation of the MISM

In this section, two examples will be employed to validate the MISM proposed based on Eq. (2.16). All the process modeling, computational, and post-processing tasks were coded using the APDL environment in the commercial ANSYS simulation software. The classical mechanical package in ANSYS r17.2 was called to read the input files and conduct the thermal and mechanical analysis. The element type used was the solid brick element containing 8 nodes named solid185. Each node has three degrees of freedom corresponding to the displacements (UX, UY, UZ). This element type has good bending behavior even when the mesh is coarse and is one of the most commonly used element types. Results with excellent accuracy can typically be obtained using this element type.

In the following two examples, there is one element in the thickness dimension of a single layer, and the thickness of the element is close to the laser penetration depth. The number of elements in the entire deposition thickness equals the number of physical layers. This element size in the thermomechanical simulation was shown to have good accuracy compared to the experiments where the thermal history and residual deformation were measured. Based on past literature and the own experience, it is a common practice to employ only one element in the layer thickness in many references [27, 28, 35, 36, 55]. It is clear that finer mesh with two or more

elements in the thickness can also be used for the simplified detailed process model. However, it will be very expensive to implement the simulation.

2.3.1 Single Wall Deposition Model

The first example employed to validate the MISM proposed is a single wall produced by depositing multiple single tracks on top of each other on a substrate. The model and a back-and-forth laser scanning path are shown in Figure 2.6. The left end of the substrate consists of two fixtures connected to the platform in the chamber of the LENS machine.

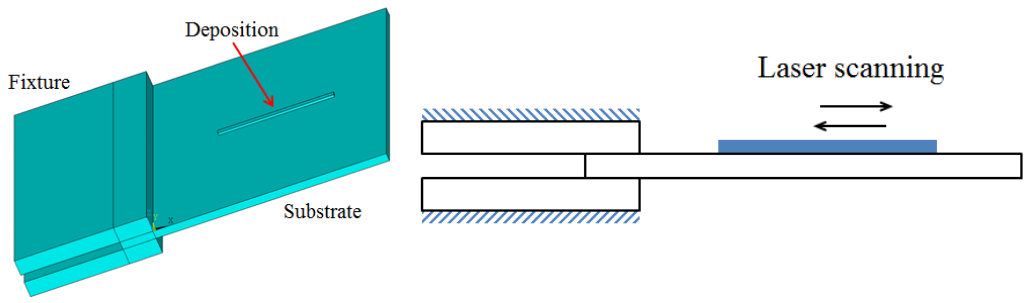

Figure 2.6 A Line Deposition and the Laser Scanning Path

Table 2.1 Geometrical Parameters of the LENS Depositions

Number of layers	Length /mm	Width /mm	Height /mm
1	44.57	2.0	0.99
2	44.57	2.0	1.80
3	44.57	2.0	2.70
5	44.57	2.7	4.75
10	36.00	3.0	9.00

Geometrical parameters including the length, width and height of the line depositions are shown in Table 2.1. The size of the substrate is 102×102×3.22 mm^3. Both the deposition and substrate are made of Ti64. For the deposition, the process parameters employed are as follows: Laser power of 300W, scan velocity of 2.0 mm/s, and powder feed rate of 8 rotations per minute (RPM). The input heat source model employs the double ellipsoid model in which the absorption efficiency is taken to be 45% [35, 55]. The laser scanning starts from a designate point close to the free end of the substrate and moves toward the clamped end. When printing the next layer, the laser beam scans in the opposite direction, i.e., from the clamped side to the free end. The laser scanning strategy repeats itself every two layers. Material property of Ti64 is temperature dependent and detailed information can be found in Refs. [30, 55]. The total processing time is 1,600 seconds with the entire heating and cooling process included. Without specific instructions, residual distortion in all the figures is in unit of meter.

It could take a few hours to finish running the detailed process simulation. Usually the maximum residual distortion and stress are of the most concern. As shown in Figure 2.7, the displacement profile of the one-layer line deposition in the vertical direction is obtained by the detailed process simulation. The maximum distortion occurs at the free end of the substrate and the value is 0.326 mm. In addition, many elements in the deposition are at yield state and their von Mises stress is ~765 MPa, which agrees with the yield criterion with respect to the mechanical plastic property of Ti64 at room temperature.

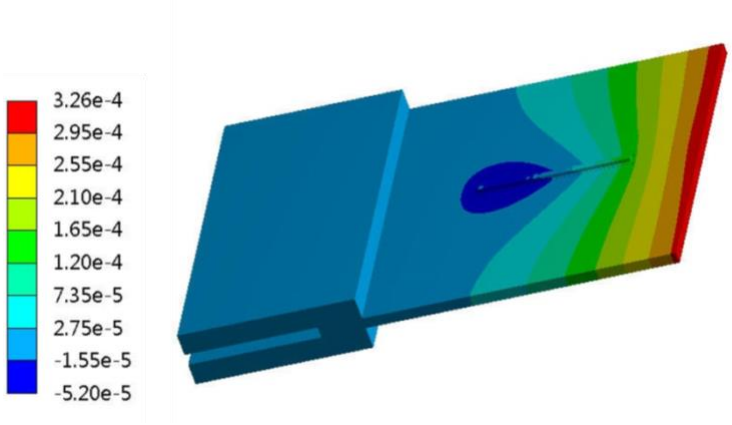

Figure 2.7 Vertical Residual Distortion (Unit: m) of a 1-Layer Line Deposition by Detailed Process Simulation

Before extracting the inherent strains, it is necessary to show how the HAZ should be estimated from the detailed process simulation. The plastically deformed areas indicate the existence of the inherent strains. Besides the metal depositions, an extension has to be considered since the plastic deformations are also found in the local areas of the substrate. A thin layer beneath the metal deposition is deformed due to the high temperature caused by the intensive heat input when the first layer of the metal part is built. To determine the reasonable HAZ, the simplest way is to investigate the distribution of the residual plastic deformations after the entire deposition is finished in the detailed simulation. All the plastic deformed elements are selected according to the range of their coordinates. Then the inherent strains of those selected elements are calculated based on the simulation results.

In order to illustrate that the conventional theory of inherent strain is not valid for AM, the inherent strain is computed based on Eq. (2.14) and then is utilized to compute residual distortion. Only the final state at room temperature is concerned according to the definition of conventional inherent strain model. Both single-layer and multi-layer depositions were investigated. Computed results of the vertical residual distortion are listed in Table 2.2 and compared with those obtained

by detailed process simulation. The computational times of the two different methods are also shown to demonstrate the advantage of the ISM as a fast prediction tool. The large errors shown in the table suggest that the conventional inherent strain theory is not accurate for estimating the residual distortion of an AM process. Therefore, the modified theory is proposed in this dissertation.

Table 2.2 Maximum Vertical Residual Distortion of the Part after LENS Deposition of a Straight Line and Computational Times by Detailed Process Simulation and Conventional ISM

Number of layers	Detailed process simulation		Conventional ISM		Distortion error (%)
	Distortion (mm)	Computational time (min)	Distortion (mm)	Computational time (min)	
1	**0.326**	21.6	**0.170**	1.2	**47.9**
2	**0.502**	33.0	**0.299**	1.8	**40.4**
3	**0.584**	43.7	**0.412**	2.2	**29.8**
5	**0.937**	57.6	**0.672**	3.2	**28.3**
10	**0.663**	114.4	**0.478**	4.2	**27.9**

In order to illustrate how to evaluate the inherent strains using the modified theory based on the detailed process simulation, the two-layer line deposition case is taken as an example, and the inherent strains of the elements in the lower layer are concerned. The critical step here is to determine the reasonable time steps corresponding to the intermediate and steady states. Since the length of the line deposition is relatively small, an easy way to determine the intermediate state (when the compressive plastic strain reaches the maximum) to be the time step for the concerned layer when the deposition of the next upper layer is just completed. This time step is thus employed

as the intermediate state for the elements in the concerned layer to extract the total mechanical strains. After the entire printing process is complete, the deposition reaches the steady state and then the elastic strains of the elements in the lower layer are extracted. Using Eq. (2.16), the modified inherent strains in three dimensions can be calculated. The averaged inherent strain values against the normalized deposition length are plotted in Figure 2.8. The longitudinal direction represents the major laser scanning path, while the transverse direction is perpendicular to the in-plane scanning direction. The vertical direction indicates the build direction. Using the same method, the inherent strains of the elements in all the deposition layers can be obtained from post-processing of the detailed process simulation results. Figure 2.8 shows a general distribution pattern of the inherent strains in the AM metal parts, but the magnitudes of the inherent strains in different layers may be a little different due to the variation of the laser scanning paths.

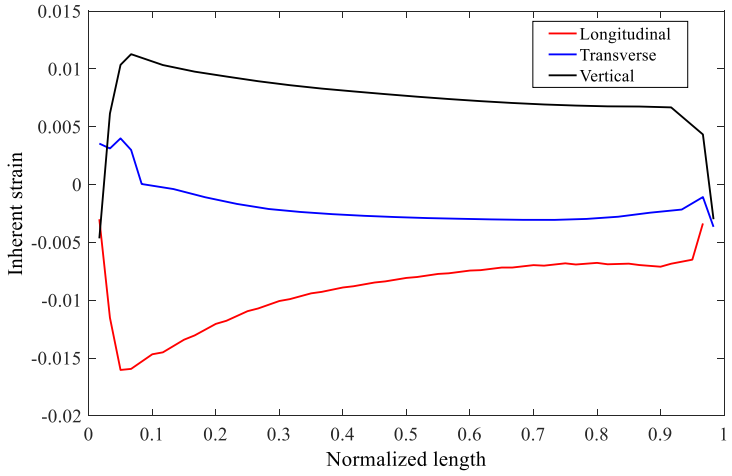

Figure 2.8 The Extracted Elemental Inherent Strains of the Lower Layer in a 2-Layer Line Deposition

After the inherent strains are obtained using the modified theory, residual distortion can be computed through a single static equilibrium analysis within a few minutes on a desktop computer. Note the conceptual formulation of the MISM is illustrated using the two-pass deposition (see

Figure 2.5) because it is more straightforward to explain the intermediate state for a typical material point in the metal depositions. However, it does not mean the proposed method is not applicable to the single-track experiment. The same concept of finding the rapid solidification state still needs to be applied to the one-layer case to extract the inherent strains. For the one-layer line deposition, the distribution pattern of the vertical residual distortion of the part, as shown in Figure 2.9, is almost identical to that shown in Figure 2.7, and the maximum vertical distortion is 0.348mm. Excellent agreement can be observed between the results computed by the detailed process simulation and the MISM.

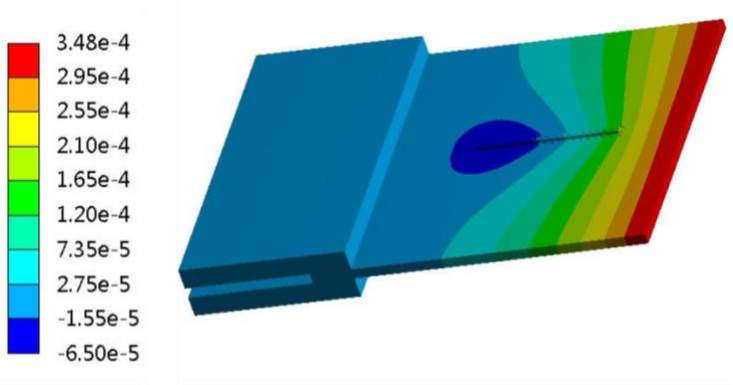

Figure 2.9 Vertical Residual Distortion (Unit: m) of the 1-Layer Line Deposition by the MISM

Moreover, vertical residual distortions resulting from line depositions for different layers obtained by detailed process simulation and the MISM are compared in Table 2.3. Note that the errors in the vertical displacement computed by the modified theory are 5~15 times smaller than the corresponding ones obtained by the original theory when compared to the detailed process simulation results. Since there is no obvious trend in the errors for different number of layers (Table 2.3), the assumption that the mechanical boundary condition reaches steady state after one layer has been deposited seems to be valid. This makes extracting the inherent strains from detailed

process simulation much more straightforward. Whereas, Table 2.3 contains result for the two-layer line deposition, and the prediction error of 10.9% is the largest among all the different cases. Although the conceptual formulation of the modified inherent strain theory is illustrated using a two-layer deposition, it is not expected to represent the best result for the two-layer case. Since even the largest percentage error is of the same magnitude to the ten-layer case (8.4%) in Table 2.3, this discrepancy is insignificant. Thus, the relatively large error in the case of the 2-layer model is believed to be a random occurrence.

Table 2.3 Maximum Vertical Residual Distortion of the Part with Line Depositions and Computational Times by Detailed Process Simulation and MISM

Number of layers	Detailed process simulation		MISM		Distortion Error (%)
	Distortion (mm)	Computational time (min)	Distortion (mm)	Computational time (min)	
1	**0.326**	21.6	**0.348**	1.5	**6.7**
2	**0.502**	33.0	**0.557**	2.1	**10.9**
3	**0.584**	43.7	**0.606**	2.6	**3.8**
5	**0.937**	57.6	**0.956**	3.5	**2.0**
10	**0.663**	114.4	**0.607**	4.4	**8.4**

Next, the vertical residual distortion profiles of a five-layer line deposition obtained by detailed process simulation and MISM are shown in Figure 2.10(a) and 2.10(b), respectively. The distribution of the vertical distortion is symmetric in the plane since the laser scanning path and the mechanical boundary conditions are both symmetric in this problem. Very good agreement is

observed by comparing the two figures. Both the accuracy and efficiency of the proposed method are further validated.

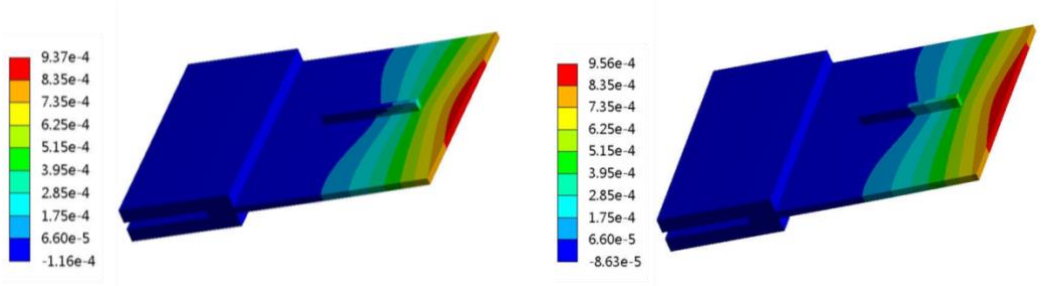

(a) (b)

Figure 2.10 Vertical Residual Distortion (Unit: m) of the 5-Layer Line Deposition by (a) the Detailed Process Simulation and (b) the MISM

In terms of computational efficiency, the computational times of the detailed process simulation and the MISM are also shown in Table 2.3. Generally, a ~20x speedup can be achieved using the MISM as compared with detailed process simulation. Especially for the depositions containing more layers, the computational efficiency becomes higher (see 10-layer case in Table 2.3). Clearly, with more development, the proposed method has great potential in fast prediction of residual deformation in an AM part.

2.3.2 Rectangular Contour Wall Deposition Model

In order to further demonstrate accuracy of the proposed method, the rectangular contour wall deposition shown in Figure 2.11 is investigated here. In the printing process, the laser scanning path is counterclockwise as illustrated by arrows in the figure. Each side of the model can be considered as an independent single-walled deposition, since the intersection of any two

neighboring sides is relatively small. Since an intermediate state containing a stable mechanical boundary is critical in the proposed theory, the intermediate state of the elements in the layer of interest is defined as the moment when the overlaid layer on the same side has just been deposited.

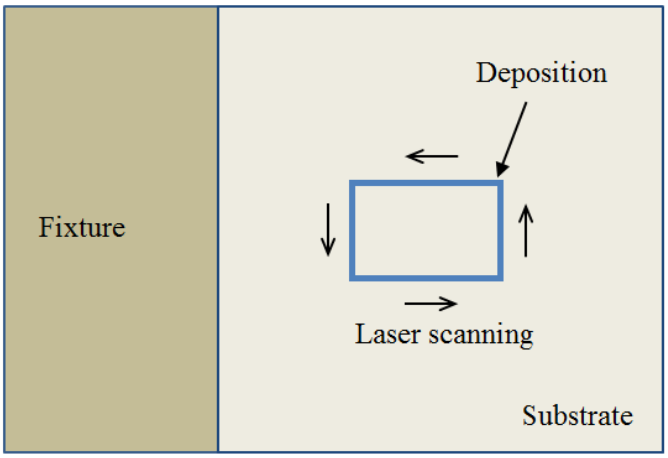

Figure 2.11 Laser Scanning Path of the Rectangular Contour Deposition

First, detailed process simulation is conducted for the rectangular contour wall with different number of layers. In particular, for the five-layer rectangular contour wall, dimension of the substrate is set to 101.6×101.6×3.18 mm^3 in order to be consistent with the experimental setup. For other cases, the size of the substrate is the same as in the first example. Geometrical parameters such as the length (L), width (W), thickness (T) and height (H) of the rectangular contour depositions are shown in Figure 2.12 and also listed in Table 2.4 below. The process parameters employed are as follows: Laser power 300W, scan velocity 2.0 mm/s, and powder feed rate of 6 RPM. In addition, to ensure numerical convergence of the detailed process simulation for the five-layer contour, the substrate is meshed using two layers of elements in the thickness direction, while three layers of elements are employed for the other cases. To ensure the choice does not create an unfair comparison, the influence of the element mesh to the numerical simulations has been

investigated through a series of process simulations. For the five-layer contour deposition case, two cases were investigated where the substrate was meshed into one and two elements in the dimension of thickness, respectively. It is found that the influence by the element mesh of the substrate to the entire residual distortions is negligible, which indicates that the substrate mesh is not a concern to the validation of the proposed method.

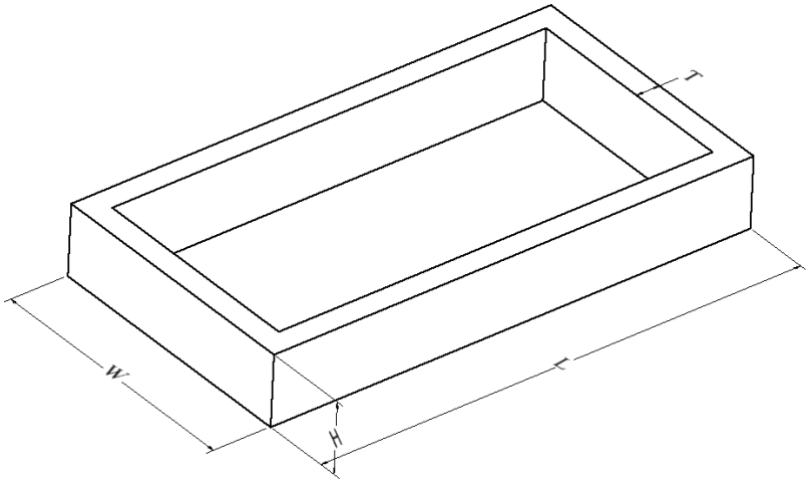

Figure 2.12 Illustration of the Geometry of the Rectangular Contour Deposition

Table 2.4 Geometrical Parameters of the LENS Rectangular Contour Depositions

Number of layers	Length /mm	Width /mm	Thickness /mm	Height /mm
1	41.86	22.37	2.52	0.90
2	41.86	22.37	2.20	1.90
4	31.80	19.80	2.10	4.10
5	41.86	22.37	2.72	4.43

Through detailed process simulation and MISM, the maximum residual distortion in the vertical direction for the rectangular contours with different number of layers is listed in Table 2.5.

The difference between the results obtained by the two different methods is very small, which indicates good accuracy for the proposed method. Although the substrate deformation results are much more consistent for layers 2 through 5 cases, no obvious trend is found in the substrate deformation results for the different number of deposition layers. Regarding a larger error in the one-layer case, a reasonable explanation is that it may not be so robust to identify the intermediate state of a long single layer deposition using exactly the same way established based on the multi-layer LENS process. Since the difference was acceptable when the same way of identifying the intermediate state was applied in all the cases, the one-layer contour case was still included to demonstrate the efficiency of the proposed method. In addition, the computational times of the detailed process simulation and the MISM are shown in Table 2.5. The computational efficiency has a significant improvement (e.g. nearly 80x speedup for the 5-layer case) due to benefit of the proposed method.

Table 2.5 Maximum Vertical Residual Distortion of the Part with Rectangular Contour Deposition and Computational Times by the Detailed Process Simulation and the MISM

Number of layers	Detailed process simulation		MISM		Distortion Error (%)
	Distortion (mm)	Computational time (min)	Distortion (mm)	Computational time (min)	
1	**0.499**	134.0	**0.432**	2.4	**13.4**
2	**0.776**	153.6	**0.798**	3.2	**2.8**
4	**0.950**	398.1	**0.973**	4.2	**2.4**
5	**1.157**	439.2	**1.131**	4.8	**2.2**

Meanwhile, the respective vertical displacement profiles of the rectangular contour wall with two layers and five layers obtained from the two different methods are shown in Figures. 2.13 and 2.14.

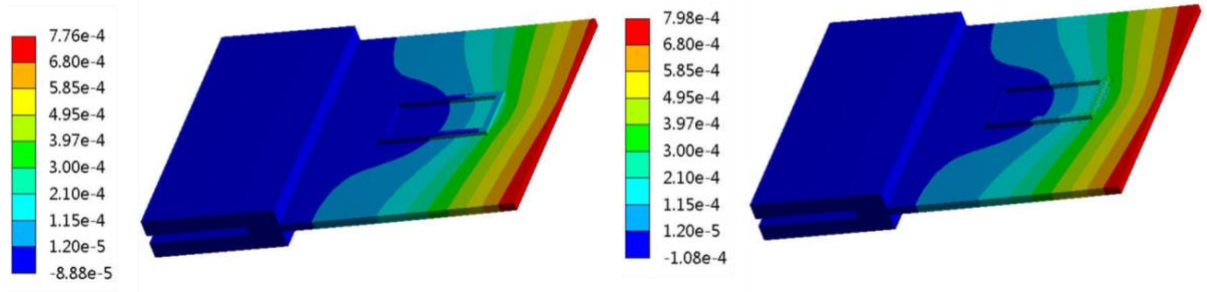

(a) (b)

Figure 2.13 Vertical Residual Distortion (Unit: m) of the Part with the 2-Layer Contour Deposition (a) by the Detail Process Simulation and (b) by the MISM

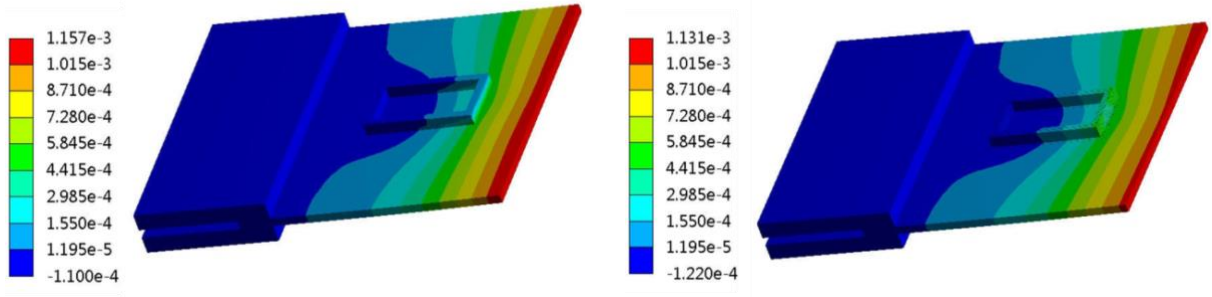

(a) (b)

Figure 2.14 Vertical Residual Distortion (Unit: m) of the Part with the 5-Layer Contour Deposition (a) by Detailed Process Simulation and (b) by the MISM

As can be seen, the maximum residual distortion occurs at the free end of the substrate in the vertical direction. Clearly, the distribution of the vertical displacement field obtained in two

ways is the same: A local region with negative vertical displacement exists close to the clamped end of the substrate, and positive deflections always occur along the free end. By comparison, very good agreement between the vertical displacement profiles can be clearly seen, which strongly verifies accuracy of the proposed MISM for predicting residual distortion of the LENS process.

Finally, to further validate the modified inherent strain theory, an experiment was conducted to measure residual distortion resulting from the LENS process. A five-layer rectangular contour shown in Figure 2.15 was manufactured using the LENS system. Residual distortion in the vertical direction is measured using a 3D laser scanning device.

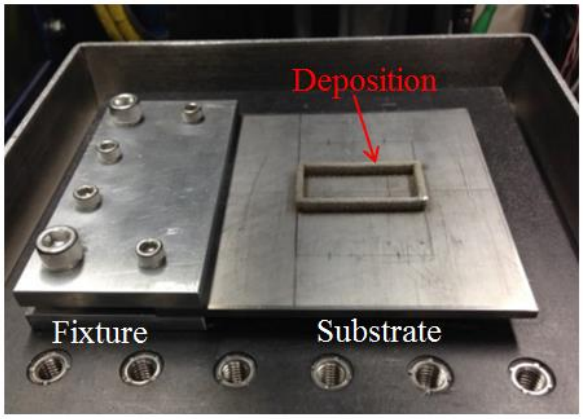

Figure 2.15 The Experimental Setup and the 5-Layer Contour Deposition by LENS

Surface profiles of the residual vertical distortion of the substrate obtained by three different methods, namely the MISM, detailed process simulation, and the experimental measurement, are shown in Figure 2.16. Clearly the distributions of the distortion field are very similar to each other. Note for the experimental result shown in Figure 2.16(c), the flexural behavior is slightly stronger compared to the results obtained by the detailed process simulations and the MISM. The possible reason is that there exists a little residual stress in the substrates since

some machining treatment was done in the manufacturing process. The LENS process may contribute to releasing the residual stress in the substrate, generate some bending and affect the distribution of the distortions. This explanation is acceptable since similar observations had been obtained in other experiments using the same substrates.

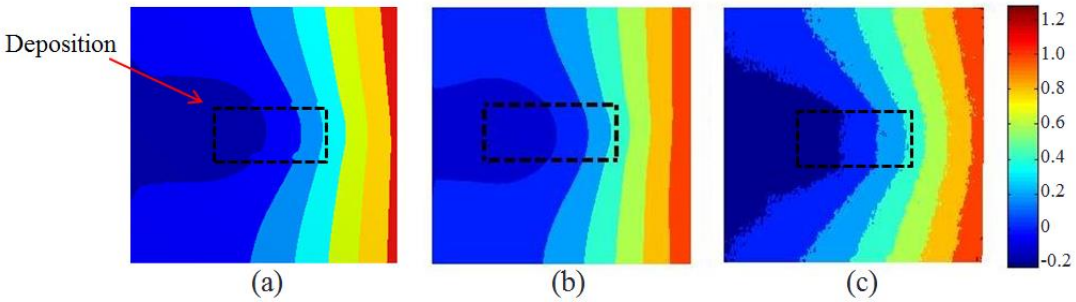

Figure 2.16 Vertical Residual Distortion (Unit: mm) of the Substrate with LENS Deposition of 5-Layer Rectangular Contour by (a) MISM (b) Detailed Process Simulation (c) Experimental Measurement

In addition, both the minimum and maximum vertical residual distortions of the substrate are listed in Table 2.6. A concern is that the minimum distortion magnitudes are roughly 50 percent different from the experiment and two possible reasons are provided. First, the resolution of the laser scanning device is ±0.075mm, which may induce some error to the deformation measurement. As seen in the table, the magnitudes of the minimum distortion obtained by the detailed process simulation and the MISM are very small and close to the measurement precision. The experimental measurement of the residual distortion may have some uncertainty caused by system errors, leading to slightly larger magnitudes (see Table 2.6). Second, the large error also has to do with the inaccurate boundary condition of the clamp since the minimum distortion location is close to the clamp. In the experiment, the fixtures were clamped by only several bolts as seen in Figure 2.15. However, all the nodes of the fixtures were fixed strictly as the mechanical

boundary conditions in the simulations. As a result, a relatively smaller distortion is seen in the simulation results, but generally, the maximum residual distortions are in excellent agreement with each other. From these results, the effectiveness and accuracy of the MISM are both proved.

Table 2.6 Vertical Residual Distortion (Unit: mm) of the Substrate with a LENS Deposited 5-Layer Rectangular Contour in Three Different Ways

	Minimum	Maximum	Relative error of the maximum distortion (%)
MISM	-0.121	1.131	11.7
Detailed process simulation	-0.107	1.157	9.7
Experimental measurement	-0.217	1.281	---

In this section, all the deposition lines were simulated and the inherent strains for the entire part were extracted and applied back to the LENS build. Compared to the thermomechanical simulation results, many features of the residual deformation can still be seen when this full-scale inherent strain approach is employed. This full-scale inherent strain approach is simply used to verify the accuracy of the modified model proposed in Eq. (2.16).

2.4 Mean Inherent Strain Vector Approach

For single-walled structures containing many layers, in order to achieve satisfactory results, typical inherent strains extracted from two successive line deposition layers can ensure prediction accuracy. It is unreasonable to only simulate a one-layer line deposition model for extracting typical inherent strains because the re-melting process is not considered in this one-layer process

model. On the other hand, in the LENS processing of the single-walled model, the deposited materials have enough time to cool down since the laser scanning speed is low (2 mm/s) and the length of the deposition line is large. Moreover, the large substrate is also made of the same Ti64 material with the deposition. Thus, it is not necessary to simulate more than two deposition lines to extract the inherent strains, since it can be assumed that most of the deposition lines experience the same melting and re-melting process.

To verify the above statement is correct, a representative volume of the full-scale two-layer and three-layer line deposition model is employed in the detailed process simulation to extract the inherent strains, respectively. As depicted in Figure 2.8, the inherent strains are averaged over entire length of the deposition line. Hence a mean strain vector of (-0.0070, -0.002, 0.008) is obtained for the two-layer model, while (-0.0073, -0.003, 0.007) is obtained for the three-layer case. The inherent strain vector is converted to orthogonal CTEs and uniformly assigned to the multi-layer models as thermal material properties. In the solution, the elements of the multi-layer models are activated layer-by-layer and unit temperature is applied as the external load. The results for the three-layer and five-layer wall structures obtained by the layered ISM and detailed process simulation are shown in Table 2.7. The errors are a little larger than the results obtained from full-scale detailed simulation of the entire build shown in Table 2.3. A possible reason is that the mean inherent strains, which are accurate only in the middle region of a large part, are applied uniformly to all the elements including those close to the surface. Despite the difference, very good agreement is shown between the results obtained from the two different methods. the results demonstrate that only two deposition layers are needed in the representative volume model to ensure accuracy. However, if still higher accuracy is desired, three or more deposition layers may be employed to extract the inherent strains.

Table 2.7 Maximum Vertical Residual Distortion of the Substrate with LENS Deposited 3- and 5-Layer Straight Wall Structure and Computational Times by Detailed Process Simulation and Layered ISM

Number of layers	Detailed process simulation		Simulation based on mean inherent strain			
			Extracted from 2-layer model		Extracted from 3-layer model	
	Distortion (mm)	Computational time (min)	Distortion (mm)	Computational time (min)	Distortion (mm)	Computational time (min)
3	**0.584**	43.7	**0.534**	2.1	**0.553**	2.8
5	**0.937**	57.6	**1.024**	2.5	**1.063**	3.2

To verify that the proposed method is an efficient approach with low computational effort, comparison between the proposed method and detailed process simulation has been provided in terms of the computational effort required. Table 2.8 shows computational times for the straight five-layer single-walled deposition case in the full-scale detailed process simulation and the MISM, respectively. Note that the proposed method allows the computational time to be reduced by ~20 times. Clearly, this comparison demonstrates the good computational efficiency of the proposed method.

2.5 Practical ISM based on Small-Scale Detailed Simulation

2.5.1 Description of Proposed Method

Inspired by the assumption that nearly all the elements in a deposition line experience similar physical process, the entire length of a long deposition line does not need to be considered in the representative volume model. Therefore, for the LENS process concerned in this dissertation, how to determine a reasonable small-scale model has been investigated to extract the mean inherent strains for different single-walled structures. This section introduces details of the small-scale model with particular emphasis on the following three aspects:

(1) Determination of the small-scale model

The geometry of the small-scale model for the LENS process should be a two-layer line deposition model. It is also reasonable to use a three-layer deposition model if the computational cost can be afforded. However, the benefit of utilizing a three-layer deposition as the small-scale model is little, as the mean inherent strains extracted from the two-layer and three-layer single-walled model are very close to each other.

The size of the two-layer small-scale model depends on the specific DED process parameters including laser power, scanning speed and powder feed rate. For the process parameters employed for LENS processing of Ti64 in this dissertation (laser power 300W, scanning speed 2.0 mm/s and powder feed rate 6~8 rpm), the size of the small-scale two-layer model can be defined as $20\times2.0\times1.8$ mm^3 as shown in Figure 2.17(a). Note the length for the small-scale process model should be selected to ensure that the temperature along the scan line in the simulation reaches steady state. (The inherent strains will then be extracted from the steady state region as steady state behavior is dominant in most structures of interest.) The heat source should move far away

from the starting end to ensure that the temperature contour maintains a stable shape with a comet-like tail over the layer (see Figure 2.17(b), for example). The mesh dimension of the two-layer small-scale model is shown in Figure 2.17(a). As a common practice [27, 28, 35], one element through the thickness is employed to model one single layer. For the element mesh along the laser scanning direction, given the laser beam diameter (~0.6 mm) of the LENS machine, the layer is meshed with 40×3 elements in the length and width dimension (see Figure 2.17(a)). Employing the element birth and death method, 50 load steps are used to simulate the deposition process of one single layer.

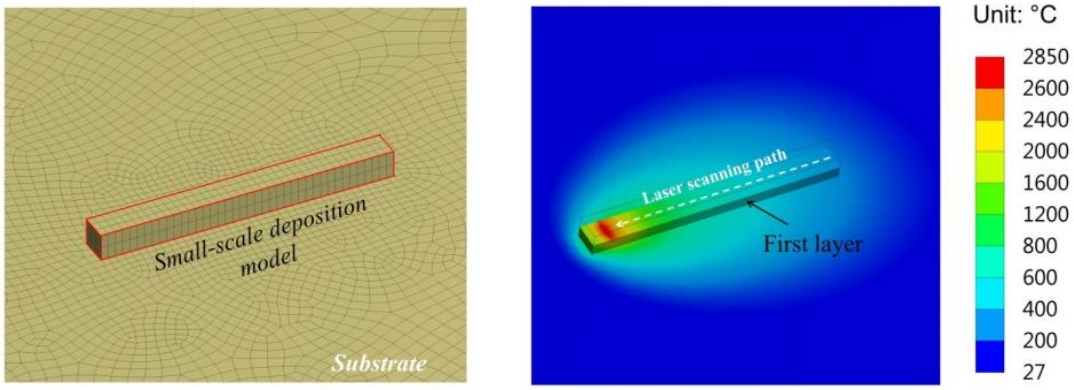

(a) (b)

Figure 2.17 Typical Features of the Small-Scale Model: (a) Geometry and Mesh Model and (b) Stabilized Temperature Contour in a Deposition Layer

(2) Evaluation of mean inherent strain

After the small-scale simulation is finished, the elastic and plastic strain history of any material point in the deposition can be recorded conveniently using APDL commands. Material points in the centerline of bottom layer in the small-scale model are selected as the sampling points to compute the mean inherent strain. The elastic and plastic strains in the intermediate and steady

states of the selected sampling points are obtained from the small-scale simulation results. Then the inherent strains at each sampling point can be computed based on the modified inherent strain definition given in Eq. (2.16). For the strain component parallel to the laser scanning direction, the inherent strains are summed up and averaged over the entire layer dimension to obtain the mean inherent strain component. Similarly, the same procedure is carried out for the remaining two inherent strain components perpendicular to the laser scanning path and in the build direction. In this manner, the three normal components of the mean inherent strain vector can be evaluated. In this section, the mean inherent strain vector based on the small-scale model is determined to be (-0.0069, -0.002, 0.008) and will be applied to the rectangular contour deposition model to verify its accuracy.

(3) Application to a different single-walled structure

These normal inherent strains are averaged into an inherent strain vector as discussed above. To implement this conveniently in commercial FEA software, the mean inherent strain vector is treated as orthotropic CTEs for the large model. The rectangular contour wall deposition model is considered as a different part to illustrate the application of the mean inherent strain extracted from the small-scale detailed simulation model. Note that the in-layer components of the mean inherent strain vector correspond to the directions parallel and perpendicular to the laser scanning direction. However, since the laser scanning changes direction on different sides of the rectangular contour deposition model and forms a closed contour path, a reasonable way is to apply the averaged magnitude for the in-layer components of the mean inherent strain vector to the layers containing different laser scanning paths. Therefore, the mean inherent strain vector for each layer of the rectangular contour becomes (-0.0045, -0.0045, 0.008) after averaging and is then applied uniformly to each layer of the rectangular contour wall model. The layers in the large model are

activated layer-by-layer, and a unit temperature increase is applied to the newly activated layer to introduce the inherent strains as initial strains. Generally, the mean inherent strain obtained through the small-scale simulation can be applied to different single-walled structures and predict residual deformation efficiently.

2.5.2 Results and Discussion

The predicted maximum vertical deformation of the 5-layer and 10-layer rectangular deposition model using the new mean inherent strain vector is shown in Table 2.8 together with results obtained from full-scale detailed process simulation.

Table 2.8 Maximum Vertical Deformation of the Rectangular Contour Deposition Model Using Full-Scale Process Simulation and the MISM based on Small-Scale Process Simulation

Cases	Maximum vertical deformation (mm)		
	Full-scale process simulation	MISM	Error (%)
5-layer	1.157	1.181	2.1
10-layer	1.622	1.780	9.7

In addition, the vertical residual deformation profile of the ten-layer rectangular contour deposition model is shown in Figure 2.18. Clearly, compared with those full-scale simulation results, good agreement can be observed, and the MISM based on the small-scale simulation is successfully validated when applied to a different model. Nonetheless, a possible explanation for the relatively large error in the ten-layer case is that, during deposition of large parts, the workpiece

experiences different thermal energy transfer. As a result, the re-melting zone changes during the deposition process, and it is normally larger with increasing distance from the substrate. This phenomenon could affect the extracted inherent strains, and it may be inappropriate to use the same mean inherent strain vector for all the layers in a large AM build.

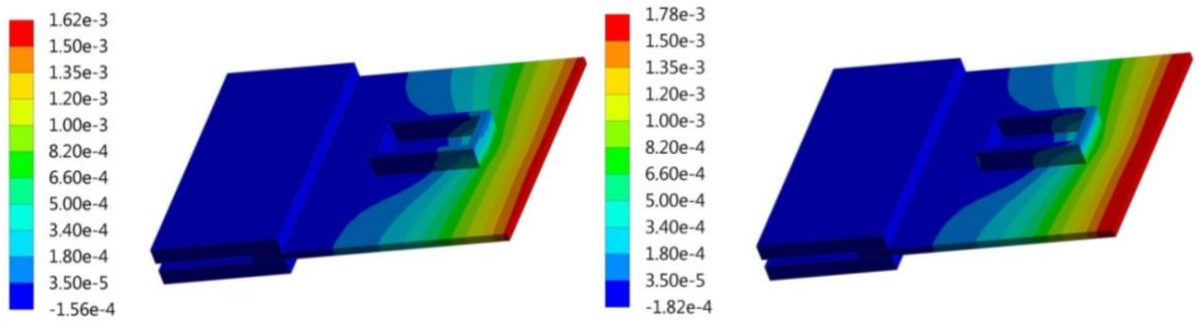

(a) (b)

Figure 2.18 Predicted Distribution of Vertical Residual Deformation (Unit: m) of the 10-Layer Rectangular Contour Deposition by (a) Full-Scale Process Simulation (b) Mean Inherent Strain Vector Method

Regarding efficiency of the proposed method, the computational times of the two new cases of the five-layer and ten-layer rectangular contour deposition models are shown in Table 2.9. The time needed for the small-scale simulation model (33.8 mins) has been added to the total computational time for the modified inherent stain method since it also takes time to evaluate the mean inherent strain vector. As shown in the table, even with the small-scale simulation time included, the MISM is still much more efficient (10~15x speedup) than the full-scale detailed thermomechanical simulation. And if only the time it takes to execute the MISM is considered, the improvement of the computational efficiency can be nearly 80 times.

Table 2.9 Comparison of Detailed Process Simulation and the MISM in Terms of Computational Efforts Required for the 5-Layer and 10-Layer Rectangular Contour Deposition Model

Cases	Computational time (min)		
	Full-scale detailed process simulation	MISM	
		Including small-scale simulation	Excluding small-scale simulation
5-layer	439.2	38.4	4.6
10-layer	610.2	42.2	8.4

Additionally, the same mesh is used when the obtained inherent strains are applied back to the deposition models in this chapter. The benefit of doing this is that the inherent strains can be applied in a convenient element-by-element manner. If the mesh size of the detailed simulation model is different from that used for the estimation of the residual distortions, the calculated inherent strains could be mapped to the model as a function of the location of the elements. For the model used for the detailed process simulation, the locations of those elements in the HAZ can be normalized to a standard range as seen in Figure 2.8. Then for the model with a different mesh used for the prediction of the residual distortions, as for any element in the HAZ, according to its normalized location, the amount of the inherent strains to be assigned to the element can be calculated by interpolation using the normalized curves.

2.6 Conclusions

In this chapter, the MISM is proposed for fast prediction of residual distortion of single-walled structures produced by a representative DED process in LENS. Specifically, a modified

model is proposed to estimate the inherent strains from detailed process simulation, which are then applied to the part model to perform a layer-by-layer static analysis to simulate residual distortion. To validate the proposed model, the inherent strains obtained from full-scale detailed simulation of the entire structure under consideration are applied back to the structure to predict residual distortion by static equilibrium analysis. The structures employed to validate the model include a single wall and rectangular contour wall by the LENS process. The accuracy and efficiency of the proposed method has been demonstrated by both numerical examples and experiments.

As a first step to make the proposed method practical, the mean inherent strain concept is then proposed and extracted based on full-scale two-layer and three-layer line deposition models. Numerical examples have demonstrated that the mean inherent strain can be applied to single-walled structures having more layers to accurately predict the residual deformation much faster. To make the method truly practical, a small-scale detailed simulation model is proposed to extract the mean inherent strains, which are then applied to different single-walled structures for fast residual deformation prediction. Simulation results show that the MISM is quite efficient, while the residual distortion of AM parts can be accurately computed within a short time.

The assumption that most of the deposition lines experiences the same melting and re-melting process in the AM process may not be true in some cases. When the scan speed is high and the part is large, the workpiece may experience different thermal energy transfer due to the boundary effects of the substrate and the previous deposition layers with high temperature. In other words, the sampling positions of the small-scale model from the large part may also have some effects on the extracted inherent strains. To tackle this problem, further research is needed to investigate the temperature gradient in the deposition by performing many more detailed process simulations and experiments.

The modified inherent strain model is proposed based on single line depositions on top of each other, and hence validity of the model has been demonstrated only on single-walled structures in this dissertation. The proposed model will need to be extended in order to treat more complex geometries consisting of scan lines not only on top of each other but also next to each other. For a large AM build, clearly it is impossible to simulate all the lines and layers before extracting the overall inherent strains. In addition, usually complex geometries may be deposited using complex laser scanning patterns in the AM process including DED and PBF. The influence on the inherent strains by the process parameters such as the laser scanning path needs to be considered further. Thus, the detailed depositing path needs be modeled in the simulation of a local region of the large part. This also means that simulating only a straight deposition line is not sufficient for computing the inherent strains accurately for complex geometries. Rather, a small section may be used as the representative volume to obtain the inherent strains necessary to simulate deformation of a large complex part efficiently. Further research is needed to investigate this approach and the associated accuracy and efficiency.

3.0 MISM for PBF Components

3.1 Current Simulation Methods for PBF Components

The powder bed fusion (PBF) process is currently the most popular AM process for manufacturing complex metal parts in the industry. For example, techniques such as direct metal laser sintering (DMLS) [32, 60, 61], selective laser melting (SLM) [62-64] and electron beam melting (EBM) [65-68] are all powder bed based. In general, a metal component is built out of a powder bed via repeated micro-welding process. At the macroscopic scale, different AM systems involving a high energy beam are generally based on similar physical process like melting and solidification of metal materials. Typically, large temperature gradient and high cooling rate will occur due to intensive heat source and large local energy density [55], which consequently leads to large thermal strain and hence significant residual stress or deformation in the metal components. These are both undesirable as large residual deformation makes it difficult to post-process parts to achieve the desired dimensional accuracy, and residual stress can cause cracking during the build. Therefore, it is of critical importance to predict residual stress and deformation in the process such that the quality of the printed components can be guaranteed.

In the past, residual deformation and stress were predicted through fully coupled thermomechanical simulations [28, 69, 70] based on heat source models [49, 53, 71], which is very time-consuming. Moreover, for the complex metal parts, it is very difficult to compute the residual deformation through these detailed process simulations, since a part may contain thousands of thin layers containing numerous scan tracks. Limited by computational power, it is very difficult to predict residual deformation of large-scale AM parts by detailed thermomechanical simulation

directly. Even with a coarse layer-by-layer analysis pattern [72, 73], it still takes many hours to obtain the final residual deformation of the AM builds. To achieve a faster prediction, some alternatives were developed based on welding mechanics such as the inherent strain theory [37, 39, 40]. This method was first established to calculate the residual deformation in metal welding problems. However, conventional ISM was proved to be inaccurate when applied to predict residual deformation in complex AM process. Similarly, the applied plastic strain method [42, 43] was proposed to simulate residual deformation of an LENS deposited part. However, it was found that the accuracy of this method is not adequate when applied to large AM builds. In the past years, Keller et al [45] and Alvarez et al [74] proposed some possible values of inherent strain used to efficiently predict the residual deformation of the AM components. Nonetheless, the detailed theory and method of determining inherent strain in the AM builds were not presented. Recently, an empirical methodology was proposed to determine the inherent strain values in the SLM-printed components [75]. Through iteratively optimizing the difference between the predicted residual distortions and the experimental results of double cantilever beams, reasonable inherent strain values can be determined to ensure good prediction accuracy compared with the experiments. This empirical method is expensive since many metal samples need to be manufactured and large computational work is required in the numerical optimization process. In addition, the present authors proposed the modified inherent strain theory [76] to compute accurate inherent strain in single-walled structures consisting of single line depositions by the LENS process. However, the validity of the modified theory has not been demonstrated when applied to the DMLS process employing more complex scanning strategies such as the rotational laser scanning paths in different deposition layers. Moreover, it has not been fully revealed how to predict the residual

distortion accurately and efficiently for a large and geometrically complex DMLS component containing many thin layers based on the modified inherent strain model.

3.2 MISM Adapted for PBF Process

In a typical AM process, new layers are formed out of the metal powder bed all the time during the multi-track laser fusion process, which will cover those lower layers and act as a mechanical constraint for them. The layer-by-layer shrinkage of the upper layers will also contribute downward to the evolution of the elastic deformation and stress in the lower depositions. Consequently, the assumption in the early method that only the plastic strain in the final equilibrium state of the weld matters as the inherent strain will be invalid when applied to the layered AM process. The inelastic strains are highly dependent on the boundary conditions including mechanical and thermal boundary, plate dimensions, and fixtures like the large substrate as the constraint in the DMLS process, etc. The inherent strains in the metal part have to be determined case by case since many factors, even like the input laser power can influence the time-dependent accumulation of inelastic strains. This makes the application of this method expensive in time. Nonetheless, physically in the AM builds, many layers are subjected to same kind of thermal expansion and shrinkage caused by the moving thermal loading, and similar mechanical restraints like the constraint by the already deposited cooled layers. As a result, the accumulation of their inelastic/inherent strains will be very similar. Therefore, it is believed that only a small representative volume needs to be fully simulated to look into the accumulation of the inelastic strains in the thermal and mechanical equilibrium process of AM. Then the typical inherent strains

can be extracted and applied to the layers in the large part. In this way, significant gain in time can be obtained.

In order to obtain accurate inherent strain values, the amount of thermal strain that is converted into mechanical strain responsible for residual deformation (so-called inherent strain) needs to be captured. In the proposed theory, the inherent strain in the layer-by-layer AM process is a processing-history-dependent quantity, rather than being only dependent on the final cooled state as in the original theory. Besides the generated plastic deformation as a definite source in the proposed inherent strain model, new strain terms are added to account for the evolving elastic deformation due to the layer-by-layer shrinkage in the cooling process, which represents conversion of some of the thermal strain coupled with the influence of the inter-layer constraint. Therefore, the modified inherent strain theory is proposed specifically to adapt to the AM process, and two major sources for the inherent strain are considered.

(1) Contribution from plastic deformation. Large compressive plastic strain is generated once the powder is sintered by the laser beam and rapid solidification of material occurs. The plastic strain incurred during rapid solidification is considered to be a direct conversion of the thermal strain. Given a material point already deposited, in the following cooling-reheating-cooling process, the plastic strain changes due to the temperature increase and decrease. However, compared with the evolution history of the elastic strain, the change of the plastic strain is not so significant. For convenience of discussion, the instant when the compressive plastic strain reaches its maximum due to the rapid solidification phenomenon is defined as the "intermediate state". Based on the above assumption, contribution of the plastic deformation to the inherent strain of the AM process is written as:

$$\boldsymbol{\varepsilon}_p^* = \boldsymbol{\varepsilon}_p^I \tag{3.1}$$

(2) Contribution from thermal shrinking coupled with inter-layer effect. In the original method, the induced inherent strain in the welded part is assumed to be equal to the residual plastic strain, given that the thermal strain quickly vanishes after the heating-cooling cycle and thus has no effect on the change of mechanical strain. In order to adapt the original ISM to model the metal AM process, the influence of thermal shrinkage is further considered coupled with the evolving mechanical constraint and inter-layer effect due to the deposition of new layers on the residual deformation and stress. For a material point under consideration, its intermediate state is considered the beginning of the accumulation of the elastic deformation. After the intermediate state, the elastic deformation at any material point will be changed by thermal shrinkage of the surrounding solid and the layer-by-layer overlaid solid materials until the entire part reaches the end of the cooling process, which is defined as the "steady state". This change of elastic strain during the cooling process represents the conversion of thermal strain into mechanical strain that needs to be accounted for in the modified model for AM. Since no heat transfer simulation is performed in the original ISM, this change in elastic strain is thus added to the plastic strain, which becomes the modified model for AM. In fact, the property of the additional source in the modified inherent strain model is still not elastic. The contribution to the inherent strains in the AM process can be written as:

$$\boldsymbol{\varepsilon}_{th}^{*} = \boldsymbol{\varepsilon}_{e}^{I} - \boldsymbol{\varepsilon}_{e}^{S} \tag{3.2}$$

where $\boldsymbol{\varepsilon}_{e}^{I}$ and $\boldsymbol{\varepsilon}_{e}^{S}$ denote the elastic strain at the intermediate and steady state of the specific AM process, respectively. The intermediate state is the same with the one defined in Eq. (2.15).

Finally, the modified inherent strain model proposed can be written as:

$$\boldsymbol{\varepsilon}^{*} = \boldsymbol{\varepsilon}_{p}^{*} + \boldsymbol{\varepsilon}_{th}^{*} \tag{3.3}$$

As the modified theory indicates, the residual deformation is inherently induced by the heat input and influenced by the inter-layer effects of the evolving mechanical boundaries as new layers

are deposited onto the previous ones. The inherent strain is employed to quantitatively capture the deformation considering the thermal history and the inter-layer mechanical constraint in the AM process. In practice, the inherent strain model will be utilized to extract the typical inherent strain values from a small-scale detailed process simulation for a given AM process. And then the obtained strain values will be applied to the entire metal part to predict the residual distortion. This method is proved to be valid when the process has a build pattern that repeats itself periodically, as will be demonstrated for the DMLS process next.

3.3 Calculation and Application of Inherent Strain

3.3.1 Calculation of Inherent Strain

The small-scale detailed process simulation of the DMLS processing of Ti64 and Inconel 718 is presented below based on FEA. Since the detailed process model for DMLS in this chapter is adapted from that of the LENS process discussed in Ref. [55], only the pertinent details specific to the DMLS process are given and only a brief description of other details is provided hereby. In the detailed simulation, temperature-dependent material properties such as the coefficient of thermal expansion (CTE), Young's modulus, and yield strength [30, 55] are employed. The DMLS system has different scanning modes using different process parameters. The core-skin mode will be simulated as it is the dominant mode for printing the core volume of a metal component. The process parameters of this print mode for Ti64 and Inconel 718 are listed in Table 3.1.

Table 3.1 Default DMLS Process Parameters of the Core-Skin Mode for Ti64 and Inconel 718

Process parameters	Laser power/W	Scanning velocity/(m/s)	Layer thickness/μm	Laser beam diameter/μm
	200-300	0.95-1.25	30	100

In the core-skin mode, a single layer is divided into multiple hatches, each having the same width. The hatch orientation rotates an angle of 67° when a new layer is deposited. This rotation angle is the default option for printing Ti64 and Inconel 718 parts in the DMLS process. A reason for such a choice is that the laser scanning strategy using such a rotation angle of 67° can give the least directional stress difference inside the deposited layers in the metal part [27]. Inside the hatches, the laser beam scans back and forth in an S-pattern with scan lines perpendicular to the hatch lines. This feature will be considered in the small-scale simulation in order to better match the DMLS process. A thin rectangular deposition is defined as the representative volume, containing two layers with a size of $0.6\times0.3\times0.06$ mm^3. In the first layer, the laser beam moves along a straight line for three consecutive tracks. In the second layer, the laser path rotates an angle of 67° and forms eleven tracks as shown in Figure 3.1(a). The two-layer model is deposited onto a large substrate of the same material of which the bottom surface is fixed as the boundary condition.

There are three reasons why a thin rectangular 2-layer deposition is chosen as the representative volume. First, since the micro-welding process is similar in each layer of the large build as the basic assumption, it is not necessary to simulate many layers to investigate the AM process. However, the influence of the laser scanning strategy on the inherent strain has to be considered. Since the laser scanning process has a rotation angle for each layer, at least two layers have to be included in the simulation model to reflect this feature. Second, when a new layer is

deposited, the re-melting process of the previous deposition has important influence on the redistribution of the elastic and plastic strain in the deposited layers. Meanwhile, the inter-layer effect between two adjacent layers will also affect the mechanical strain in the deposition. A 2-layer deposition model is able to consider all these important factors mentioned above. Third, the detailed thermomechanical simulation is computationally expensive because very fine mesh and small time steps have to be employed to ensure the accuracy of the numerical analysis. In order to reduce the computational cost, simulating many layers in the representative volume should be avoided. Thus, the thin rectangular 2-layer model as the representative volume is chosen for the small-scale simulation. More thin layers can be created below the concerned layers to represent the already deposited ones. Since the temperature drops very quickly in the already deposited layers, it is acceptable to use room temperature as the initial thermal boundary condition for those layers. The large substrate then provides the appropriate thermal and mechanical boundary conditions for the entire model. However, in this way the small-scale model will give similar inherent strain results compared with the only 2-layer model according to the simulation trials. This phenomenon is reasonable because the already deposited layers work like the substrate constraint. As a result, the influence is negligible when only large substrate without already deposited layers is used as the constraint for the representative volume model. Compared with the manner of extracting the inherent strain values for LENS based on a 2-layer small-scale simulation in Ref. [76], a lot more deposition lines are modeled around a concerned line in the lower layer out of the 2-layer model. The reason is that the DMLS process has higher and more localized laser intensity and usually its physical deposition layers are much thinner than those in LENS. The neighboring deposition lines including the adjacent upper layer will affect the mechanical strain

evolution of any concerned material point in one deposition line of the lower layer. As a result, the inherent strain for the lower layer will also be influenced greatly.

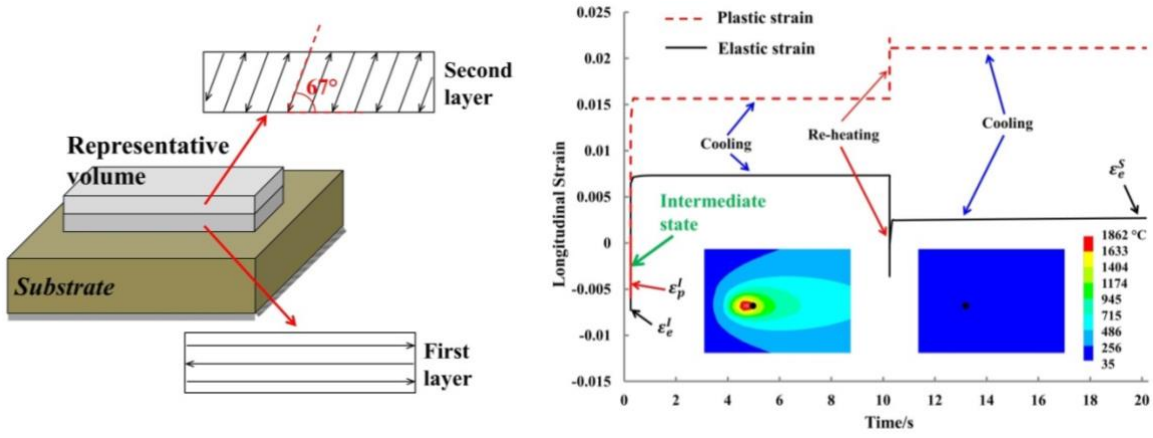

(a) (b)

Figure 3.1 Small-Scale Model: (a) a 2-Layer Representative Volume on the Bottom-Fixed Substrate and the Laser Scanning Strategy, and (b) Illustration of the Intermediate and Steady State of a Ti64 Material Point (Black Dot)

The actual process parameters for Ti64 in the micro-mechanical model are as follows: laser power of 280 W, laser beam diameter of around 100 μm, scanning speed of 0.95 m/s and layer thickness of 30 μm. As for Inconel 718, the laser power is 285 W and scanning speed is 1.0 m/s. The other parameters are the same with Ti64, for example, the laser energy absorption efficiency of 50% is used for both materials. The double-ellipsoidal heat source model [53] is employed in the small-scale process simulation. Detailed mathematical description of this heat source model can be found in Refs. [53, 55]. Its major feature is that the respective lengths of the longitudinal (a), transverse (b) and through-the-depth (c) semi-axes of the ellipsoidal laser beam can be different. Values of the semi-axes of the heat source model are determined based on the practical process parameters in Table 3.1. For both materials, the values of a and b are equal to the radius

(50 μm) of the laser beam. The value of the depth c is determined as 90 μm through experiments, which equals the thickness of three thin layers in the DMLS process.

The involved laser scanning pattern in this chapter is a typical scanning strategy in the DMLS process. In addition, besides the core-skin scanning mode, there are other scanning modes such as the island scanning used by other AM systems. However, even though the scanning patterns are different for different layers, the proposed method can still be employed. When more complicated scanning patterns are concerned, a small representative volume which contains only a few layers corresponding to the typical scanning patterns for different layers needs to be found. As long as the representative volume is established and the small-scale process simulation can be implemented, the MISM can be employed, for both the extraction of the inherent strain values and the prediction of the residual deformation. Nonetheless, the sacrifice is that the computational cost will be expensive since more layers have to be considered to reflect the different laser scanning patterns for different layers.

Based on the small-scale simulation of the two-layer Ti64 model, one typical material point (black dot in Figure 3.1(b)) is chosen and the longitudinal elastic and plastic strain in the direction of the horizontal laser scanning path (see first layer in Figure 3.1(a)) are plotted in Figure 3.1(b). The drastic jumps of the curves indicate the heating and re-heating when the laser beam passes the point (left temperature map in Figure 3.1(b)). And the nearly flat sections indicate the steady cooling process (right temperature map in Figure 3.1(b)). The intermediate and steady states of any material point in the DMLS process will be identified based on the strain history in Figure 3.1(b). This figure shows the typical and necessary nodal strain terms in FEA to calculate the averaged elemental inherent strains as defined in Eqs. (3.1~3.3). For the lower one of the two layers, it experiences complete melting, re-melting, and relaxation process. Thus, the lower layer

can be used as a representative layer to represent the inherent strain of any layer in a large component. If a material point in the lower layer is concerned, the elastic and plastic strain history can be tracked directly based on the small-scale simulation. Note from Figure 3.1(b) that large compressive elastic and plastic strain are generated at the very beginning of the strain history. This phenomenon indicates the rapid solidification process, that is, the intermediate state. Then the elastic and plastic strain will develop into tensile strain very rapidly and reach steady state following the intermediate state, indicating that the rapid solidification finishes in an extremely short time. This feature is the most common characteristics of the mechanical strain evolution for different metal AM processes including DMLS and SLM using a high energy beam source.

As shown in Figure 3.1(b), the compressive elastic and plastic strain reach their maximum at the same time, which is defined as the intermediate state (annotated in Figure 3.1(b)). Then tensile strain starts to accumulate due to the instant solidification. For the first term in the modified inherent strain model, the plastic strain at the intermediate state is extracted from the small-scale simulation results. Then the difference of the elastic strain at the intermediate and steady state is calculated as the second term in the modified model. The inherent strain equals the sum of the two terms. In this way, the inherent strain of any material point in the first layer can be calculated. Regarding numerical implementation based on FEA, some simplifications have to be adopted. Constitutively, the strain and stress terms are second-order tensors in continuum mechanics theory. For the isotropic material, symmetry in the stress/strain and elasticity tensors will be utilized to simplify the independent components. Finally, only six independent components in the strain/stress tensor are needed for the isotropic material model in three-dimensional problems. By rearranging the indices of the components, the tensors can be reduced into lower-order forms like vector and matrix. As for the strain vector, it contains six components including three normal strain

components (ε_{xx}, ε_{yy}, ε_{zz}) and three shearing strain components (ε_{xy}, ε_{yz}, ε_{xz}). The detailed process simulation shows the shearing strains are of much smaller magnitude compared with the normal strain components [76]. The physical reason is that the normal expansion and shrinkage in the in-plane dimension of the thin layer are the major cause of the residual deformation and stress instead of the shearing effect. Therefore, the three shearing strain components are neglected for simplicity and the inherent strain vector will only consist of three normal strain components.

Many details of the procedure of extracting the three normal inherent strain components have been fully covered in Ref. [76]. Even for the DMLS process, when the modified inherent strain model is applied, the obtained inherent strain distribution curves share some similar features as reported in Ref. [76]. The components of the inherent strain in three directions distribute continuously and nonuniformly over the entire lower layer. The inherent strains are almost stable and flat in the middle section of the first layer, while the values have a drastic transition to nearly zero when the curves get close to the two ends of the layer. This characteristic indicates the influence by the difference of the thermal and mechanical boundaries on the inherent strains. The local material at two ends of any layer has quite different cooling boundary conditions and weaker mechanical constraint compared with the materials in the middle bulk volume of a large build.

The most significant feature is that the inherent strain has two compressive in-plane components and one tensile component in the build direction. The positive sign of the strain component in the build direction may reflect the Poisson effect in the mechanical deformation. Due to the small thickness compared with the other two dimensions of a single layer, temperature gradient in the in-plane directions is very different from that in the layer-thickness dimension (build direction). As a result, the in-plane strains have dominant Poisson effect on the strain in the build direction. Moreover, the mechanical constraint for a layer in the build direction is weaker

than the in-plane directions. The thin layer is easier to shrink normally in the build direction. Due to coupled effect by the in-plane strains and the mechanical constraint, the positive normal strain component is obtained for the inherent strain in the build direction. The above analysis explains why for the upper layer in the fine scale model, it is found that the normal stress is quite small (not exactly zero) compared with the lower layer while the normal strain in the build direction is non-zero in the inherent strain vector.

3.3.2 Applying Inherent Strain to Part-Scale Model

In the metal DMLS process, if the same process scanning path is applied, the micro-welding phenomenon in each layer of the large deposition will be quite similar. The elastic and plastic strain history of each layer is quite similar and as a result, the extracted inherent strain values for the elements in each layer will be close. Thus, the same inherent strain can be applied to each layer of the large build for simplification. Nonetheless, for a large and complex deposition containing thousands of thin physical layers, the thermal cycle in the build direction can have some influence on the inherent strain of the deposition layers in different heights. It is reasonable that if varying inherent strain values are applied to the layers with respect to the build direction, the accuracy of the MISM can be improved. However, expensive computational cost is required to figure out the reasonable trend of the inherent strain against the increasing height of the deposition layers.

As a preliminary trial, the average inherent strain values when the laser scanning is at steady state will be applied uniformly to each deposition layer, since the processing is dominated by steady-state scanning. Following the above discussion, a mean inherent strain vector (ε_{xx}^*, ε_{yy}^*, ε_{zz}^*) is obtained from the small-scale simulation and will be employed to predict the

residual deformation of a large DMLS part. In addition, based on the thermomechanical simulation, it is found that the rotational laser scan pattern has a redistribution effect and makes the inelastic strains homogenous especially in the in-plane dimensions. Therefore, it is reasonable to assume that the same value for the in-plane components of the inherent strain vector can be used in this dissertation, i.e. $\varepsilon_{xx}^{*} = \varepsilon_{yy}^{*}$. Since the inherent strain is calculated based on the small representative volume out of a large part, it is reasonable to apply the inherent strain vector in a layer-by-layer manner, as shown in Figure 3.2, in the static FEA with elastoplastic constitutive model. However, a couple of top/final layers will not have the same kind of thermal loading since they will not experience multiple remelting occurrences like the lower layers. The inherent strains in the final layers will be a little different from those lower layers. In this chapter, this effect is ignored because the several final layers are only a very small section of the large metal part. Regarding the first several layers, though they are exposed to the constraint of the large substrate directly, it has been shown in the earlier work [76] that it is reasonable to assume the first few layers have the same inherent strains with most layers in the bulk volume of the large part. Other factors that may challenge the applicability of the mean inherent strain vector uniformly loaded in the build direction, such as the part geometry containing changing width or local overhang features, are not considered in this chapter.

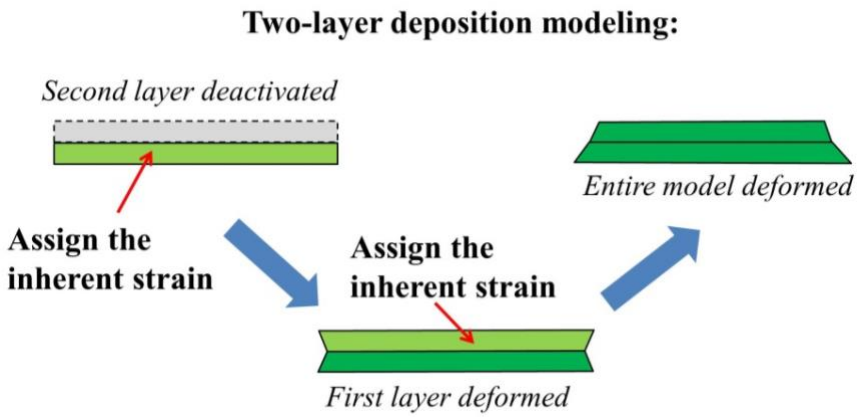

Figure 3.2 2-Layer Example for Illustration of the Layer-by-Layer Method of Assigning Inherent Strain

In order to adapt to the layer-by-layer loading of the inherent strain, the metal part will be meshed into slices in FEA to ensure the part model has a flat top surface in any height in the build direction, just like the way in the practical DMLS process. The inherent strain obtained from the small-scale model can be used to predict the residual deformation of any complex part if the same process parameters are applied, without the need to perform the small-scale detailed process simulations again. Note the same process parameters mainly suggest that the laser power, scanning strategy and the scanning speed are same. Otherwise, the small-scale simulation based on the representative volume should be performed again to obtain accurate strain history for extraction of the inherent strain.

Usually a large metal component may contain thousands of physical layers deposited by the DMLS process. It is impractical, if not impossible, to simulate all the layers even by the ISM. Therefore, many thin physical layers are lumped into one equivalent numerical layer (or named super layer [77]) in the static analysis. When the equivalent layer is employed to replace many thin physical layers, the mean inherent strain vector is applied as the orthotropic CTEs of the layer. And a unit temperature increase is applied to the equivalent layers in a layer-by-layer manner as

the load, in order to simulate the effect of the bottom-to-top manner of the AM process (see Figure 3.2). With the body force of the metal depositions neglected, the governing equation for the layer-wise mechanical analysis of the large-scale components can be written as follows:

$$\boldsymbol{\nabla} \cdot \boldsymbol{\sigma}^i = 0 \tag{3.4}$$

where $\boldsymbol{\sigma}^i$ denotes the stress tensor of the metal component when the *i*th layer is printed onto those already deposited layers. If one layer is simulated by a load step in the FEA, Eq. (3.4) indicates the governing equation for the *i*th load step. Element birth and death technique is employed to simulate the bottom-up material depositing process. All the layers are killed/deactivated in the very beginning. Then each layer is activated step-by-step in the vertical build direction. Those already deposited layers have an active status and behaves like mechanical constraint to the upper activated layers.

The elastic stress tensor in Eq. (3.4) is calculated based on the elastic constitutive law as follows:

$$\boldsymbol{\sigma}^i = \boldsymbol{D} : \boldsymbol{\varepsilon}_e^i \tag{3.5}$$

where $\boldsymbol{\varepsilon}_e$ denotes the elastic strain and $\boldsymbol{D}$ denotes the constitutive elastic tensor. Related to the definition of $\boldsymbol{\sigma}^i$ after Eq. (3.4), the explicit definition of $\boldsymbol{\varepsilon}_e^i$ is the elastic strain field of the metal component when the *i*th layer is printed onto those already deposited layers.

Regarding how to load the inherent strains to induce inelastic strains, thermal expansion strains are considered as a suitable form. Since there are three normal strain components in the inherent strain vector (ISV), the inherent strains are defined as orthotropic coefficients of thermal expansion (CTEs) in the material property parameters. In order to cause the thermal deformation, simply a unit temperature increase can be treated as the thermal load. When thermal strain exists in the mechanical analysis, the total strain in the large-scale component is computed as follows:

$$\boldsymbol{\varepsilon}_{tot}^{i} = \boldsymbol{\varepsilon}_{e}^{i} + \boldsymbol{\varepsilon}_{p}^{i} + \boldsymbol{\alpha}^{*}\Delta T^{i} \tag{3.6}$$

where $\boldsymbol{\varepsilon}$ and $\boldsymbol{\varepsilon}_p$ denote the total and plastic strain, respectively. Elastoplastic material constitutive model is used and the $J2$ plasticity model is adopted to describe the plastic behavior of the material. $\boldsymbol{\alpha}^{*}$ represents the equivalent CTEs which are equal to the ISV. ΔT denotes the unit temperature increase applied to each deposited layer to induce the thermal strain. It just suggests a direct way of loading inherent strains in the layer-by-layer simulation. In addition, the total strain $\boldsymbol{\varepsilon}$ is formulated as follows:

$$\boldsymbol{\varepsilon}^{i} = \frac{1}{2}\left[\boldsymbol{\nabla u}^{i} + \left(\boldsymbol{\nabla u}^{i}\right)^{T}\right] \tag{3.7}$$

where $\boldsymbol{u}^{i}$ denotes the displacement field when the *i*th layer is added to the already activated layers of the model. In particular, in the layer-wise simulation, the displacement field is updated in each load step while taking the displacement solution of the previous step as the initial conditions.

In addition to Eq. (3.4), boundary conditions should be set up according to the practical manufacturing scenarios. For the PBF process, usually the metal powders are deposited on a fixed large and thick build plate in practice. Therefore, in the simulation, the boundary condition is to clamp the bottom surface of the build plate. However, according to the knowledge, the large and thick build plate forms a strong constraint to the bottom of the metal builds. Therefore, in order to save computational cost, the build plate can be neglected and the boundary condition becomes to fix the bottom surface of the metal components, accordingly. This boundary condition is adopted in this chapter.

The solution process can be easily implemented in any commercial FEA software like ANSYS Mechanical package. Using the element birth and death method, the equivalent layers will be deactivated at first and then activated layer-by-layer (see Figure 3.2). The shrinking deformation and stress relaxation effects of the activated layers are considered as the initial condition for the

following layer to be activated. Therefore, the accumulated shrinkage and stress relaxation effects in the thin physical layers are modeled equivalently by the shrinkage and stress relaxation of the equivalent layers. The numerical and experimental results have validated the accuracy of this equivalent procedure. The influence on prediction accuracy by the number of the equivalent layers will be investigated in the following section. Since only static mechanical analysis is required for the application of the inherent strain for an equivalent layer, the solution can be completed within a short time.

In summary for the proposed MISM when applied to the DED and PBF process, the general workflow for predicting residual stress and deformation of the AM metal components is shown in Figure 3.3. The critical input information mainly includes those process parameters such as laser power, laser absorption coefficient, scanning velocity and layer thickness. Through the workflow, residual stress and deformation are the final output of the MISM-based sequential analysis.

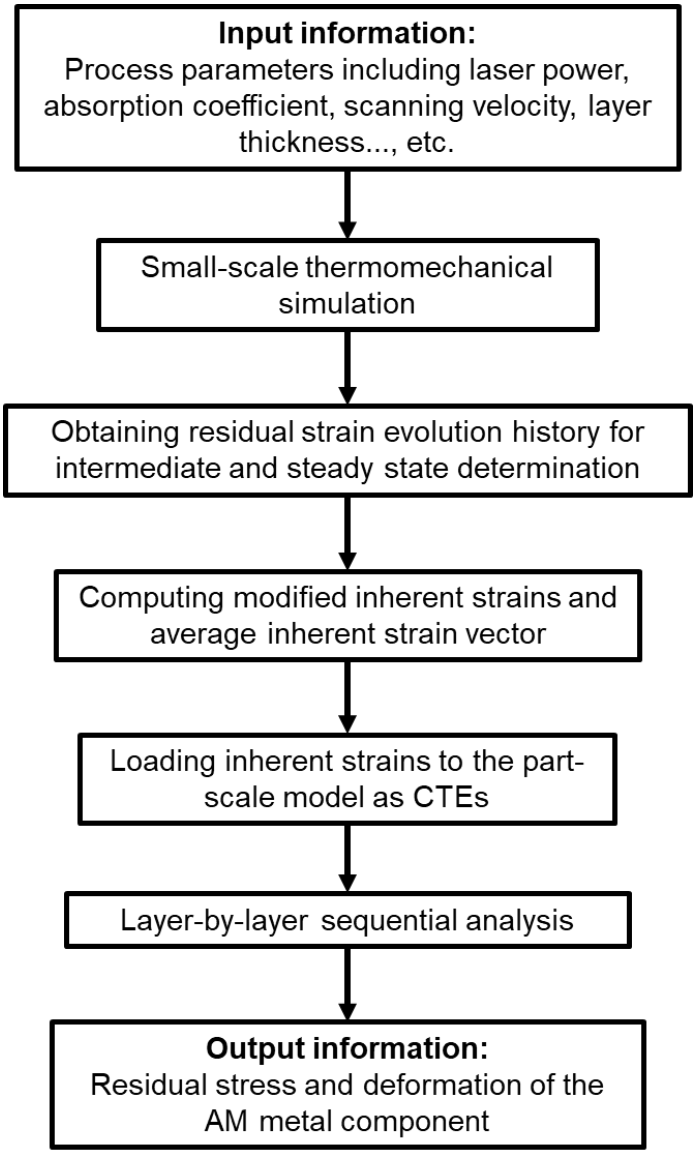

Figure 3.3 Workflow of the MISM-Based Simulation for Metal AM Process

3.4 Experimental Validation

3.4.1 Double Cantilever Beam

The double cantilever beam is a common benchmark employed to validate the numerical simulation of the AM process. The geometry model is shown in Figure 3.4(a). The length, width, and height of the double cantilever beam are 76.2 (3 inch), 12.7 and 18.35 mm, respectively. Support structures including two ramp blocks are added to the space beneath the beam since the large overhang cantilever beams cannot be printed by the DMLS process directly. The two cantilever beams were created after printing by cutting between the support structures and the beams on top. A convincing justification of this experiment design can be referred to the AM benchmark testing series (AM BENCH) [78].

The cutting caused the beams to bend upward from releasing the residual stress induced by the AM process, see Figure 3.4(b) for the Ti64 case. The total displacements of the Ti64 and Inconel 718 double cantilever beams were measured experimentally. The finite element mesh of the double cantilever beam and the substrate is shown in Figure 3.4(c). There are 110,694 elements in the entire model. Regarding the mechanical constraint in this case, the bottom surface of the substrate is clamped in all directions.

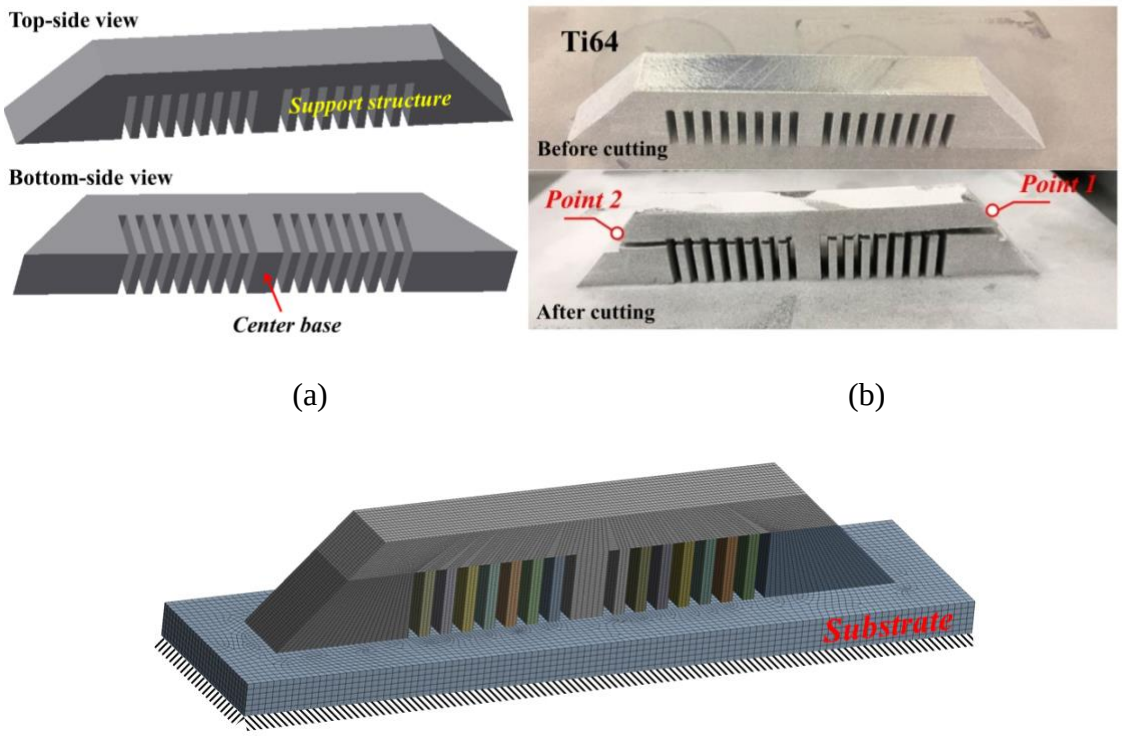

Figure 3.4 Double Cantilever Beam: (a) Geometry Profile; (b) Ti64 Deposition before and after Cutting off the Support Structures (Similar Phenomenon Also Observed in the Case of Inconel 718); (c) Finite Element Mesh of the Beam and the Substrate with the Bottom Surface Clamped

To show the accuracy of the modified method, first the inherent strain is extracted according to the definition in the original theory, that is, the plastic strain in the cooled steady state is taken as the inherent strain. The mean inherent strain vector is (-0.004, -0.004, 0.005) for Ti64, while (-0.006, -0.006, 0.004) for Inconel 718, where the components of the vector are parallel to scan direction in-plane, transverse to scan direction in-plane, and along the build direction. These inherent strain vectors are applied to a model with 60 equivalent numerical layers to compute the residual deformation of the beams, while the large substrate is fixed at the bottom surface all the time. After the layer-by-layer simulation finishes, material property having very small Young's

modulus will be assigned to the support structures, in order to release the residual stress inside the supports and simulate the cutting-off post processing.

For further comparison with experimental results, the total residual deformation of the beams is also obtained based on the modified inherent strain model proposed in this chapter. The mean inherent strain vector for Ti64 is (-0.012, -0.012, 0.01). The Young's modulus and yield strength for Ti64 used in the model are 104 GPa and 768 MPa, respectively. A different mean inherent strain vector of (-0.014, -0.014, 0.01) is employed in the Inconel 718 case, and the Young's modulus and yield strength are 205 GPa and 1000 MPa, respectively.

In all the cases, the total deformations of two center points (#1 and #2, see Figure 3.4(b)) in the two ends of the double cantilever beam are compared and shown in Table 3.2. It is expected the total deformation at the two ends of the double cantilever beam is different. The reason is that the support structures at the right end were removed first and most of the residual stresses, including those from the left side, were released, which resulted in smaller bending deformation at the left end after the remaining support structures were removed. In summary, the comparison shows the inaccuracy of the original inherent strain model, while demonstrating good accuracy (< 10% error) of the modified model for predicting the residual deformation of the DMLS components.

Table 3.2 Comparison of the Residual Total Deformation in the Simulated and Experimental Results

		Ti64			Inconel 718		
		Original method	Modified method	Experiment	Original method	Modified method	Experiment
Point #1	Deformation (mm)	0.64	0.87	0.94	0.41	0.54	0.58
	Error (%)	**31.9**	**7.4**	**---**	**29.3**	**6.9**	**---**
Point #2	Deformation (mm)	0.29	0.38	0.36	0.26	0.33	0.32
	Error (%)	**19.4**	**5.6**	**---**	**18.8**	**3.1**	**---**

Nonetheless, the obtained mean inherent strain vector for Ti64 leads to obvious underestimation of the total residual deformation of the double cantilever beam. More accurate prediction for the Inconel 718 component is observed compared with the Ti64 case in this example. One important reason is the influence of the phase transformational strain on the inherent strain values of the Ti64-based DMLS process. Therefore, it is necessary to include the phase transformational strain in the small-scale process simulation so that more accurate inherent strain values can be extracted. This important work has been considered as the future work in order to get deeper understanding of the inherent strain theory. Other reasons such as the material parameter uncertainty in the complex laser-assisted depositing process can also cause some errors since the practical temperature-dependent thermal and mechanical property, which is hard to measure, will influence the real values of the inherent strain in the metal component.

In addition, the influence of employing different number of equivalent layers on the prediction accuracy of the modified method is also concerned. For brevity, only the Ti64 double

cantilever beam is taken as the example. Referring to the identical element mesh for the 60-layer model above, more simulations are performed to simulate different models with 40, 30, 20, 15, 10, 6, and 3 layers. As an extreme case, the entire model only employs one layer to apply the mean inherent strain vector. Respectively, the computational times of the 9 cases above are listed in Table 3.3 using 8 Intel Xeon E5-1660 cores in a desktop computer. It can be seen that the computational time does not increase proportionally to the increasing number of equivalent layers employed in FEA. The reason is that the layer-by-layer simulation is a highly nonlinear process due to the elastoplastic material property. Correspondingly, simulation time increases nonlinearly when more equivalent layers are employed. Nonetheless, compared with the detailed process simulation given the complex laser scanning paths, the layer-by-layer simulation based on the MISM is still computationally much more efficient.

Table 3.3 Computational Time of the Layer-by-Layer Simulation for the Double Cantilever Beam Having Different Number of Equivalent Layers

	Number of equivalent layers								
	1	3	6	10	15	20	30	40	60
Computational time (hour)	0.25	0.39	0.61	0.86	0.98	1.22	1.62	1.85	2.3

The computed maximum total deformation values at the two ends of the double cantilever beam are plotted against the total number of the equivalent layers as shown in Figure 3.5. The continuous curves are obtained by piecewise cubic spline interpolation through the data points. It shows that the maximum total deformation increases first, then decreases and tends to stabilize as

the total layer number increases. Explanation for some characteristics of the curves in Figure 3.5 is provided in the following.

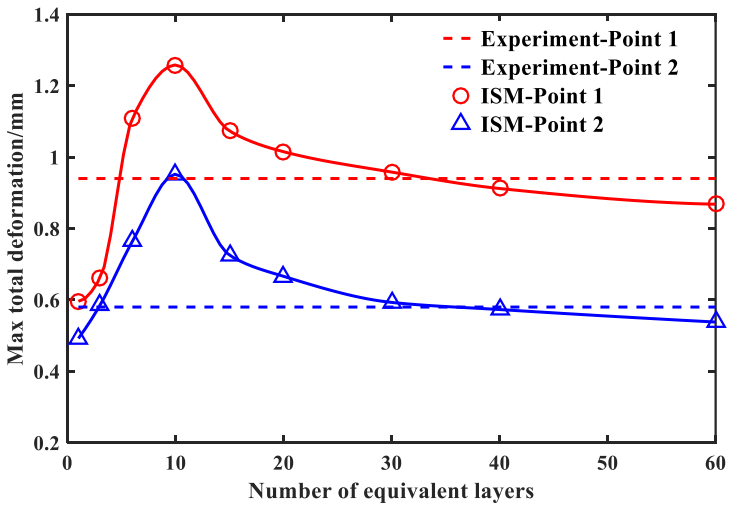

Figure 3.5 Maximum Total Deformation of Point 1 and 2 after Stress Relaxation of the Double Cantilever Beam Containing Varying Number of Equivalent Layers, through the Experiment and ISM

First, as the extreme case, the one-layer modeling case gives the least total deformation compared with other test cases. In the simulation, when the entire model of the double cantilever beam is treated as one layer and the unit temperature increase is applied to the entire model in just one load step, the FEA result shows insignificant residual stress for the elements in the top section. Accordingly, after the support structures are removed to release the residual stress, the two relaxed beams will not bend up so much. This indicates that the one-layer modeling manner will lead to underestimation of the residual distortion and stress. Therefore, it is incorrect to push the layer-by-layer simulation method to the extreme case using only one equivalent layer.

Second, with more equivalent layers (i.e. less layer lumping), there is a steep increase in the total deformation as shown in the beginning of the curve. The reason is that less layer lumping

helps to form large stress in the interface of the support structures and the two overhang beams when the thick layer exactly connected to the support structures is activated. The following activated layers will give a shrinkage relaxation effect to the already deposited layers and help to mitigate the residual stress in that interface. When fewer layers are employed, the relaxation effect on the stress in that specific interface is not so significant compared to those cases when more equivalent layers are used. Thus, in the final equilibrium state, the residual stress is quite large and after it is released, the cantilever beams will bounce up and form large distortion correspondingly

Third, as continuing discussion to the second point, more equivalent layers indicate that the relaxation effect from the upper deposition layers on the stress in that interface will be more significant. Consequently, the residual stress is mitigated to a larger extent. Therefore, a natural trend for the predicted total deformation decreases with more equivalent layers, which is the third feature of the curve in Figure 3.5. However, the stress state in the interface will finally reach a stable equilibrium because the shrinkage of an upper layer too far from that interface has negligible influence on far field stress distribution.

As the fourth characteristic, the predicted total deformation will tend to become stable when enough many equivalent layers (e.g., 40 layers) are employed in the layer-by-layer modeling, as shown in Figure 3.5. This phenomenon indicates that the thin physical layers in the large component cannot be arbitrarily lumped into one super layer. There must be a certain range for the number of lumped layers so as to ensure the prediction accuracy through the layer-by-layer simulation. Therefore, referring to Figure 3.5, the differences between the predicted and experimental results are shown in Figure 3.6 when varying numbers of physical layers are lumped into an equivalent layer. Note that only the 6 cases with at least 10 equivalent layers are taken into consideration as the reference data, because it is reasonable to see the predicted result improves

monotonically when more equivalent layers are employed. Note a larger error is shown in the first case of Figure 3.6 when the number of the lumped physical layers equals 10 compared with the second and third case (15 and 20 physical layers lumped, respectively). The explanation is that the absolute error has been plotted with reference to the experimental measurement in Figure 3.6, while the predicted results are smaller than the experimental results (see Table 3.2) and the error turns negative due to the underestimation in the first case. Therefore, it does not mean the prediction error gets larger when fewer physical layers are lumped into one equivalent layer if the sign of the error is considered.

Figure 3.6 shows the difference between the predicted and experimentally measured maximum total deformation of the double cantilever beam are less than 15% when the number of lumped thin layers is not greater than 30 layers. This finding is very meaningful because it can guide the determination of the smallest number of equivalent layers necessary to obtain acceptable accuracy when the proposed method is applied to other metal parts through the layer-by-layer simulation. In general, if better accuracy is needed, only the number of the equivalent layers needs to be increase correspondingly. However, more equivalent layers will definitely lead to longer computational time of the nonlinear layer-by-layer mechanical analysis. As a result, it is highly necessary to find a compromise between model accuracy and the computational cost with consideration of the requirement in practical applications.

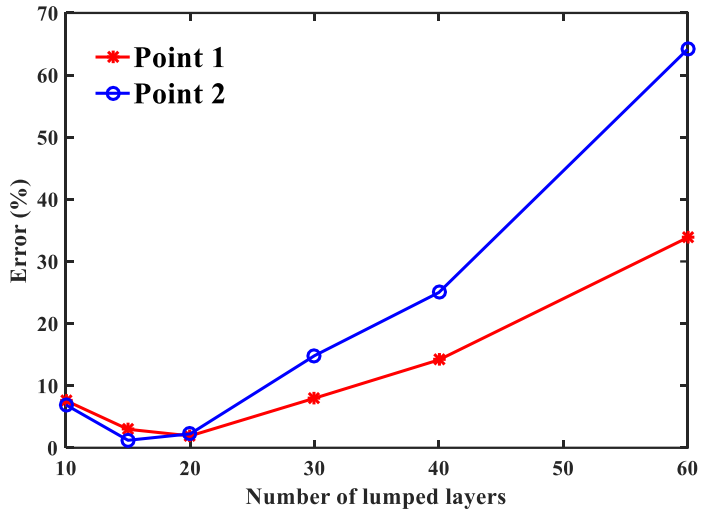

Figure 3.6 The Differences between the Predicted and Experimental Results in Point 1 and 2 Changing with the Number of Lumped Physical Layers in One Equivalent Layer

3.4.2 Canonical Part

Residual deformation of a DMLS-processed canonical component containing curved thin walls shown in Figure 3.7 has been investigated. For the outer section of the component, the length and width are 81.6 mm and the wall thickness is 2.91 mm. For the inner section of the component, the length and width are 29.8 mm, and the thickness of the wall is 1.05 mm. The height of the entire component is 64.35 mm, indicating around 2100 thin layers in the large part. It took around 20 hours to finish the DMLS printing of the component, as shown in Figure 3.8(b). This canonical part is made of Ti64 and all the involved elastoplastic material properties are the same with the first example.

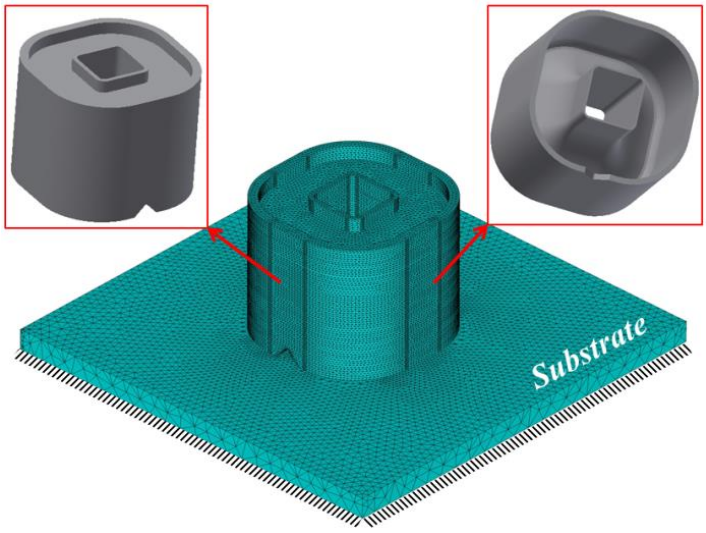

Figure 3.7 A Complex Canonical Part Utilized to Validate the Proposed Method: Geometry Profile and Meshed Model Including the Substrate Using All Tetrahedral Elements

Since the geometry of the canonical part is very complex, a fine mesh has to be used to discretize the model for FEA. To simulate the constraint of the big plate, a substrate with a size of 200×200×10 mm^3 is included in the analysis as shown in Figure 3.7. The meshed model of the canonical part containing 346,420 tetrahedral elements is shown in Figure 3.7 and Figure 3.8(a). For convenience of discussion, the X-axis is defined as the longitudinal direction and Y-axis is defined as the transverse direction, while Z-axis denotes the build direction. The bottom surface of the substrate is fixed in displacement as the mechanical boundary condition. In the solution process, the inherent strain is applied to the canonical part with 60 equivalent layers employed, each having 36 physical layers merged together. Despite the large number of elements, it took around 2.5 hours to finish the entire analysis using the same desktop computer. Clearly, this would be orders of magnitude more efficient than performing a detailed process simulation of the component given the detailed and complex laser scanning strategy as shown in Figure 3.1(a).

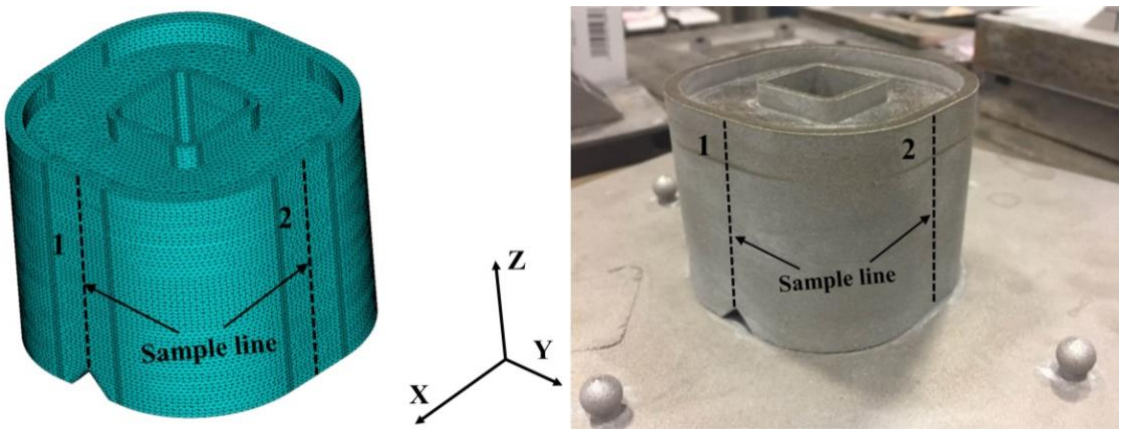

(a) (b)

Figure 3.8 Two Sample Lines in the Meshed Model and the Printed Component by DMLS in Ti64

The simulation result via the layer-by-layer application of uniform inherent strain vector shows that the maximum perpendicular deformation on the outer surface in the longitudinal and transverse direction is 0.68 and 0.69 mm, respectively. Meanwhile, experimental measurement of the residual deformation of the canonical part shows the maximum deformation in the longitudinal and transverse direction is 0.63 and 0.66 mm, respectively. In both the simulation and experiment, the maximum deformations are located at the necking position of the canonical part, which can be clearly observed in Figure 3.8(b). In terms of the comparison between the simulated and experimental results, the percentage error is 7.9% and 4.6% for the maximum longitudinal and transverse deformation. Given that the ISM is 2~3 orders of magnitude lowered in degrees of freedom than detailed process model, these results are considered to be very good. Moreover, the distribution of the residual deformation shares the same features in the two cases. For example, the shrinkage of the outer surface reaches an extreme value similarly nearby the necking position,

where the inner and outer sections of the canonical part begin to connect to each other. This example provides a strong validation of the MISM.

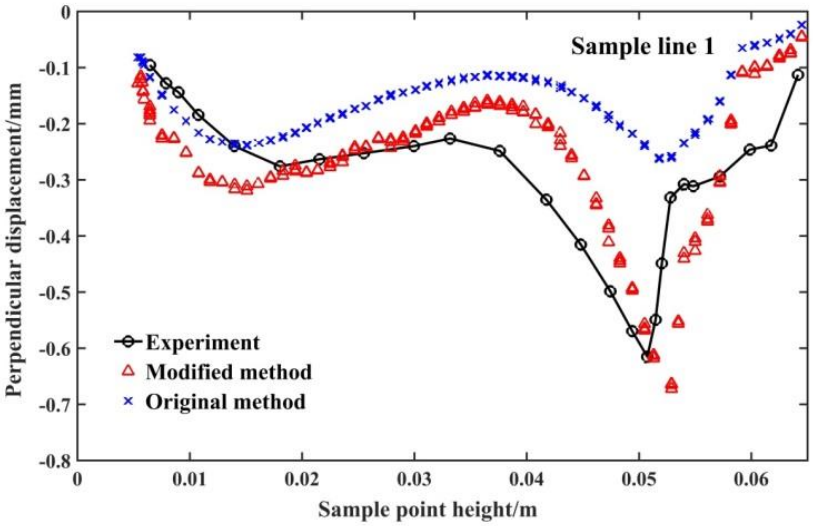

(a)

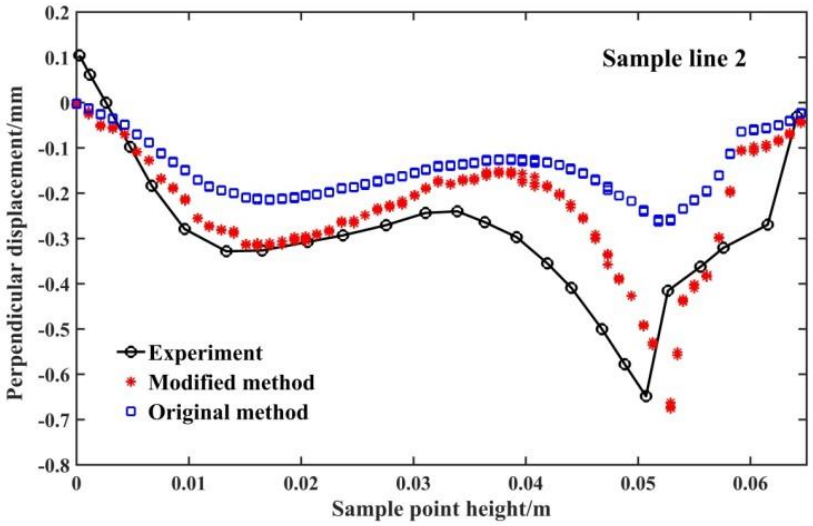

(b)

Figure 3.9 Residual Displacements Perpendicular to the Outer Surface on (a) Sample Line 1 and (b) Sample Line 2 Obtained by the Modified Method, the Original Method and Experimental Measurement

To compare the experimental measurement and prediction from the proposed method, the directional displacements of the nodal points along two sampling paths (black dashed lines) shown in Figures. 3.8(a,b) are extracted. The displacements perpendicular to the outer surface of the concerned points are being studied. Then the values of the displacements are plotted against the sample point height in the vertical direction. Figures. 3.9(a,b) show the general trends of the perpendicular displacements of the nodal points on sample lines #1 and #2 of the canonical part simulated by the proposed method and experimental measurement.

As mentioned above, the sharp valley of the curves corresponds to the necking position of the canonical part. Clearly, good agreement of the curves for the experimental and predicted results by the MISM can be observed in the two figures and accuracy of the proposed method is validated by this example. One reason for the slight mismatch of curves is the slight detachment of the canonical part from the substrate as shown in Figure 3.8(b). As a result, the experimental curves seem to be shifted a little compared with the simulation result. Another reason is the measurement error caused by the operation in the experiment. For example, the laser scanning cannot reach the inside of the canonical part. Consequently, only the outer surface can be used as the reference to align the scanned model with the CAD file, which may cause some errors when the deformation of the model is analyzed.

Next, the influence on the accuracy of the proposed method regarding the large canonical part by the number of equivalent layers is further investigated. The predictions of the maximum perpendicular shrinking deformation along sample line 1 of the canonical part using different number of equivalent layers are shown in Figure 3.9. Compared with the experimental result (red dashed line), the predicted maximum displacement increases in the beginning with a small number of equivalent layers employed. When the number of the employed equivalent layers becomes

larger, the predicted displacement decreases, and gradually becomes stable, indicating simulation convergence is reached. The case using 80 equivalent layers gives an accuracy improvement to 0.66 mm compared to 0.68 mm in the case where 60 equivalent layers are employed. Therefore, to obtain a reasonably accurate prediction (e.g. <10 % error) for large components, sufficiently many equivalent layers such as 60 layers in this example have to be employed despite large computational cost. In that case, the number of lumped physical layers is 35 for one equivalent layer. In Sec. 3.4.1, it shows that the layer-by-layer simulation for the double cantilever beam will give an accuracy of less than 15% error when the number of lumped physical layers is not larger than 30. However, this comparison does not mean better accuracy of applying the proposed method to the canonical part when the same number of lumped physical layers (e.g. 35 layers) is employed for the double cantilever beam. The reason is that the performance of the proposed method cannot be evaluated based on only the match of the globally largest deformation, while the overall deforming patterns of the two large components in Sec. 3.4.1 and 3.4.2 are quite different (see Figure 3.4(b) and 3.8(b)). In fact, many local differences can be seen between the predicted and experimental measured residual deformation of the other sample points in sample line 1 and 2 (see the red and black curves in Figs. 3.9(a,b)), apart from the point having the largest deformation. Therefore, the conclusion cannot be drawn that better accuracy has been obtained by only considering the error of the maximum residual deformation of the canonical part and the double cantilever beam.

In addition, regarding the computational cost, nearly 3 hours are taken to finish the layer-by-layer simulation when 80 equivalent layers are used to improve the prediction accuracy. Thus, it is important to find a compromise between the accuracy and computational expense when any large-scale component with complex geometry needs to be concerned. Nonetheless, compared to

the detailed process simulation, the MISM is still much more efficient since the detailed step-by-step simulation considering detailed laser scanning paths can be extremely slow.

3.5 Conclusions and Discussions

In this chapter, a detailed account has been presented of extracting the inherent strain based on a small-scale thermomechanical simulation of the representative volume for large DMLS Ti64 and Inconel 718 components. The extracted mean inherent strain vector is applied to a part-scale model in a layer-by-layer manner in a series of static mechanical analyses in order to predict the residual deformation. To validate the accuracy of the proposed method for complex metal components, the double cantilever beam (Ti64 and Inconel 718) and the complex canonical part (Ti64) after the DMLS process have been investigated. The predicted residual deformation, especially the globally largest deformation in the large components, matches well (<10 % error) with the results through the experiment measurement, when 60 equivalent layers are employed in the layer-by-layer simulation using the MISM.

Moreover, the effects on the accuracy of the prediction by the number of equivalent layers and the number of lumped physical layers are also investigated. The example shows strong verification of accuracy of less than 15% error of the proposed method in predicting the residual deformation of the large metal components when not greater than 30 thin physical layers are lumped into an equivalent layer in the layer-by-layer simulation. Meanwhile, the computational time of the numerical examples also shows the efficiency of the proposed method. In the future, the MISM can be adapted in a straightforward manner to other AM process such as SLM and EBM. In addition, the same value for the in-plane components does not mean the scan pattern will

not matter in the modified inherent strain approach. In addition, only the rotational laser scanning strategy with a certain angle is investigated. However, if other scan patterns are employed such as the parallel line scanning pattern with specific angle like 0° or 45° degree, the in-plane components parallel and transverse to the laser scanning direction will have some difference in their values. Based on the detailed process simulation results, the laser scanning path will influence the redistribution of the residual strain in the previous layer as the new layer is deposited. As a result, the inherent strain will also be different since it is related to the residual strain accumulation in the AM process.

4.0 Inherent Strain Homogenization for Lattice Support Structures

4.1 Introduction of Support Structures for PBF Process

It is quite challenging to predict residual deformation through thermomechanical simulation when considering realistic laser scanning paths and process parameters. Especially, when lattice support structures such as the thin-walled hollow blocks (Figure 4.1) are used in the DMLS process to assist in building components with overhanging structures [79-82], it becomes more difficult to simulate the PBF process because lattice support structures have lots of fine features which make mesh generation extremely difficult. This very issue makes conventional transient thermomechanical simulation method [27, 55, 83] difficult to implement and computationally intractable, since a moving localized heat source needs to follow exactly the varying laser scanning patterns and process parameters in the solid and support regions in the build. Moreover, the laser scanning strategy has also been found to have some influence on residual stress/strain evolution and accumulation of the metal components produced by PBF [27, 84, 85]. Thus, it is significant to incorporate the effect of the practical specific laser scanning strategy in PBF-fabricated lattice structures when simulating their residual deformation and stress.

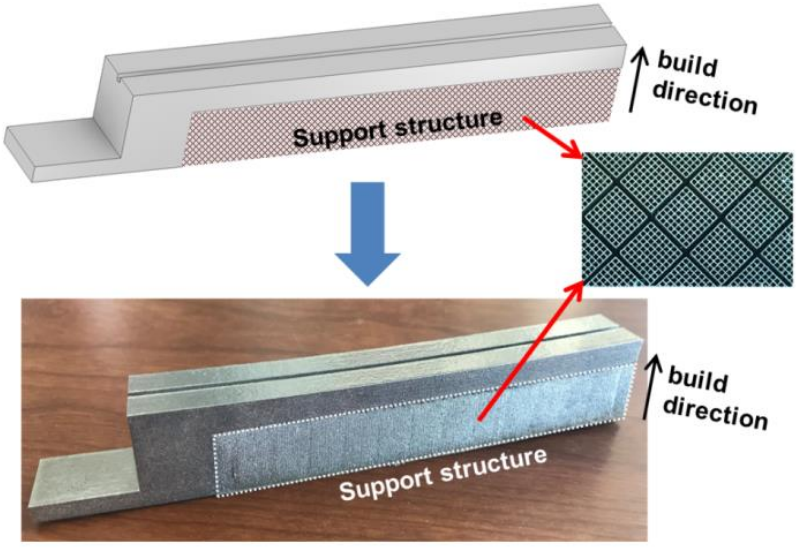

Figure 4.1 Thin-Walled Lattice Support Structures for Overhang Features in the Inconel 718 Component

The current authors have recently published a modified inherent strain model for extracting inherent strains from small-scale thermomechanical process simulation and applying the obtained inherent strains to simulate residual deformation of LENS and PBF components [86, 87]. However, residual deformation of PBF-processed lattice support structures with large number of lattice units have not been investigated by the ISM yet. In this chapter, an ISM based on homogenization is proposed to efficiently and accurately simulate the residual deformation of lattice support structures. Moreover, the homogenized inherent strains and prediction accuracy will be studied for metal builds containing both solid and lattice supports.

4.2 Calculation of Inherent Strains for Support Structures

A specific setup of process parameters is employed to print the thin-walled lattice support structures out of the Inconel 718 powder bed in the EOS M290 printer. The layer thickness in the

build direction is 40μm and other process parameters are prescribed as: laser power 100W, laser scanning velocity 0.90m/s, laser beam diameter 100μm. In order to obtain the accurate inherent strain values, a small-scale thermomechanical simulation is employed and a two-layer model will be modeled as the representative volume [87]. Given the periodicity of the features in the thin-walled lattice support structures (see Figure 4.1), only a small model containing four lines as shown in Figure 4.2(a) is needed to be investigated in the small-scale process simulation. The parallel line scanning strategy is simulated as the basic scanning pattern and only single-track laser beam is employed for printing the support structures as shown in Figure 4.2(b) in the DMLS process. Due to the single-track laser scanning pattern, the wall thickness of the support structures is constant as 0.1 mm, which equals the laser beam diameter in fact. The space size between the center lines of two adjacent parallel walls can be varied to control the volume density of the lattice support structures to satisfy different printing demands. For example, the distance of 1.0mm is adopted to give a volume density of 19% as shown in Figure 4.2. For this case, the size of the selected representative area is $2.0\times2.0mm^2$ including the substrate with a thickness of 0.1 mm in the build direction. In the FEA, very fine mesh is adopted as shown in Figure 4.2(a) in order to apply the small time steps and also to ensure the simulation convergence. The bottom surface of the substrate is fixed as the boundary conditions in the mechanical analysis. If necessary, many helpful details such as the thermal and mechanical governing equations as well as the boundary conditions for conducting the small-scale process modelling can be found in the Refs. [76, 86].

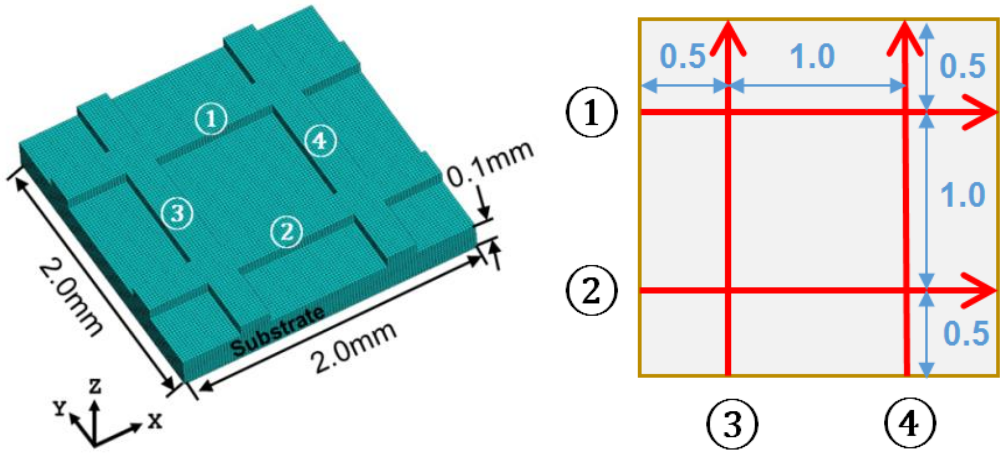

(a) (b)

Figure 4.2 Thin-Walled Support Structure: (a) the Representative Volume for Small-Scale Modeling and (b) the Laser Scanning Strategy and Space Size (in mm)

After the small-scale process modeling is finished, based on the modified inherent strain theory, the inherent strains in the lattice support structures are extracted. Taking Line 1 in Figure 4.2(a) as the example, three normal strain components of the inherent strain vector for that wall are plotted in Figure 4.3 below, while the shearing strain components are neglected. The strain component directions are defined with reference to the coordinates as shown in Figure 4.2(a). Significant difference can be found between the two components in the in-plane direction for the single wall. The reason is the quite different thermal gradients and mechanical constraint conditions parallel and transverse to the laser scanning path [76, 86]. As a result, the mechanical strain accumulation and distribution will be quite different for the direction parallel and transverse to the wall, leading to the significant difference between the two in-plane strain components in the inherent strain vector. The strain component parallel to the wall span-wise direction shows a dominant effect. Moreover, the fluctuations pointed by the arrows in Figure 4.3 correspond to the cross of the two adjacent perpendicular walls. Due to the repeated and perpendicular laser scanning

at those corner areas, the residual strains are redistributed and become closer in the in-plane directions. As a result, the difference between the two in-plane normal strain components in the inherent strain vector for that single wall is narrowed slightly. The same inherent strain distribution is found in the second wall parallel to the first wall. Regarding the remaining two perpendicular walls, the curves for the two in-plane normal strain components will switch compared to those in Figure 4.3. Other features like the fluctuations at the cross areas are similar to Figure 4.3.

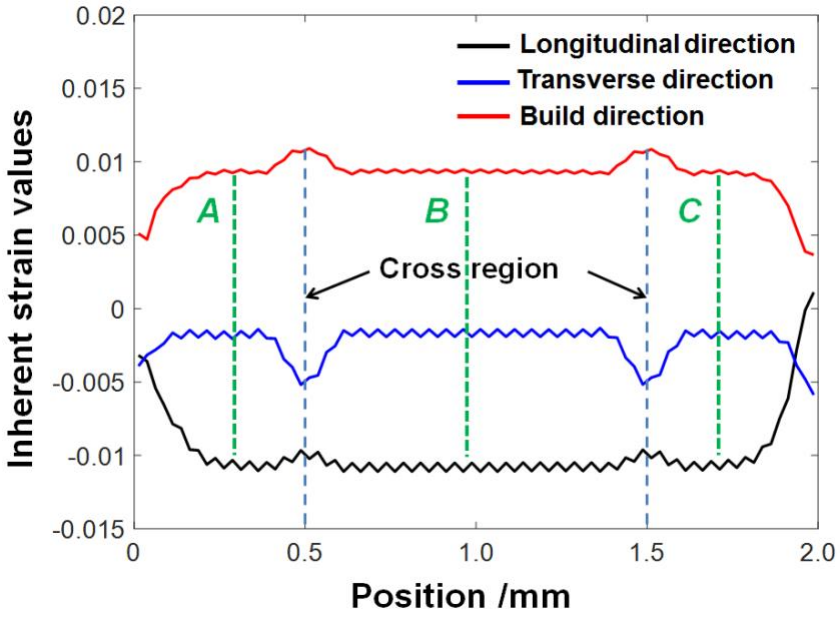

Figure 4.3 Distribution of the Normal Inherent Strains in a Single Wall of the Lattice Support Structures

The average of the inherent strain values in the middle region (the curves between the dashed lines in Figure 4.3) is taken as the mean directional inherent strain vector (DISV) and the magnitude is (-0.010, -0.003, 0.009). This DISV will be defined as the orthotropic CTEs in the DMLS process for the first two walls (deposition line #1 and #2 in Figure 4.2) in the thin-walled support lattice structures. As for the remaining two perpendicular walls (deposition line #3 and #4 in Figure 4.2), according to the small-scale detailed simulation result, the inherent strain plot for

line 3 or 4 is essentially the same with those values for line 1. This is because the thermal history of line 3 and 4 is almost the same with that of line 1 or 2. Moreover, the mechanical boundary condition for line 3 and 4 is the same as line 1 and 2 in the small-scale detailed process simulation. Note that the longitudinal direction is always in the length direction of a wall in the inherent strain plot, although the inherent vectors of all four walls share the same global Cartesian coordinate system in numerical simulation. Therefore, the first two components in the mean DISV are switched to define their CTEs accordingly. On this basis, the asymptotic homogenization method will be employed to evaluate the equivalent mechanical property and CTEs so that the thin-walled support structures can be considered as solid continuum.

Moreover, a larger RVE model is studied in order to investigate how much the inherent strain estimation changes. Assume "a larger RVE" contains more lines in the small-scale model (selected representative volume). For example, a small-scale model where six lines are included is taken into consideration. In contrast to Figure 4.2, there are three lines in each direction on the 2D plane and four square hollow sections are formed. The gap size between two walls is identically 1.0 mm like that shown in Figure 4.2. New simulation results show that the extracted inherent strain values are nearly the same to those values shown in Figure 4.3 as expected. The reason is that the heat source diameter is assumed to be 0.1 mm, which is very small compared with the length of each line in the small-scale model (line length is 2.0 mm in Figure 4.2, for example). In addition, the laser scanning velocity is 0.9 m/s. Therefore, the temperature decreases very quickly after heat source moves away. Given a concerned material point in the line, those materials far away have limited influence to the point of interest. This finding can also be observed in Figure 4.3. See the three sections highlighted by *A* to *C* (green dashed line) in Figure 4.3. The inherent strain values at positions A and C are almost identical to the values at Position B. Except cross

regions and depositions near the edge, the inherent strain values are nearly the same in the lines of the small-scale model. As a conclusion, the inherent strain prediction does not change significantly even when a larger representative volume is selected as a small-scale model. Therefore, it is not necessary to use a larger representative model to extract inherent strain values.

In addition, only the small-scale model with wall gap size of 1.0 mm is studied in the process simulation for extracting inherent strains in the walls. Theoretically, the size of the small-scale model should vary when the distance between walls of the lattice varies. For example, the small-scale model with wall gap size of 0.75 mm and 0.5 mm should be used for volume density of 0.25 and 0.36, respectively. However, the thermal simulation result indicates a wall has no influence on the remaining walls except the cross regions. The heat-induced high temperature affected zone is very small compared with the gap size according to thermal history of the small-scale model at a certain time step. Therefore, it can be assumed that the influence of a wall on the remaining walls is limited when distance between walls of the lattice is large enough. As a result, the extracted inherent strains from small-scale simulation for volume density of 0.19 can be applied to other cases in this dissertation. Nonetheless, it is noted that the above finding may not hold for a case where the wall gap size is close to or smaller than the wall thickness. For example, when the gap size decreases to 0.15 mm for volume density of 0.89, the thermal history of a wall can have some influence on the remaining three walls since they are very close to each other. In this case, the above assumption will cause some change in the extracted inherent strain values. This possible error is ignored in this dissertation for simplicity.

4.3 Asymptotic Homogenization for Lattice Structures

Generally, the lattice structured parts consist of many periodic features also called unit cells or representative volume elements (RVEs). For example, for the thin-walled support structures commonly used in the DMLS process, the obvious periodicity and the RVE is elucidated in Figure 4.4. Clearly, it will be very expensive to employ the FEA to mesh the full-scale thin-walled support structures and perform a nonlinear analysis for the entire model containing a huge number of elements. To balance the computational efficiency and accuracy, the RVE-based asymptotic homogenization theory [88, 89] is employed to compute the equivalent thermal and mechanical properties of the lattice support structures with different volume densities. As a benefit of the homogenized properties, any geometrically complex lattice structures are able to be considered as the regular solid continuum easier to be analyzed.

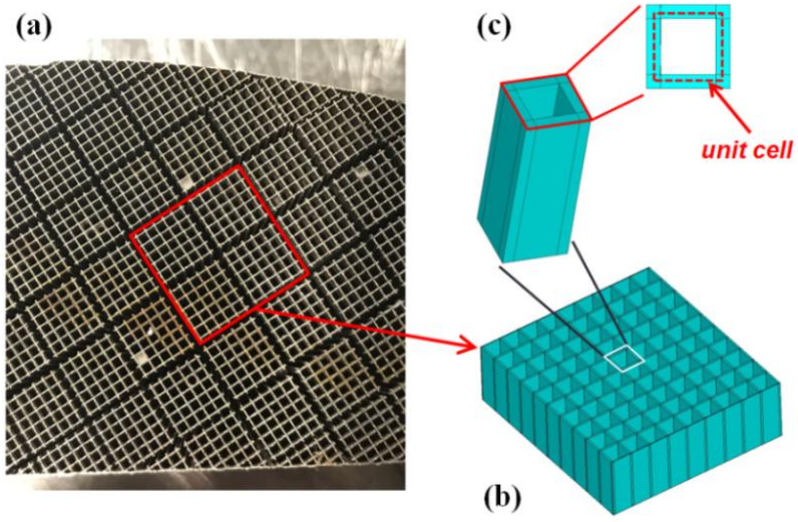

Figure 4.4 Thin-Walled Support Structures in the DMLS Process: (a) Inconel 718 Lattice Depositions; (b) the CAD Model of a Thin-Walled Lattice Block; (c) the Representative Unit Cell (Red Dashed Square)

The asymptotic homogenization method [90] is briefly introduced first. To link the macroscopic structural response with the microscopic mechanical behavior of the material, two sets of coordinate system are established: $\boldsymbol{X} = (X_1, X_2, X_3)$ is defined on the macroscopic domain (Ω_{ma}) of the macro-scale structure, while $\boldsymbol{x} = (x_1, x_2, x_3)$ is defined on the microscopic domain (Ω_{mi}) based on the selected RVE. One dimensionless variable $\epsilon(\boldsymbol{x} = \boldsymbol{X}/\boldsymbol{\epsilon})$ is also defined to describe the characteristic dimension of the RVE. The displacement function can be described by asymptotic expansion against ϵ as a function of the macroscopic parameter $\boldsymbol{X}$ and the microscopic variable $\boldsymbol{x}$ as follows:

$$\boldsymbol{u}^{\epsilon}(\boldsymbol{X}, \boldsymbol{x}) = \boldsymbol{u}(\boldsymbol{X}, \boldsymbol{x}) = \boldsymbol{u}^{(0)}(\boldsymbol{X}, \boldsymbol{x}) + \epsilon \boldsymbol{u}^{(1)}(\boldsymbol{X}, \boldsymbol{x}) + \epsilon^2 \boldsymbol{u}^{(2)}(\boldsymbol{X}, \boldsymbol{x}) + \cdots \tag{4.1}$$

Separation of the macro-scale and micro-scale length scales for homogenization is valid. In fact, $\boldsymbol{u}(\boldsymbol{X})$ can represent a macroscopic field quantity like displacement and strain field. Eq. (4.1) shows a basic assumption that a field quantity like $\boldsymbol{u}(\boldsymbol{X})$ can have asymptotic expansion form based on ϵ in asymptotic homogenization [90, 91]. Specifically in this dissertation, displacement field $\boldsymbol{u}(\boldsymbol{X}, \boldsymbol{x})$ stands for a field quantity like displacement field of macro-scale structure having a relationship with both macro-scale features and micro-scale factors such as geometrical features of lattice unit cells [91]. Potential changes in unit cells (RVEs) can lead to changes in macroscopic field quantity such as the displacement field $\boldsymbol{u}(\boldsymbol{X})$. Therefore, in order to take into account the unit cell features, the displacement field can be parameterized in terms of $\boldsymbol{x}$ and $\boldsymbol{X}$ simultaneously. In Eq. (4.1), the macroscopic variable $\boldsymbol{X}$ belongs to the solid domain Ω_{ϵ} in the macro-scale structure (Ω_{ma}) if there is hollow feature in the entire macroscopic domain (Ω_{ma}). This clarification is necessary because for the thin-walled lattice structures addressed here, there is a lot of hollow gapping space in the blocks. In this scenario, Ω_{ma} represents the entire block, while Ω_{ϵ} indicates

only the domain where there is metal material. If there is no void space in the macroscopic domain (e.g, solid laminate composites), Ω_{ma} and Ω_{ϵ} will be the same.

The mechanical governing equation of the thermal elastic problem defined in the macroscopic domain is written as:

$$\int_{\Omega_{ma}} E_{ijkl}\left(\frac{\partial u_k^{\epsilon}}{\partial X_l} - \alpha_{kl}\Delta T\right)\frac{\partial v_i}{\partial X_j}d\Omega - \int_{\Omega_{ma}} g_i v_i d\Omega - \int_{\Gamma} t_i v_i dS = 0, \forall v \in \Omega_{ma} \quad (4.2)$$

where u_k^{ϵ} stands for a component of displacement field quantity $\boldsymbol{u}^{\epsilon}(\boldsymbol{x})$ in Eq. (4.1); E_{ijkl} is the fourth-order elasticity tensor, α_{kl} is the thermal expansion coefficient tensor. ΔT is the temperature change. v_i denotes an arbitrary testing function for the displacement field, g_i is the body force. Γ is the boundary surface and t_i is the surface force, accordingly.

An important assumption in this chapter is that neither body force term (g_i) nor surface force (t_i, e.g., boundary traction force) is considered in the RVE model for simplicity. By substituting Eq. (4.2) to Eq. (4.1), a series of perturbed equations will be obtained according to the order of the characteristic variable ϵ. One of those perturbed equations involve the $\boldsymbol{u}^{(0)}(\boldsymbol{X})$ and $\boldsymbol{u}^{(1)}(\boldsymbol{X}, \boldsymbol{x})$ is shown as follows:

$$\int_{\Omega_{mi}} E_{ijkl}\left(\frac{\partial u_k^0}{\partial X_l} + \frac{\partial u_k^1}{\partial X_l} - \alpha_{kl}\Delta T\right)\frac{\partial v_i}{\partial X_j}d\Omega = 0, \forall v \in \Omega_{mi} \quad (4.3)$$

In Eq. (4.3), the temperature change ΔT is a known parameter as the thermal loading in the problem. Among the two displacement terms, $\boldsymbol{u}^0(\boldsymbol{X})$ is assumed to be known. The implication of $\boldsymbol{u}^0(\boldsymbol{X})$ is the macroscopic displacement field, which can also be considered as an average displacement field because the effect of perturbation from the unit cell features is averaged [91]. The macroscopic deformation pattern of a structure is easy to know even when it contains many lattice structures because its average overall deformation can always be calculated. For example, for linear elastic case (e.g., line uniaxial loading condition), $\boldsymbol{u}^0(\boldsymbol{X})$ implies the average linear

deformation of the macro-scale structure. In homogenization analysis, the average macroscopic deformation pattern $\boldsymbol{u}^0(\boldsymbol{X})$ is assumed to be known [91], and this knowledge is used to apply a displacement constraint such as unidirectional tensile deformation to RVE-based simulation. $\boldsymbol{u}^{(1)}(\boldsymbol{X}, \boldsymbol{x})$ implies the perturbation term in the accurate overall displacement field given the feature of unit cells in the macroscopic structure. It is not known and will be solved with the assumption that the overall average deformation pattern $\boldsymbol{u}_0(\boldsymbol{X})$ is known. The unknown displacement function $\boldsymbol{u}^1$ can be decomposed and described as the sum of two sources respectively induced by the characteristic mechanical and thermal loading as:

$$\boldsymbol{u}^1 = \boldsymbol{u}^{1m} + \boldsymbol{u}^{1T} \tag{4.4}$$

The two displacement decompositions in Eq. (4.4) will be further computed based on the characteristic displacement solution of the RVE, as shown in the following two equations:

$$u_i^{1m} = -\xi_i^{kl}(\boldsymbol{x}) \frac{\partial u_k^0(\boldsymbol{X})}{\partial X_l} \tag{4.5}$$

$$u_i^{1T} = \eta_i(\boldsymbol{x}) T(\boldsymbol{X}) \tag{4.6}$$

The characteristic displacement $\boldsymbol{\xi}(\boldsymbol{x})$ and $\boldsymbol{\eta}(\boldsymbol{x})$ will be evaluated based on the RVE in the FEA. $\boldsymbol{\xi}(\boldsymbol{x})$ indicates the deformation response under a characteristic mechanical loading like unit strain field, while $\boldsymbol{\eta}(\boldsymbol{x})$ indicates the deformation response under a characteristic thermal loading like a known temperature field $T(\boldsymbol{X})$. Mathematically the solutions to Eq. (4.5) and (4.6) represent the characteristic displacements for the RVE:

$$\int_{\Omega_{mi}} \left(E_{ijkl} - E_{ijmn} \frac{\partial \xi_m^{kl}}{\partial x_n} \right) \frac{\partial v_i}{\partial x_j} d\Omega = 0 \tag{4.7}$$

$$\int_{\Omega_{mi}} \left(E_{ijkl} \alpha_{kl} - E_{ijmn} \frac{\partial \eta_m}{\partial x_n} \right) \frac{\partial v_i}{\partial x_j} d\Omega = 0 \tag{4.8}$$

where E_{ijkl} and E_{ijmn} denote the components of the fourth-order elasticity tensor. α_{kl} denotes the CTE constants of the material. Definition of v_i has been shown above after Eq. (4.2). In the

practical FEA, some specific mechanical and thermal loading conditions such as the unit normal strain loading will be applied to the RVE in order to solve the characteristic displacements and further solve the components in the homogenized constitutive tensors. For example, the specific strain field such as the uniaxial tensile strain will be applied to the RVE in order to evaluate the mechanical response like the deformation and stress distribution. After the characteristic displacement functions are determined, the homogenized elastic modulus, thermal elastic tensor and the CTE tensor of the RVE will be obtained in the following way:

$$C_{ijkl}^{H} = \frac{1}{|\Omega_{mi}|}\int_{\Omega_{mi}}\left(E_{ijkl} - E_{ijmn}\frac{\partial \xi_m^{kl}}{\partial X_n}\right)d\Omega \tag{4.9}$$

$$\lambda_{ij}^{H} = \frac{1}{|\Omega_{mi}|}\int_{\Omega_{mi}}\left(E_{ijkl}\alpha_{kl} - E_{ijmn}\frac{\partial \eta_m}{\partial X_n}\right)d\Omega \tag{4.10}$$

$$\alpha_{kl}^{H} = \left(C_{ijkl}^{H}\right)^{-1}\lambda_{ij}^{H} \tag{4.11}$$

where C_{ijkl}^{H} denotes those components of the homogenized elasticity tensor. λ_{ij}^{H} and α_{kl}^{H} denote respectively the components of the equivalent thermal load and homogenized CTE tensor based on the RVE model. For those interested readers, more complete and detailed mathematic knowledge of asymptotic homogenization method, including more detailed explanation for the above variable symbol, can be found in Ref [90-92].

The important characteristics include the topological configuration and the relative volume density for the lattice structures composed by any designate constituent material. According to Ref. [93], there exists a scaling law mathematically between the mechanical properties and the relative volume density of the lattice structures. Given the specific structural configuration, the relative volume density of the lattice structures is defined as:

$$\rho_v = \frac{V_m}{V_c} \tag{4.12}$$

where V_c and V_m denote the geometrical volume of the cellular structures and the volume of the contained constituent material.

For the fourth-order elasticity tensor in the elastic constitutive law, it will be written in a reduced matrix form in FEA for the three-dimensional problems as follows

$$\boldsymbol{C} = \{C_{ij}\}, i, j = 1,2, \dots, 6 \tag{4.13}$$

When the simplest anisotropic model such as the orthotropic constitutive model is considered, some components in the elasticity matrix ($C_{mn}, m = 1,2,3, n = 4,5,6$, and C_{45}, C_{46}, C_{56} , see Eq. (4.13)) are eliminated to zero. Given the self-symmetry of the elastic tensor and also the geometrical symmetry of the thin-walled lattice support structures in this chapter, the further reduced form of the elastic matrix in Eq. (4.13) can be written as:

$$\boldsymbol{C} = \begin{bmatrix} c_{11} & c_{12} & c_{13} & 0 & 0 & 0 \\ c_{12} & c_{11} & c_{13} & 0 & 0 & 0 \\ c_{13} & c_{13} & c_{33} & 0 & 0 & 0 \\ 0 & 0 & 0 & c_{44} & 0 & 0 \\ 0 & 0 & 0 & 0 & c_{55} & 0 \\ 0 & 0 & 0 & 0 & 0 & c_{66} \end{bmatrix} \tag{4.14}$$

In order to obtain the unknown components in the equivalent elastic tensor for the lattice structures, the standard mechanical analysis will be performed with periodic displacement boundary conditions applied to the unit cell. The specific strain field such as the uniaxial tensile strain will be applied to the unit cell in order to obtain the mechanical response including the deformation and stress distribution [94, 95]. Through the unit cell-based simulation, the equivalent properties of the lattice structures like the elastic modulus and CTEs could be determined in an economic manner.

The numerical implementation of computing the homogenized thermal and mechanical material property as shown in Eqs. (4.9-4.11) will be performed in the commercial software ANSYS v17.2. More details of the solution procedures in the FEA in the commercial software can

be found in the Refs. [94-97]. Especially in Ref. [96], a simple demo code for numerical implementation of asymptotic homogenization was provided in the appendix, even though the demo code was written for a totally solid RVE. The general workflow of RVE-based asymptotic homogenization to obtain equivalent mechanical and thermal properties is very similar for those RVEs with different geometries. Through the homogenization, an equivalent CTE vector will be obtained so that the RVE can be treated as a solid continuum element regardless of considering the rotational laser scanning paths in each thin layer. The way of obtaining the homogenized mechanical property and CTE vector for the thin-walled lattice support structures given different volume densities will be introduced next.

4.4 Homogenized Material Properties

4.4.1 RVE-Based Homogenization

The wall thickness of the thin-walled lattice support structures is kept constant at 0.1 mm as the relative density is varied by increasing the wall-to-wall distance as mentioned above. Table 4.1 gives the volume densities of the various lattice support structures related to the space size. The height of the RVE model is 0.4 mm for all the four cases in Table 4.1, and hence represents the height of ten physical thin layers. The number of lumped thin layers in the RVE is determined for simplicity since in the trials no significant influence is shown in the homogenization results by the height of the RVE model.

Table 4.1 Volume Densities of the Thin-Walled Lattice Support Structures with Changing Space Size

Sample number	Space size /mm	Wall thickness/mm	Volume density
1	1.0	0.1	0.19
2	0.75	0.1	0.25
3	0.5	0.1	0.36
4	0.3	0.1	0.56

Take the first case in Table 4.1 as the example. According to those geometrical size parameters, the RVE model is built as shown in Figure 4.5 and a reasonable mesh is adopted for further analysis. Note the wall thickness of the RVE is 0.05 mm as elucidated in Figure 4.4(c). The DISVs including $\boldsymbol{\varepsilon}_1^* = (-0.010, -0.003, 0.009)$ and $\boldsymbol{\varepsilon}_2^* = (-0.003, -0.010, 0.009)$are assigned to the four walls with respect to their span-wise direction accordingly as shown in Figure 4.5. For the four corners, the two in-plane components in the DISV are averaged and the simple inherent strain vector $\boldsymbol{\varepsilon}_3^* = (-0.0065, -0.0065, 0.009)$ is assigned to those cross regions instead of using the calculated values in Figure 4.3. This choice is consistent with some previous works [75, 76, 86, 87], where the average of DISV was used for the solid material scanned by rotational laser scanning strategy in the simulations to gain efficiency by layer lumping. The benefit is that the homogenized inherent strains can converge to certain values for solid material when volume density reaches its limit of 1.0. However, when volume density of lattice structures increases and gap distance between two walls decreases, the four corners will be major areas occupied by materials. Meanwhile, inter-wall effect becomes an issue because they are too close to each other. This inter-wall effect is not considered in this dissertation for simplicity. Moreover, when gap distance reaches the extreme limit of 0.1 mm, the thin-walled lattice structure would theoretically become bulk solid because the four corners are connected to each other. In this situation, the RVE

model should employ a two-layer block deposited by rotational laser scanning strategy (rotation angle 90°).

For other volume densities, the three DISVs are also employed since the small-scale process modeling for the four cases separately with different space sizes gives similar directional inherent strain distribution as discussed. This phenomenon is reasonable since the walls in the lattice support structures can always be considered as independent lines given the space between despite the four different sizes. For each single wall, the small-scale process modeling shows very similar thermal and mechanical evolution history and no significant mutual influence is found due to the void in the model (see Figure 4.4 and 4.5) except the small cross regions in the four corners.

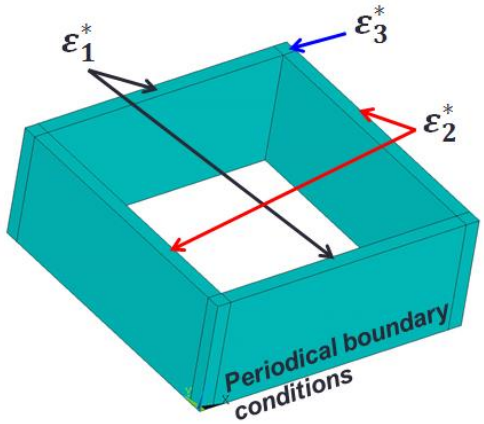

Figure 4.5 The RVE Model and Directional Inherent Strains for Thin-Walled Lattice Support Structures

The asymptotic homogenization is implemented via APDL in ANSYS Mechanical package. The homogenized CTE vector, i.e., the inherent strain vector ($\boldsymbol{\varepsilon}_H^*$), is shown in Table 4.2 corresponding to different volume densities. A decreasing trend is found for the in-plane components of the homogenized inherent strain vector (HISV). Nonetheless, the results show very minor difference between the HISVs for the first three cases. This finding is very helpful to

facilitate the application of the ISM to those scenarios involving lattice structures with low volume density in order to accelerate the numerical simulations through assigning the same homogenized inherent strain values uniformly in the lattice-filled regions.

In addition, the homogenized CTEs show an obvious dependency on the volume density of the thin-walled lattice structures. However, when the in-plane isotropic CTEs like $\boldsymbol{\varepsilon}_3^*$ are assigned to all the elements of the RVE, the homogenization gives the identical homogenized CTEs for all the cases without dependency on the volume density. One more special scenario is that the ideally isotropic CTEs (i.e., $\alpha_{11} = \alpha_{22} = \alpha_{33}$) are employed, for the porous material composed of purely solid and void like the hollow thin-walled lattice support structures in this chapter, the general conclusion is that the effective CTEs are proved to be the same with those values of the solid material for the lattice structures of different volume densities [98]. Therefore, explanation for the dependency on volume densities shown in Table 4.2 is largely attributed to the particular physical features of the DISVs including the magnitude difference of the in-plane strain components and the dominant direction largely related to the laser-track scanning direction as well.

Table 4.2 Homogenized CTEs for the Thin-Walled Lattice Support Structures of Different Volume Densities

Sample number	Volume density	Homogenized CTEs ($\boldsymbol{\varepsilon}_H^*$)
1	0.19	$(-0.0095, -0.0095, 0.009)$
2	0.25	$(-0.0094, -0.0094, 0.009)$
3	0.36	$(-0.0091, -0.0091, 0.009)$
4	0.56	$(-0.0085, -0.0085, 0.009)$

4.4.2 Effective Mechanical Properties

The elastic modulus values of the thin-walled lattice support structures are also obtained through the asymptotic homogenization. The solid tensile bars were fabricated by DMLS using the specific process parameters like laser power of 100 W for the thin-walled lattice support structures. Based on the experimental measurement, the isotropic elastic modulus (165 GPa) is adopted as the basis material property parameter for the solid material of Inconel 718 in the homogenization analysis later.

Meanwhile, some standard tensile bars made of the thin-walled lattice support structures were manufactured by DMLS using Inconel 718 powder. Three different volume densities as 0.19, 0.25 and 0.36 were studied and the wall gap size is set as 1.0, 0.75 and 0.5 mm accordingly for specimen fabrication. Moreover, the specimens were manufactured horizontally and vertically by DMLS in order to figure out directional elastic modulus of the thin-walled structures. These specimens are shown in Figure 4.6 as follows. The total length of these tensile specimens is 102 mm (4 inch) and the detailed shape was designed according to ASTM tensile test standard [99]. For the purpose of avoiding cracking in those thin walls especially walls nearby the edges when the specimens are gripped in the tensile tests, more thin walls were inserted into two ends of the specimens.

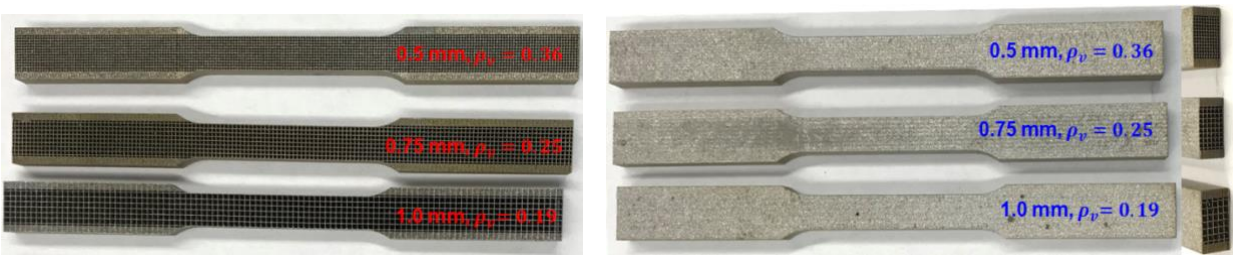

(a) (b)

Figure 4.6 Tensile Specimens of Thin-Walled Lattice Structures Fabricated (a) Horizontally and (b) Vertically by DMLS

The tensile experiments were then performed to determine the effective properties including the directional elastic modulus in order to validate the accuracy of the homogenization. Standard tensile tests were performed on an MTS Landmark test system. Experimental setups of the tensile tests are shown in Figure 4.7. The displacement-control loading rate was 0.5 mm/min and a specific extensometer was used to monitor the deformation/strain history of the specimens in the tensile tests.

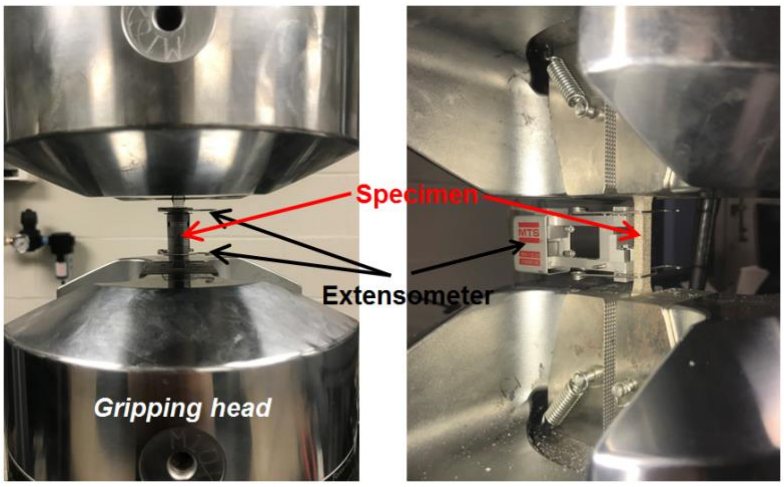

Figure 4.7 Experiment Setup of the Standard Tensile Tests

Multiple specimens for each volume density were tested in the tensile test. The experimental results were described by loading force-displacement curves in Figure 4.8. According to these experimental results, directional mechanical properties including elastic modulus and yield strength of the specimens can be computed. As observed in Figure 4.8, for each single volume density, yield strength of the thin-walled lattice structures is different in the horizontal and vertical build direction. Average of the two directional yield strength values is taken into consideration for the Von Mises yield criterion employed in this dissertation.

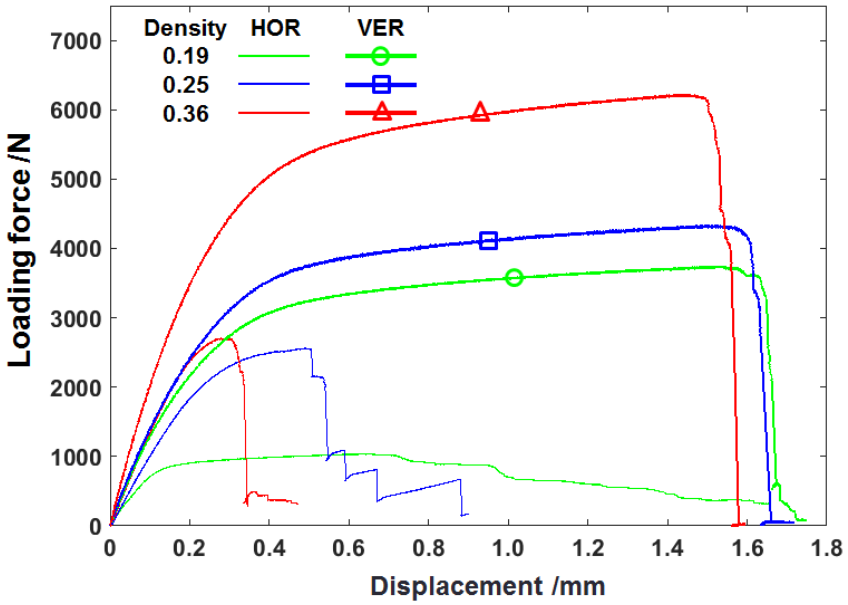

Figure 4.8 Experimental Loading Force-Displacement Curves for Horizontal (HOR) and Vertical Specimens (VER) of Different Volume Densities by the Tensile Tests

The comparison of the homogenized and experimental results is elucidated in Figure 4.9. Good agreements are found in the comparison of the anisotropic elastic modulus obtained by two different ways, which well validates the accuracy of the APDL-based asymptotic homogenization. However, significant anisotropy of the elastic modulus in the in-plane (E_x) and build direction (E_z)

is found as elucidated in Figure 4.9 (red data points). The obtained experimental results can be extended to other volume densities by the least squared error-based polynomial fitting and extrapolation like Ref. [94] as shown by the blue curves in Figure 4.9. Both curves are ensured to start from the origin point to satisfy the physical sense of the void with no materials, even though the zero volume density is not practical for the thin-walled lattice support structures since it indicates the space size would be as large as infinity.

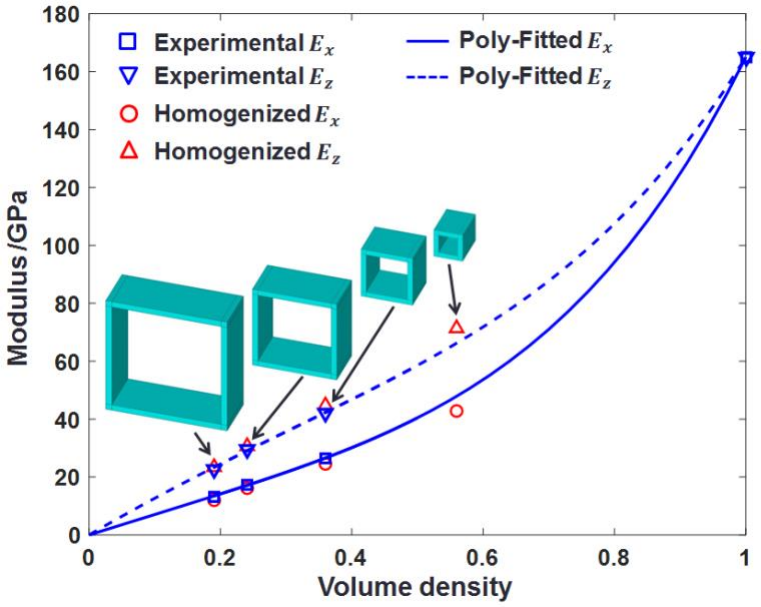

Figure 4.9 Homogenized and Experimentally Measured Elastic Modulus of the Thin-Walled Lattice Support Structures

For better elucidation, the anisotropic elastic modulus obtained by the asymptotic homogenization and the tensile experiments are listed in Table 4.3. Since the homogenized inherent strains are calculated based on the homogenized elastic modulus, the homogenization results will be taken as the material property parameters in the part-scale layer-wise simulation. Moreover, the effective yield strength of the thin-walled lattice support structures of different

volume densities were determined by the tensile tests as shown in Table 4.3. For solid tensile bars with the volume density of 1.0, the measured yield strength is 612 MPa. Note the yield strength for the volume density of 0.56 is determined based on similar polynomial fitting like those curves in Figure 4.9 using the four measured data points including the solid case. These parameters will be used in the layer-by-layer elastoplastic mechanical analysis.

Table 4.3 Yield Strength of the Thin-Walled Lattice Support Structures of Different Volume Densities

Volume density	Homogenized modulus /GPa		Experimental modulus /GPa		Yield strength /MPa
	E_x	E_z	E_x	E_z	
0.19	12.1	23.3	13.1	22.8	45.2
0.25	16.0	30.7	17.5	29.6	60.5
0.36	24.5	44.8	26.5	42.2	101.7
0.56	42.7	71.3	47.9	66.2	210.9

4.5 Experimental Validation

4.5.1 Simple Lattice Structured Beams

The blocks composed by the thin-walled lattice support structures were printed by the DMLS process using the Inconel 718 powder. The dimensional size of these blocks is 75.0×15.0×7.5 mm3. A 3mm-thick solid base was printed under the lattice support structures in order to control the cutting-off position in the post processing as seen in Figure 4.10(a). The

samples of four different volume densities are shown in Figure 4.10(b) in contrast to a nickel coin to elucidate their size.

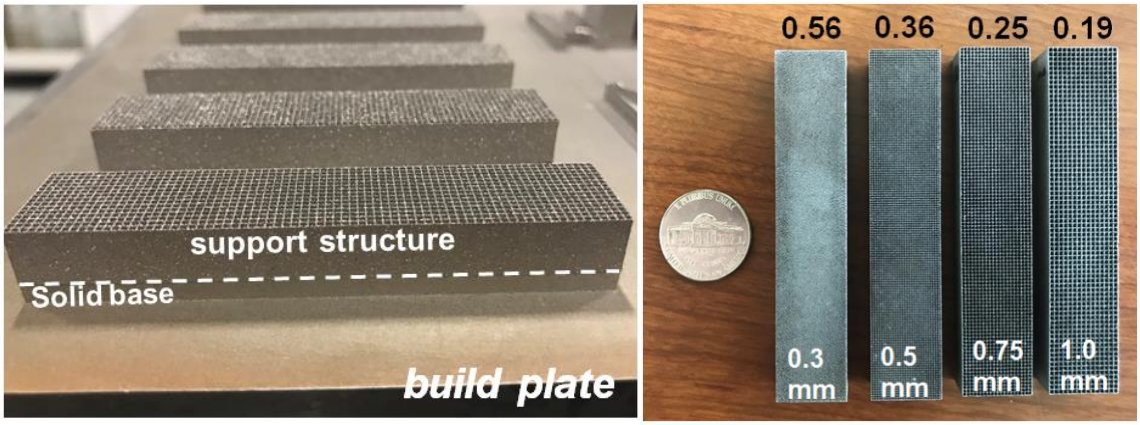

(a) (b)

Figure 4.10 Four Beam Samples by DMLS: (a) As-Built Lattice Support Structures on a Solid Base; (b) Varying Space Sizes for Different Volume Densities

The thin-walled lattice support structures were then cut off along the interface between the lattice structures and the solid base (see Figure 4.10(a)) until 10 mm was left with reference to the end. Due to release of the residual stress, the lattice-structured blocks bend up considerably like a cantilever beam as shown in Figure 4.11. The deformation in the build direction shows an obviously increasing trend with increase of the volume densities of the thin-walled lattice support structures. Compared with the deflections in the build direction, the shrinkages in the other two directions are relatively small, which are not of the concern in this dissertation.

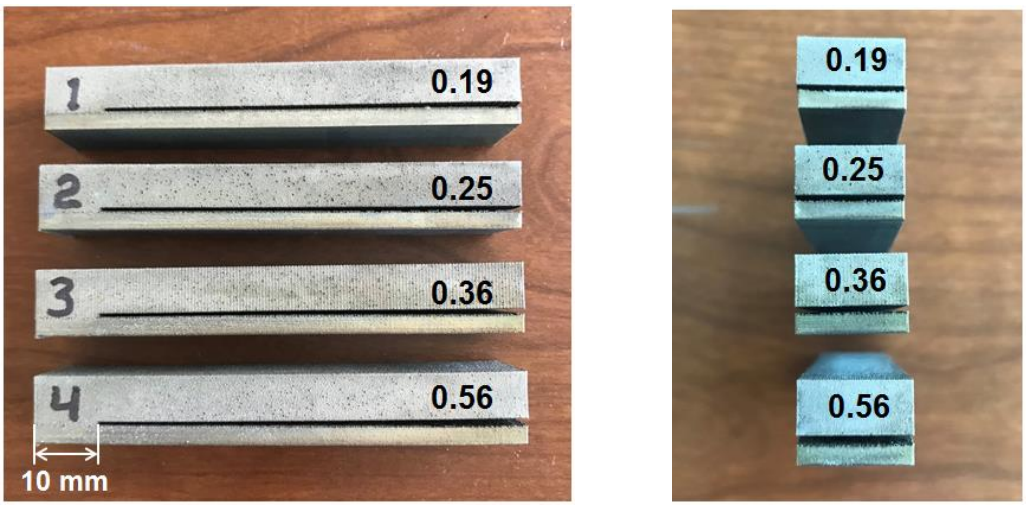

(a) (b)

Figure 4.11 Lattice Structure Beams after Stress Release: (a) the Cutting-off Interface and (b) Vertical Deformation

Meanwhile, the residual deformation of the lattice structure blocks will be computed by the inherent strain-based simulation for validation. To give a thorough investigation, the full-scale block with all the detailed lattice features is also simulated. However, only the case of the lowest volume density 0.19 with 1.0mm space size is studied because the computational cost is not affordable for the remaining cases with denser lattice structures. The full-scale thin-walled lattice support structures containing 1125 (75 in length ×15 in width) hollow tubes on the solid base are created and meshed finely in ANSYS as shown in Figure 4.12. The 10.5mm-high model is divided into 30 equivalent layers, five layers of which are for the 3mm-thick solid base. The bottom surface of the solid base is fixed as the mechanical boundary condition. The 8-node brick element is adopted and the total number of the elements in the full-scale modeling is 550160. Consequently, the computational cost is very expensive for this problem.

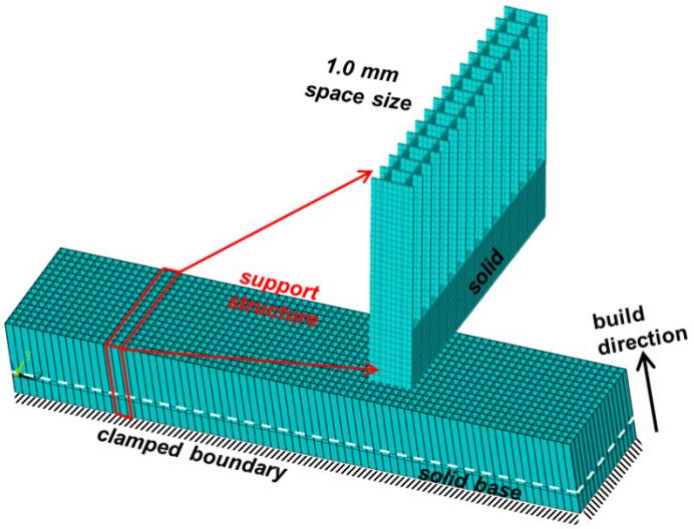

Figure 4.12 The Full-Scale Model of the Lattice Structure Block with 1.0 mm Space Size

For the solid base, it was deposited using the regular process parameters including laser power 285W and rotational laser scanning strategy for solid volumes. As a result, different inherent strain vector should be assigned to the elements in the solid base. According to the Ref. [86], the mean inherent strain vector of $\boldsymbol{\varepsilon}_s^* = (-0.015,\ -0.015,\ 0.02)$ is adopted for the five layers in the solid base of the full-scale model. For the thin-walled lattice support structures, three different inherent strain vectors as mentioned (see Figure 4.5) are assigned to those thin walls and cross regions, respectively. After the layer-by-layer modeling, the elements in the intersection of the lattice support structure and the solid base are killed to simulate the stress release. Due to the huge number of elements and many load steps in the nonlinear analysis, it took around 9.5 hours on the lab computer (Intel Xeon CPU E5, 8-core, RAM 32.0 GB) to finish the full-scale simulation even though the layer-wise ISM has been employed. It is expected that much longer time will be consumed if the lattice structures of larger volume densities are simulated in full details. For the lattice structures of larger volume densities, there are much more unit cells in the blocks. For example, there are 2,000 (100 in length × 20 in width, wall gap size 0.75 mm) and 4,500 (150 in

length × 30 in width, wall gap size 0.5 mm) for volume density of 0.25 and 0.36, respectively. Given the wall thickness is uniformly 0.1 mm, there would be tens of millions of elements in the full-scale finite element models in these cases. For these cases, it will be very difficult to generate the mesh and will take days/weeks to perform a layer-by-layer full-scale simulation in ANSYS. This explains why full-scale modeling results are not provided for larger volume density cases including 0.25, 0.36 and 0.56.

Meanwhile, the equivalent model employing the homogenized mechanical properties and inherent strains is established. As a benefit, the homogenized model is represented by a simple block of the same size compared with the full-scale modeling. The total element number in the homogenized model is 109375. There are also 30 equivalent layers defined in the homogenized model and different inherent strain vectors will be used for the five layers in the solid base and the remaining layers in the lattice support structures. Element killing is also adopted to simulate the stress release phenomenon after the layer-adding process is simulated. Moreover, the same mechanical boundary condition is used in this simulation. It took nearly one hour to finish the simulation based on the homogenized model on the same lab computer. The significantly reduced computing time suggests the great advantage of employing the homogenized mechanical property and inherent strains in the simulation for complex lattice structures.

In order to further accelerate the simulation, only half block needs to be considered given the symmetry in the problem as depicted in Figure 4.13. The half-size model is adopted in the simulation for the remaining cases for different volume densities. Moreover, a coarser element mesh is used for half-size block model, while there are still five layers in the solid base. The total element number decreases to 45000 for the half-size block representing the homogenized model. Generally, it took nearly half an hour to finish the layer-by-layer depositing and stress release

simulation based on the half-size homogenized model. Especially for the case of volume density 0.19, the symmetry-constrained simulation results on the half-size model with those detailed thin-walled lattice structure features is compared to the full-size detailed modeling as mentioned above. Only insignificant difference is found between the residual deformations obtained through the two ways. In addition, for the detailed half-size modeling, it took nearly four hours to finish the layer-by-layer deposition adding-on and stress release simulation.

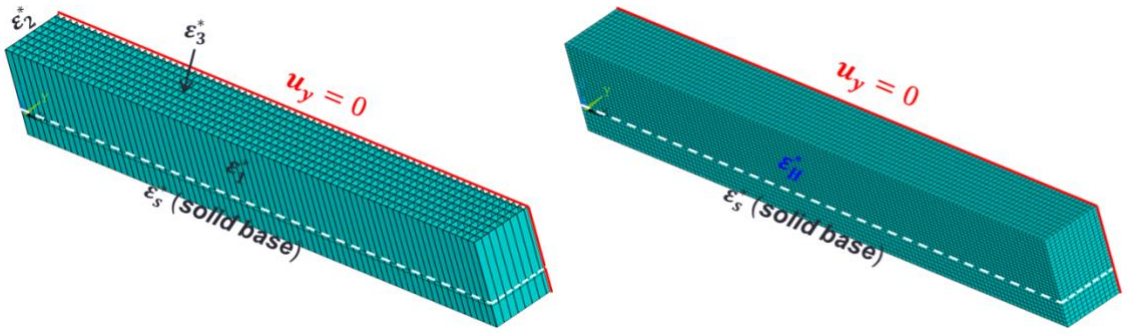

(a) (b)

Figure 4.13 The Half-Size Model under Symmetrical Constraint Condition: (a) Detailed Thin-Walled Lattice Structures; (b) Homogenized Solid Model

In addition, the residual deformations of those printed solid-lattice bonded blocks were measured by the Laser Faro Arm scanning device after the stress release in the experiment. Taking the case of volume density 0.19 as the example, the normal residual deformations especially in the build direction by the detailed half-scale modeling, the homogenization-based half-size modeling and the experimental measurement are shown in Figure 4.14 for full comparison. The maximum residual deformation in the build direction is 0.46, 0.45 and 0.43 mm in the Figs. 4.14(a)~(c), respectively, giving a very close comparison. The simulation result based on the homogenized inherent strains and material properties is proved to have good agreement with the half-scale

modeling and the experimentally measured residual deformation of the lattice structured cantilever beam.

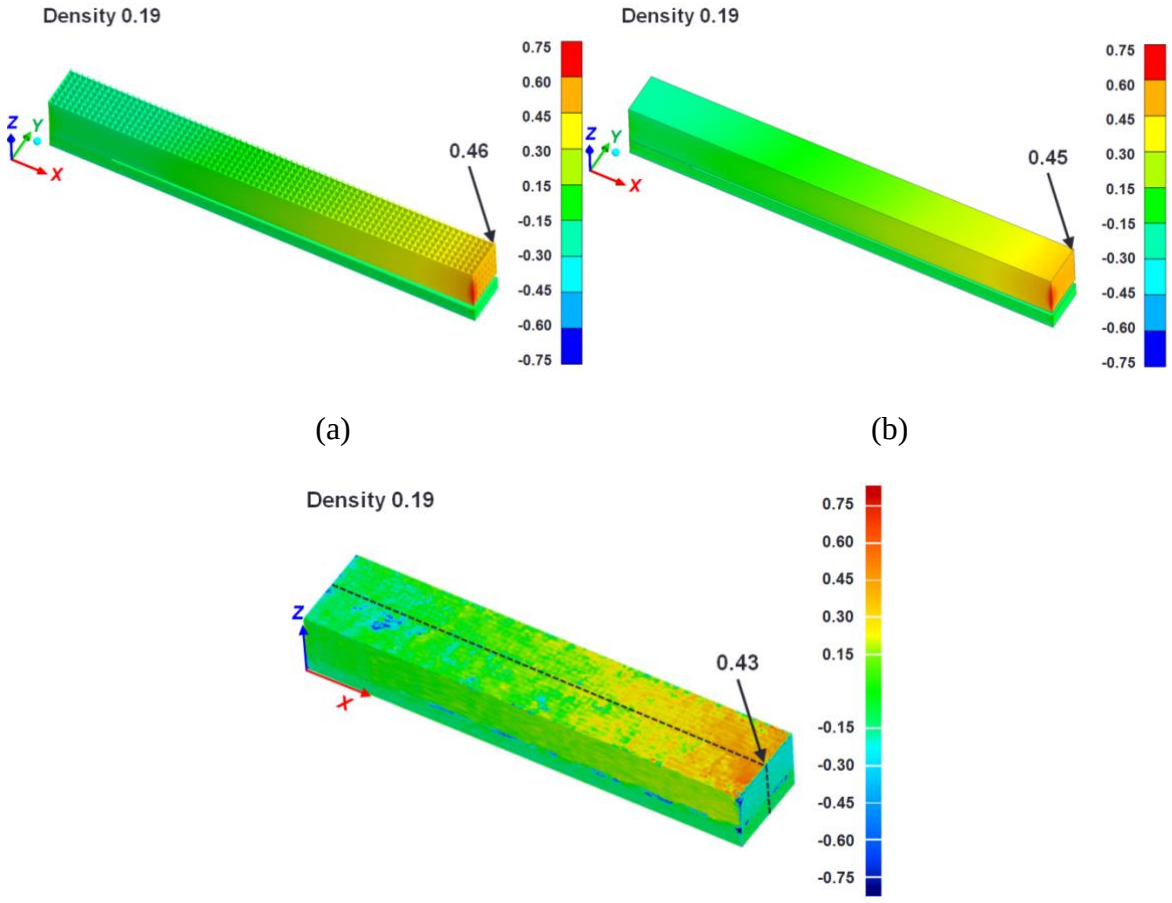

Figure 4.14 Vertical Residual Deformation (Unit: mm) for Volume Density of 0.19 through (a) Half-Size Detailed Modeling, (b) Half-Size Homogenization-Based Modeling and (c) Experimental Measurement

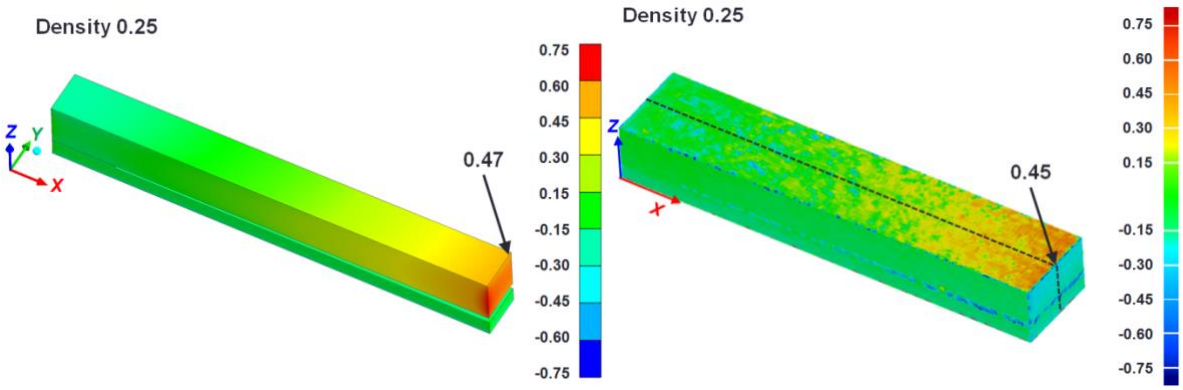

(a)

(d)

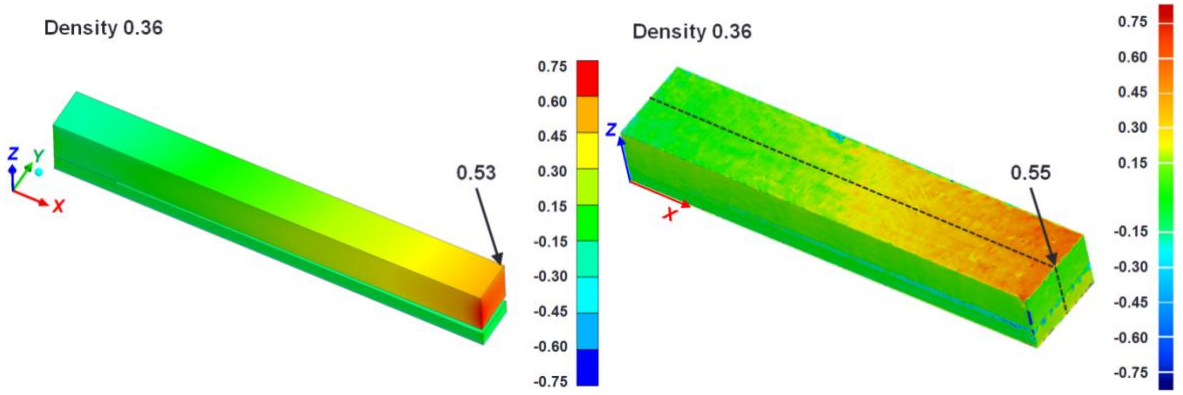

(b)

(e)

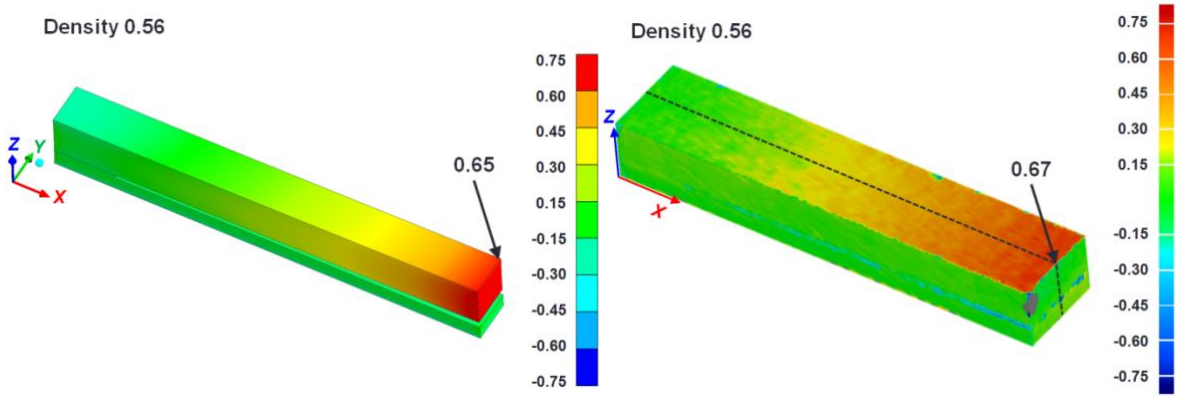

(c)

(f)

Figure 4.15 The Vertical Residual Deformation for Different Volume Densities Obtained by (a)~(c) the Half-Size Homogenization-Based Modeling and (d)~(f) the Experimental Measurement

Regarding the remaining cases for other three volume densities, since the layer-by-layer simulation of the full-scale model like Figure 4.12 is not practical due to the inevitable overlong computational time, only the half-size block modeling based on the homogenized material properties and inherent strains is performed. The computational time for the remaining cases is also nearly half an hour since the total number of the elements and load steps keep the same for all the case. The computed residual deformations are compared to the experimental results as elucidated in Figure 4.15. The maximum deflection on the center plane of the beam (see dashed line in Figs. 4.15(d)~(f)) in the build direction is annotated by those black arrows. Good agreement of both the distribution pattern and magnitude of the residual deformation by the simulation and the experimental measurement can be found in all the three cases. Moreover, the vertical residual deformation of the lattice structured cantilever beam shows an obviously increasing trend when denser lattice structures are used as observed in Figure 4.11 by eyes.

In addition, the vertical deflections along the center line of the top surface of the cantilever beam in all the above cases are illustrated in Figure 4.16. Due to the considerable space between those thin walls especially for the cases with lower volume density like 0.19 (1.0mm space size) and 0.25 (0.75mm space size), the experimental measurement is subjected to some errors and as a result the curves show some fluctuations as seen in Figure 4.16. For larger volume densities, the top surface of the lattice structured beam becomes smoother and flatter. Therefore, the experimental curves turn smoother accordingly. Nonetheless, regardless of the fluctuations in the curves, the simulation and experimental curves show a good match between, convincingly validating the excellent accuracy of the homogenization-based material properties and inherent strains for simulating the residual deformations of the thin-walled lattice support structures in the PBF process. Moreover, excellent efficiency of the homogenized inherent strain-based simulation

has been verified by the largely reduced computational time from typically nearly four hours to half an hour using the symmetrically constrained half-size modeling, leading to an eightfold speedup for the case of volume density 0.19. For those thin-walled lattice support structures of larger volume densities, the speedup will be more considerable since the simulation with all the lattice features considered will consume much longer time while the half-size modeling utilizing the homogenized inherent strains and material properties always consumes nearly half an hour regardless of different volume densities. Therefore, it will be very promising to see wide applications to the practical manufacturing scenarios regarding the PBF process.

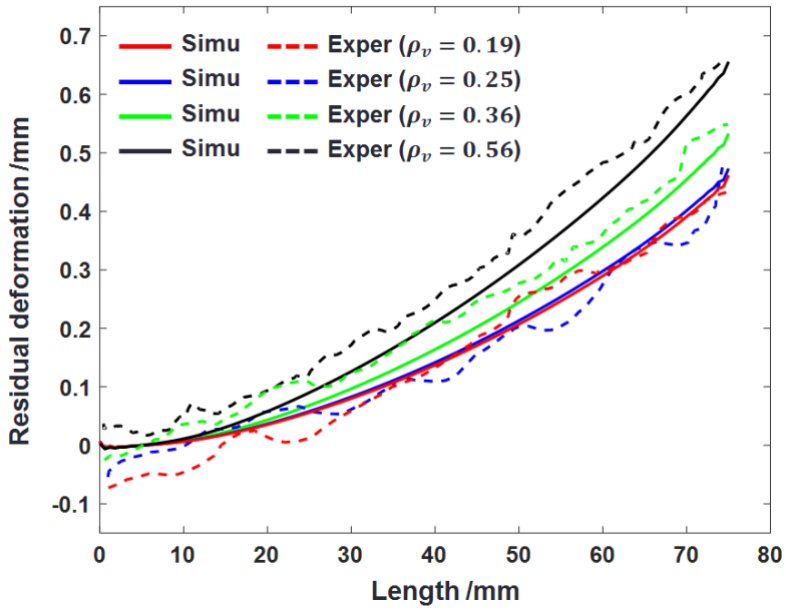

Figure 4.16 Vertical Residual Deformation along the Top Center Line of the Beam with Different Volume Densities

The simulation results are slightly higher than the experimental values on average for low volume density case of 0.19 and 0.25 as shown in Figure 4.16. The likely reason is the large hollow space induces some errors as discussed before, and leads to lower measurement values for low

volume density thin-walled samples. However, simulation results are lower than the experimental values on average for the volume density case of 0.36 and 0.56. A few reasons may result in this issue. One reason is that DISV extracted from low volume density case of 0.19 has been directly used for homogenization simulation of all the involved volume density cases. No inter-wall effect is considered for larger volume density cases where gap size between two walls becomes very small. A larger DISV may exist for those cases due to inter-wall effect. Another reason is that the wall thickness will have more uncertainty due to closer joint corners when gap size decreases in higher volume density cases. This may result in stronger material property in practice than the homogenized model. Consequently, the simulation results should be lower than the experimental values of residual deformation.

In general, the magnitude of mismatch in the four cases is within 0.1 mm as seen in Figure 4.16. In order to give a more rigorous measure, the overall error between dashed and solid lines is computed. Since 8 different curves are involved without analytical description equations in Figure 4.16, a convenient way is to adopt piecewise integration with reference to a shared lower bound line. According to Figure 4.16, a horizontal line for residual deformation of -0.1 mm is selected as referential lower bound for all the 8 curves. Certainly, a different referential lower bound can be employed since it does not change absolute error integral between any two curves. The area integral values of the 8 curves are computed and listed in Figure 4.17. The average error between dashed and solid lines for low volume density cases like 0.19 and 0.25 is very small and an overall larger prediction result is shown. In contrast, overall underestimation is shown between dashed and solid lines for larger volume density case like 0.36 and 0.56, though the error magnitude is still small (less than 10%). A likely reason is that inter-wall effect on extracted inherent strains was not considered when homogenization was implemented for large volume density cases using

DISV extracted from the case of low density value of 0.19. Future work is needed to provide a thorough study on inter-wall effect in thin-walled lattice structures. Regarding the mismatch between experimental curves (dashed lines with different colors), the area integral values for low volume density cases like 0.19 and 0.25 are very close overall. The same finding is also valid for comparison between simulation prediction results for these two cases. However, for large volume density cases like 0.36 and 0.56, obviously area integral values are closer between experimental and simulation prediction results in either case. Meanwhile, significant discrepancy has been proved when those two experimental results (see dashed lines for volume density case of 0.36 and 0.56) are compared from the view of error integrals as shown in Figure 4.17 below.

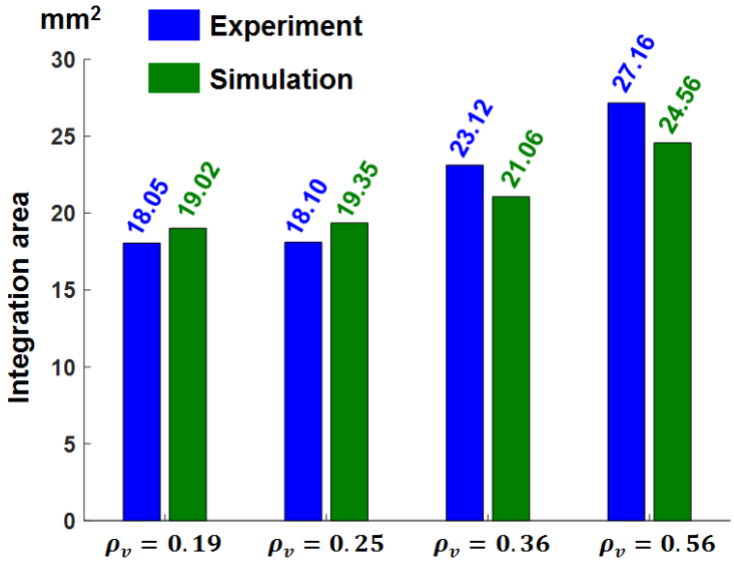

Figure 4.17 Area Integral Values for Residual Deformation Curves for Overall Error Evaluation

4.5.2 Application to a Complex PBF Bracket

In order to show scalability of the proposed method, a complex bracket with overhang features is studied in this section. Thin-walled support structures are needed to support the

overhangs in PBF processing of the bracket. An image of the complex part together with the support structures is shown in Figure 4.18. Some geometrical dimensions are also annotated in the figure. The volume density of the thin-walled support structures is set as 0.36 which corresponds to a wall gap size of 0.5 mm.

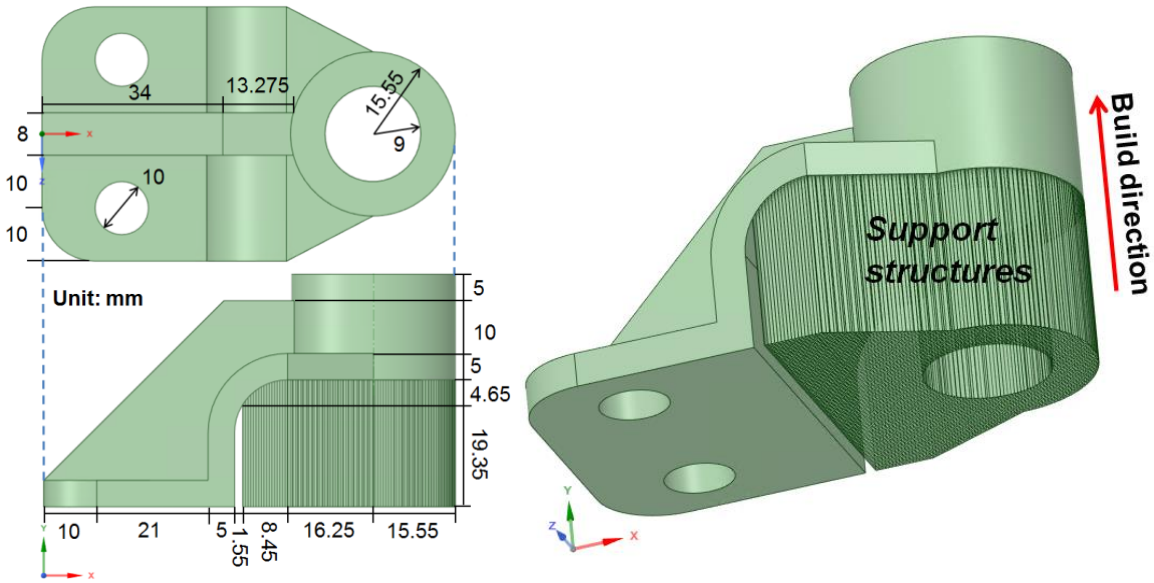

(a) (b)

Figure 4.18 Geometrical Dimensions of a Complex Bracket with Thin-Walled Support Structures

Similar to Section 4.5.1, the entire component is modeled through a layer-by-layer simulation where different inherent strain values are employed for the bulk solid regions and homogenized thin-walled support structures, respectively. As a preliminary study, for the component with a height of 44 mm, the model is sliced into 25 layers and accordingly, a large layer activation thickness of 1.76 mm is employed. In other words, nearly 44 thin layers are lumped into an equivalent layer in the layered simulation. Though an overestimation of the residual deformation is expected according to the previous work [87], the computational cost for modeling

such a complex geometry can be saved significantly. In addition, tetrahedron elements are adopted to mesh the component as shown in Figure 4.19. Especially for the interface between the solid and thin-walled support structures, element mesh is refined for better accuracy in the simulation for layer-wise material addition and post cutting process. Moreover, a small substrate with a thickness of 2.0 mm is attached to the bottom of the bracket and its bottom surface is fixed in displacement as the boundary condition for the entire inherent strain model. This setup has been proved to be helpful in avoiding stress overestimation at bottom surface of the bracket and having the simulation converged smoothly when a tetrahedron element mesh is employed. In total, there are 67,618 elements in the model and the number of degrees of freedom is 310,920. Regarding the computational time, it takes about 4.0 hours using 12 cores of an Intel work station (Xeon Gold 6136 CPU, 3.00 GHz) to finish the layer-wise printing and the post cutting process.

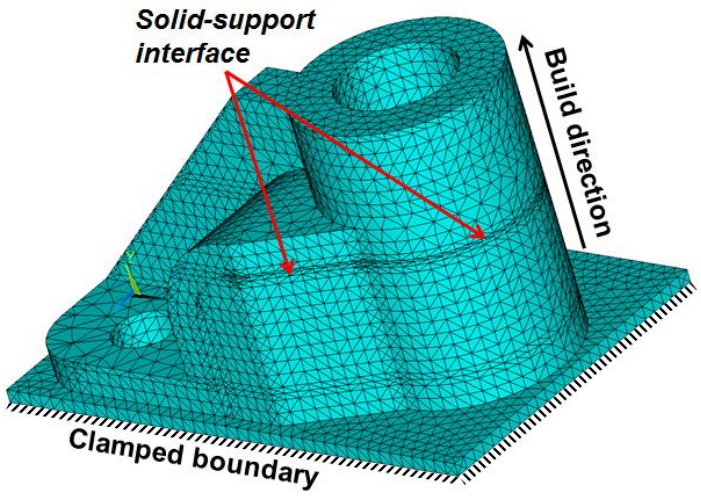

Figure 4.19 Tetrahedron Element Mesh for the Complex Component with Homogenized Support Structures

Meanwhile, the bracket was fabricated by PBF with the support structures added. The metal build is shown in Figure 4.20 before and after the cutting process. Apparent vertical deformation

can be found by observing the gap along the solid-support interface. Similar to those cantilever beams Section 4.5.1, the residual deformation of the PBF bracket was measured using the Faro Arm laser scanning device. Post-processing for the obtained cloud data including the build reconstruction and alignment to the CAD file is identical to the procedure presented in the previous example.

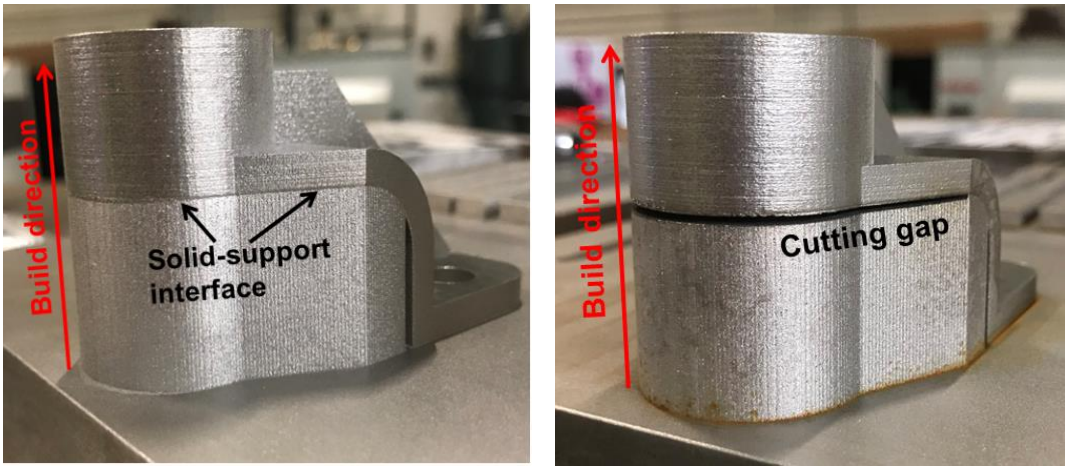

(a) (b)

Figure 4.20 L-BPF Component with Thin-Walled Support Structures before and after Cutting Process

A comparison of the simulation and experimental results is shown in Figure 4.21. The vertical deformation obtained by the inherent strain-based simulation is plotted in Figure 4.21(a). Regarding the experimental measurement, only surficial normal deformation can be computed in Geomagics software. As seen in Figure 4.21(b), the color of red/yellow indicates expansion deformation along the surface normal, while color of blue indicates shrinkage of the surface. The irregularly large negative or positive displacements denoted by dark blue and red color along the edges and sharp corners are not real. This irregular issue has been explained in Section 4.5.1. Especially in this example, it is very difficult to capture the sharp edges and corners of the bracket

precisely by the Faro Arm laser scanner. One reason is the metal surfaces for PBF solid materials are very shiny and it results in multiple reflections of the detecting laser rays especially when the sharp corners are scanned. As a result, the sharp edges and corners cannot be reconstructed with high resolution based on the point clouds. Regardless of the plotting style, general pattern of the residual deformation distribution is very similar in the figures. The maximum vertical deformation occurs at right edge of the cylinder and the measured value is 0.40 mm. In contrast, the predicted value through the simulation is 0.47 mm, indicating an overestimation of 17.5%.

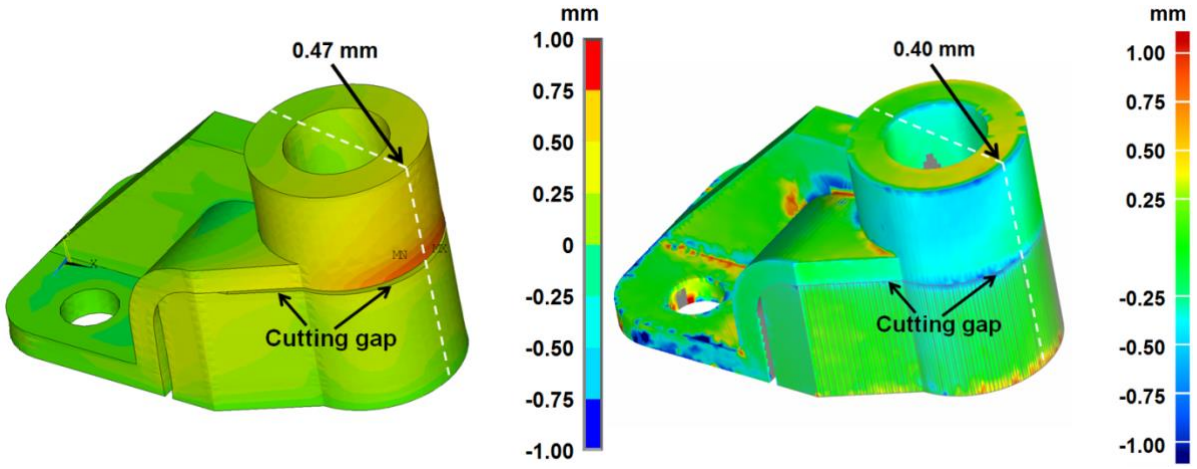

(a) (b)

Figure 4.21 Residual Deformation Comparison of the Bracket with Support Structures after Cutting Process through (a) Simulation (Vertical Displacement) and (b) Experimental Measurement (Surface Normal Deformation)

As already discussed in Chapter 3.0 [86], the simulation prediction can be improved by employing smaller layer activation thickness. In addition, the mesh quality can be further improved by using a smaller layer thickness. However, smaller layer thickness will result in longer computational time as a tradeoff. Nonetheless, this example is able to verify the scalability of the

proposed method when it is applied to more complex AM builds with support structures. As a future work, automatic mesh generation based on voxel elements will be investigated in order to further accelerate the layer-wise simulation while ensuring good accuracy. The potential for a wide application to more PBF scenarios can be foreseen.

In this chapter, a critical degradation of model accuracy involves underestimation of residual stress level in the homogenized model compared with full-scale model. The reason lies in the fact that the homogenized model does not consider local features such as sharp corners in the thin-walled support structures since the entire block has been considered as continuum without holes. To some extent, the homogenized model imposes numerical average to the residual stress between unit cells in the thin-walled lattice structures. However, in full-scale modeling, all the sharp corners in the thin-walled lattice structures are considered and higher stress level due to stress concentration issue has been found. As a result, the full-scale modeling results show higher residual stress level in some local position, such as the interface between thin-walled lattice structures and solid base. Nonetheless, the underestimation of local residual stress does not affect the conclusion that the homogenized model can give an accurate prediction of residual deformation after the stress relaxation simulation, which in turn verifies that the average stress level can be simulated with accuracy in the homogenized model.

Another important discussion is provided following the above issue. The lattice support was designed to be completely continuous in the validation experiment in order to make the numerical simulation simpler without the need to simulate the gaps as shown in Figure 4.4. However, if the gaps between each unit are adopted in the PBF process to print solid onto lattice support structures, when cutting-off process is performed along the solid-support interface, constraint of the lattice structures to the top solid part will be weaker due to missing material in

the gaps as compared to the case where full lattice support without such gaps. The top solid part will be easier to deform and as a result, the predicted residual deformation could be larger. This study on potential effect of support continuousness on the simulation results is beyond the scope of this dissertation. It will be further investigated in the future work by printing solid cantilever beam onto thin-walled support structures in validation experiments.

4.6 Conclusions and Discussions

The major obstacle to efficient prediction of the residual deformation of those AM builds with lattice support structures in the PBF process lies in the complexity of the topological features and physical printing manners of the lattice structures. In this chapter, the thin-walled lattice support structures commonly employed in the DMLS process are investigated. The wall-wise directional inherent strains are extracted based on the small-scale process modeling of a representative volume taken from the macroscopic lattice support structures given the periodicity according to the MISM. Then the asymptotic homogenization method is employed to compute the effective mechanical properties like the elastic modulus and inherent strains of an RVE for the thin-walled lattice support structures. The homogenized elastic modulus values for lattice support structures with of different volume densities have been validated by tensile experimental results. Significant anisotropy has been found in the directional elastic modulus in both the homogenization and the tensile experiment.

Based on the homogenized inherent strains and mechanical properties, the block beams composed by the thin-walled lattice support structures are able to be considered as solid continuum models in the layer-by-layer simulation. The residual deformations via the homogenization-based

simulation especially in the build direction as the dominant deformation pattern are compared to the experimental measurements. For all the studied lattice structured beams of different volume densities, good agreement can be found in the comparison between the simulation and the experiment. Therefore, the accuracy of the proposed simulation using the homogenized inherent strains and elastic properties to compute the residual deformation of the thin-walled lattice support structures in the PBF process has been well validated. Moreover, the proposed homogenization-based simulation methodology shows great efficiency according to the reduced computational time compared with the detailed modeling considering all the lattice structure features. This advantage is very significant for enabling prudential applications of the proposed method to the prediction for the residual deformation of those metal builds with lattice support structures in the PBF process. The scalability of the proposed method is further shown by extensive application to a complex component with support structures added. It is highly promising to have a wide application to more scenarios containing complex components with lattice support structures based on the method.

When the lattice structures with other topological configurations are concerned, the most important thing is to find the DISV specifically adapted to the structural topology and laser process parameters adopted for those PBF-fabricated lattice structures, before the proposed homogenization-based simulation method can be applied. Some manufacturing-related factors like rotational laser scanning strategies are not studied in this chapter. However, more influential factors will be investigated in the near future including the lattice structural topological configurations, the different laser scanning strategies and scanning velocity for fabrication of those lattice structures.

5.0 Enhanced Layer Lumping Method (ELLM) for Accelerating Simulation

5.1 Current State of Simulation for PBF

The PBF process has been the most popular metal additive manufacturing (AM) technology [4, 100, 101] thus far. Metal components are deposited out of the powder bed by repeated laser-assisted micro-welding process in a bottom-up manner. Due to the intensive heating and rapid cooling phenomenon, significant residual stress and deformation can be observed in the cooled metal components. Large residual stress is harmful to the PBF process because cracks and delamination can be caused in the metal builds [102]. Moreover, large residual deformation can result in failure of the build process since the layer-wise powder spreading process would be stopped due to collision with the deformed depositions. Therefore, it is very meaningful to investigate the residual stress and deformation of large metal components before practical fabrication by PBF.

Thermomechanical simulation employing a moving point [27, 36, 55, 69, 84, 103] or line heat source model [86, 104] has been a conventional manner to simulate the material depositing process and residual stress and deformation in the final component. However, since the moving heat source model has to follow the complex laser scanning paths, the detailed simulation would be quite time-consuming. As a result, it is impractical to apply the detailed thermomechanical simulation to large metal components. In order to make the part-scale simulation feasible, ISM [37, 39, 40] has been considered so that the mechanical analysis can be performed in a lay-by-layer manner without considering the moving heat source model [75, 105-107]. Especially, the MISM (MISM) successfully adapted the ISM to the metal AM process including DED [76] and

PBF [86, 87]. Compared with conventional thermomechanical simulation, the computational cost has been greatly reduced and part-scale simulation of residual deformation and stress became feasible based on inherent strains in a layer-wise analysis frame [75, 87, 105].

However, usually a large component fabricated by PBF can contain thousands of thin layers in the vertical build direction. Even though the detailed laser-assisted depositing paths are not considered, it is impractical to simulate all the thin layers in the sequential inherent strain-based mechanical analysis because the computational cost would be too expensive and thus is impractical. Naturally, lumping many thin layers into an equivalent layer in the numerical simulation becomes a practical choice. Many commercial codes [106, 108] such as Ansys Additive [109, 110], Simufact [81, 86, 100] and Autodesk Netfabb [111-113] have adopted layer lumping in their simulation for residual stress and deformation of metal depositions. However, there is very little specific study on its accuracy. Especially related to the lumping effects, one recent work [114] studied the classical lumping approach in the thermomechanical simulation through merging physical metal welds. Their efficient simulations showed acceptable accuracy of temperature and residual deformation prediction despite underestimation for the residual stress in the Inconel 625 builds produced by DED. However, no thorough layer lumping-related studies have been found for the L-PBF process so far.

Moreover, even though equivalent layers are employed in the inherent strain-based simulations, thickness of the equivalent layer has been shown to exert significant influence on the prediction accuracy of residual stress and deformation [87]. Even though a reasonable thickness of the equivalent layers is adopted by merging a couple of thin layers, the total number of effective layers for a large metal component can still be quite large. Due to the expensive computational cost, the inherent strain-based simulation is prohibited from application as a high-fidelity solver to

some design-oriented work, such as topology optimization of support structures that can actively mitigate residual stress and deformation in large metal components fabricated by PBF [81].Thus far, there has been no study on how to lump more layers reasonably in order to accelerate the layer-by-layer simulation to the largest extent, while ensuring good prediction accuracy for residual stress and deformation of the large components fabricated by PBF. This explains the motivation of the enhanced layer lumping method (ELLM) proposed in this chapter.

5.2 Enhanced Layer Lumping Method (ELLM)

5.2.1 Layer Activation Thickness (LAT) Effect

While the inherent strains are loaded in a layer-wise manner as introduced in Chapter 3.0, the layer activation thickness (LAT) is found to play an important role on prediction accuracy in the layer-by-layer simulation. Though the inherent strains are extracted from the detailed thermomechanical simulation taking the real layer thickness (RLT) into consideration [86, 87], if the RLT is employed as the LAT, the numbers of elements and load steps in FEA for a large-scale model would be too large to process in any commercial software such as ANSYS. For example, the RLT for Inconel 718 (IN718) is 0.04 mm in the PBF process. A complex canonical part in the previous work [86, 87] and also Chapter 3.0 has a height of 64.5 mm, indicating there are more than 1,600 thin layers in the build direction. In that case, it is very difficult to generate the mesh using an RLT of 0.04 mm in the FEA. Moreover, it is impractical to implement the highly nonlinear analysis using more than 1,600 load steps because it would be too time-consuming. Nonetheless, in this section using RLT is considered as the extreme case to study the LAT effect in the layer-

by-layer simulation. The goal is to find a reasonable minimum LAT that reduces computational cost and meanwhile ensures simulation accuracy for residual stress and deformation. Based on the found LAT, how to lump more layers to further accelerate the layer-wise simulation will be figured out later.

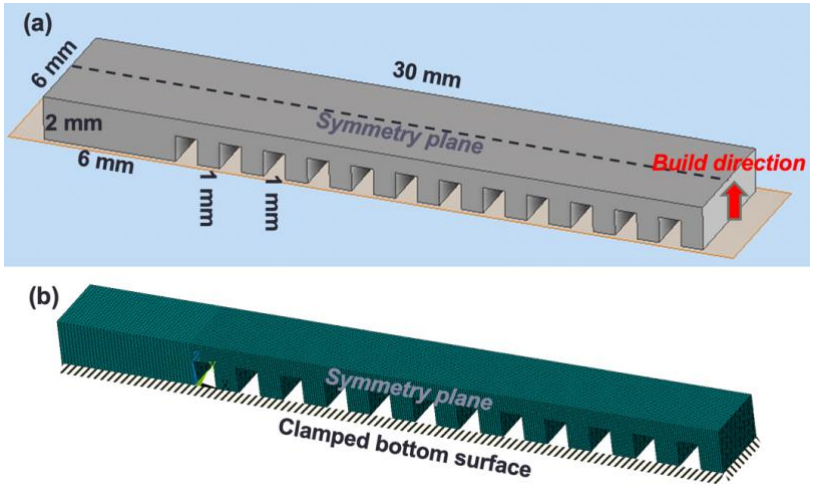

Figure 5.1 The Short Cantilever Beam as The Benchmark Case: (a) Geometrical Profile; (b) Finite Element Mesh and Boundary Condition for the Half Model

A 2 mm tall cantilever beam is adopted as the benchmark example containing 50 thin layers to investigate the LAT effect. Geometrical profile of the short cantilever beam is shown in Figure 5.1. The length and width the cantilever beam is 30 mm and 6 mm, respectively. Thickness of the teeth-like support structures is 1 mm and there are 12 bars beneath the reaching-out beam. The height of those support structures is 1.2 mm (30 thin layers), indicating the height of the reaching-out beam is 0.8 mm (20 thin layers). In addition, gap size between two adjacent support bars is 1 mm. Length of the solid base on the left of the cantilever beam is 6 mm. Regarding the finite element mesh, the RLT of 0.04 mm is used to define the 8-node solid element thickness in the vertical build direction. Given the symmetry conditions in this problem, only half of the beam (half

width = 3 mm) needs to be simulated. Consequently, there are 312,000 elements and 343,821 nodes in the half model.

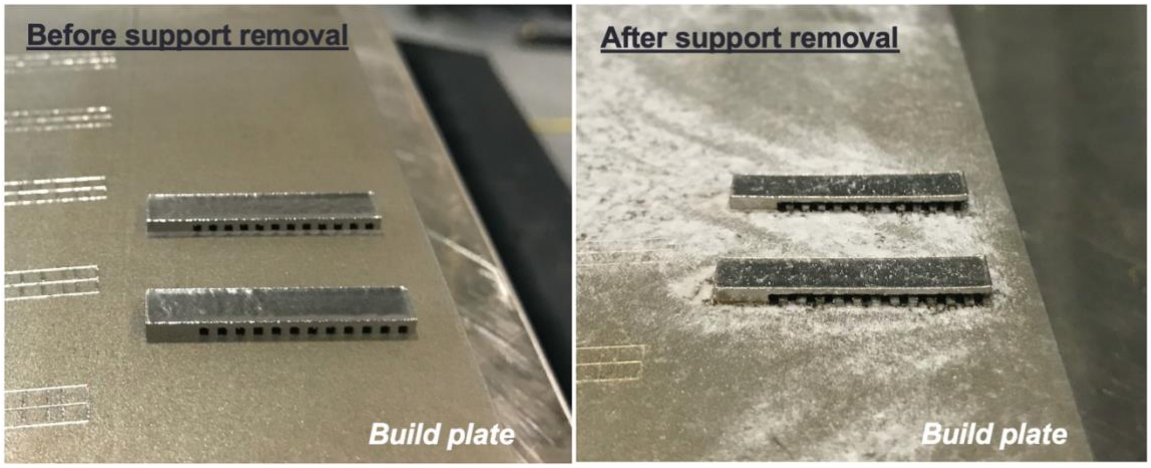

(a) (b)

Figure 5.2 The PBF Short Cantilever Beam Samples (a) before and (b) after Support Removal by W-EDM

Two cantilever beam samples were deposited by PBF (EOS M290 printer) using the IN718 powder as shown in Figure 5.2(a). Alternating laser scanning strategy with a rotational angle of 67° was adopted. The laser power is 285 W and laser scanning velocity is 0.96 m/s. Under this manufacturing condition, the corresponding ISV is $(-0.015, -0.015, 0.015)$ as already validated in the previous work [87, 115]. This ISV is applied to the half model as the CTEs in the material property parameters. For the elastoplastic material model, the elastic modulus and yield stress for IN718 is 185 GPa and 750 MPa [115]. Moreover, the wire-based electric discharge machining (W-EDM) was used to cut off the teeth-like support structures in the post-processing. Vertical bending becomes the dominant residual deformation after the support removal as shown in Figure 5.2(b). The residual deformation of the cantilever beam was measured using a 3D laser scanning device in the experiment.

Regarding the ISV-based simulation, 50 load steps (50S) are employed to implement the layer-wise simulation in the extreme case considering the 50 thin layers (50L). That is, the adopted LAT is exactly the RLT of 0.04 mm. In addition to the extreme case, different LAT values such as 0.2 and 0.4 mm are tested. Accordingly, there are 10 and 5 load steps in the two cases denoted by 50L10S and 50L5S due to the identical 50-layer mesh, respectively. In other words, 5 or 10 thin layers are activated in a single load step in the above two cases. However, as mentioned above, it is very expensive to employ RLT to generate a fine mesh for a large component containing thousands of thin layers. Therefore, two more cases are investigated where the element thickness is changed to 0.2 and 0.4 mm, respectively. In this way, the number of elements in the half model is greatly reduced to 10,944 and 5,472 and for the 10L10S and 5L5S case, respectively. For all the involved cases, it takes 24 additional load steps to simulate the support removal process through killing those elements attached to the solid-support interface. All the involved simulations were performed on a desktop computer equipped with two 8-core Intel Core i5 processors. The computational time for each case is listed in Table 5.1 as follows.

Table 5.1 Computational Time of Five Simulation Cases for Short Cantilever Beam

Case #	Layered depositing simulation/min	Support removal simulation/min	Total time/min
50L50S	210	50	260
50L10S	20	40	60
50L5S	10	35	45
10L10S	3	3	6
5L5S	1	2	3

Finally, the vertical residual deformation results obtained by the five simulation cases are compared with the experimental results. The vertical displacements along center line of the top surface are extracted and plotted against the sampling positions in Figure 5.3.

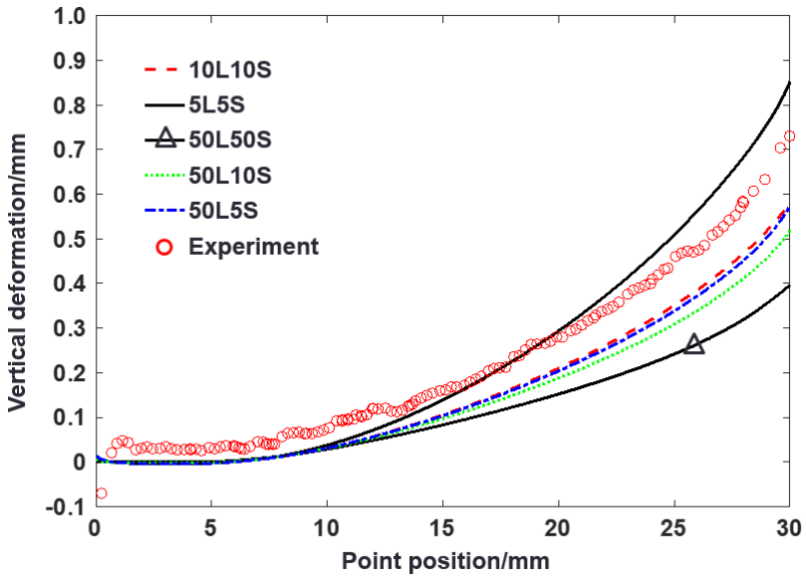

Figure 5.3 Vertical Residual Deformation along Center Line of the Top Surface of the Short Cantilever Beam Obtained by Five Simulation Cases and Experiment

In summary, the extreme case (50L50S) gives significant underestimation among all the five cases. The likely reason is that the extracted ISV inherently averages the influence of the layer-wise rotational laser scanning patterns. It is not reasonable to directly apply the ISV to a single thin layer without consideration of the variance of layer-wise laser scanning paths. Another reason is that the ISV is uniformly applied to each layer and all the materials in a layer are activated simultaneously. This manner may overestimate the stress relaxation effect on the lower layers due to thermal shrinkage of many upper layers. As a result, overall residual stress is underestimated due to the stress relaxation effect [87]. When the residual stress is released through removal of the supports, the residual deformation becomes underestimated, accordingly. Lumping thin layers can

help mitigate the over-relaxation effect on the lower depositions by those upper layers as in the 50L10S and 50L5S case. This explains why reduced prediction error is seen in these two cases according to Figure 5.3.

Regarding the 10L10S and 5L5S case, 5 or 10 thin layers are merged into one equivalent layer containing one element in the build direction. This manner numerically makes the materials within those thin layers stiffer because the equivalent layer has much fewer degrees of freedom due to reduced node numbers. Moreover, by using the equivalent layers, the number of upper layers for any concerned layer becomes much smaller. As a result, the stress relaxation effect on the lower layers is weakened, resulting in a little overestimation of the residual stress. When the residual stress is released, vertical bending deformation becomes significantly larger compared with the extreme case (50L50S). As shown in Figure 5.3, results of case 10L10S and 5L5S have a better agreement with the experimental results. Especially, the 5L5S case using the LAT of 0.4 mm shows slight overestimation of the residual deformation. Comparison of the overall residual deformation obtained by the 5L5S case and the experiment is shown in Figure 5.4. Good agreement in the residual deformation distribution can be seen in the figure. Moreover, it is better to adopt such a LAT in the layer-wise simulation because an overestimation in the residual stress and deformation can provide a conservative evaluation for a large metal component. In fact, this finding is consistent with the previous finding. A similar LAT from 0.4 to 0.6 mm was mentioned in the previous work as a direct numerical study on feasible equivalent layer thickness [87] though no systematic derivation like this section was involved in that work. Thus far, based on the knowledge on the ISV-based layer-by-layer simulation, the LAT is defined in the range of 0.4 to 0.6 mm in the following sections. In other words, 10 to 15 thin layers of IN718 can be merged into an equivalent layer to accelerate the layer-by-layer simulation as a reasonable criterion.

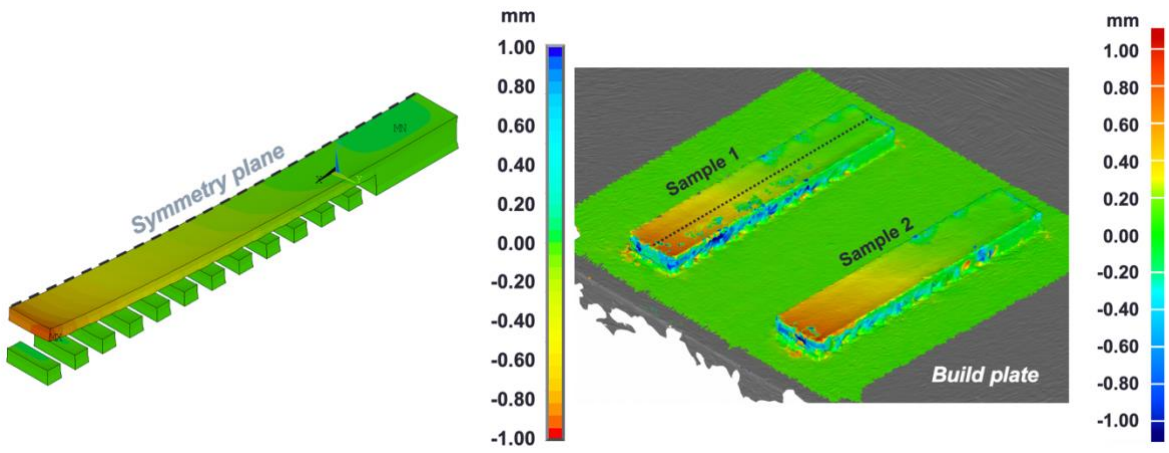

(a) (b)

Figure 5.4 Residual Deformation of the 2 mm Tall Cantilever Beam Obtained by the (a) 5L5S Case and (b) Experiment

However, even though 10 to 15 thin layers are lumped into one equivalent layer, the layer-wise simulation would still be computationally expensive for large components. It is infeasible to adopt a larger LAT simply by lumping some equivalent layers, because the simulation error will become very large according to the numerical trials. Therefore, next step is to investigate the enhanced layer lumping method (ELLM) to lump as many equivalent layers as possible in a single load step in order to further accelerate the layer-wise simulation.

Thus far, a basic point is that residual deformation, especially that after the residual stress is released due to cutting-off of the support structures in the metal cantilever beam builds, is largely determined by the residual stress level in the as-built depositions. However, if a couple of equivalent layers are lumped into a super layer and are activated in one load step, multiple layers in the deposition deform simultaneously. Generally, this reduces stress but accumulates shrinkage deformation. The inherent stress relaxation effect cannot be observed in this situation. Residual

stress level in the lower layers tend to be higher than the benchmark case without lumping layers. As a result, after the residual stress in the lower layers is relaxed, the residual deformation especially in the vertical build direction becomes overestimated significantly.

5.2.2 Meso-Scale Modeling of Residual Stress Evolution

Since only lumping the equivalent layers could result in large computation error of the residual stress and deformation, in this section, residual stress evolution in the layered deposition process is studied in order to figure out what to do in combination with lumping layers to address that issue. A meso-scale block model is established as shown in Figure 5.5. The size of the meso-scale model is 10×10×5 mm^3 and it contains 125 thin layers deposited by the PBF process. The LAT for an equivalent mesh layer is set as 0.5 mm in order to reduce the total number of elements. In the meso-scale simulation, the model is meshed into 10 equivalent layers. Accordingly, there are 20×20×10 elements in the model.

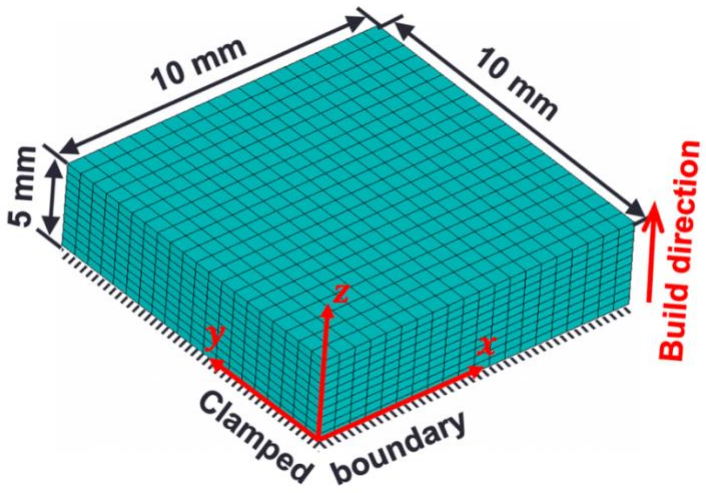

Figure 5.5 The Meso-Scale 10-Layer Block Model with Fixed Bottom Surface

The same ISV and elasto-plastic material model for IN718 given in Section 5.2.1 are employed. It takes 10 load steps to finish the sequential layer-wise simulation. As new layers are laid onto the lower layers, the residual stress distribution in those lower layers evolves correspondingly. Taking the 4th layer of the meso-scale model as the example, directional residual stress in the x-axis direction (see Figure 5.5) of the center area far away from the boundary surface in the activation step (4th load step) and the following activation step (5th load step) is shown in Figure 5.6. It is found that due to shrinkage of the 5th layer, residual stress in most area of the concerned 4th layer is relaxed significantly.

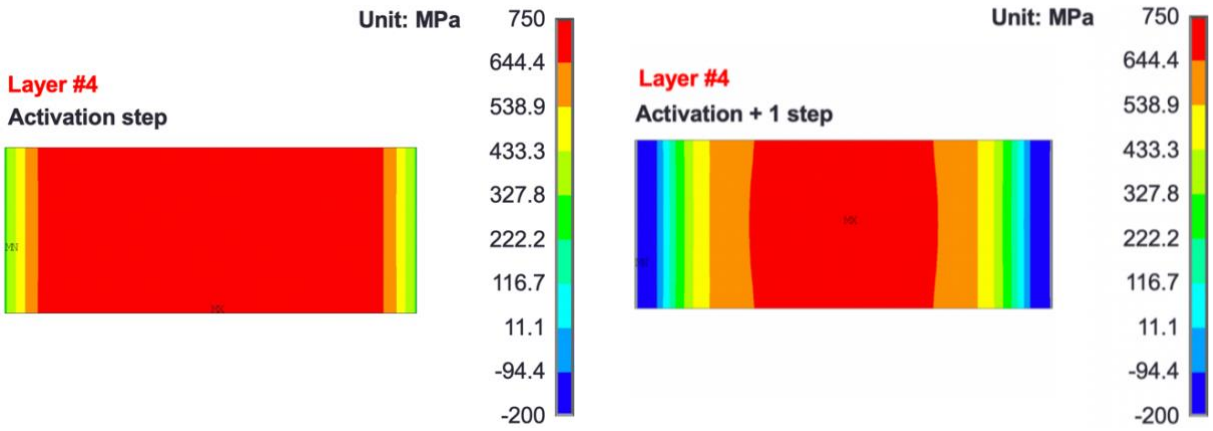

(a) (b)

Figure 5.6 Directional Residual Stress Distribution in the Core Area of the 4th Layer in the (a) Activation and (b) Following-Activation Step

In order to better elucidate the stress relaxation effect due to the addition of the upper layer, the directional residual stress along the center line of the 4th layer is plotted in Figure 5.7. Meanwhile, the stress difference between the activation and following-activation step is also shown in the figure (black dashed line). It can be seen that the stress relaxation effect is significant given the residual stress magnitude. This stress relaxation phenomenon is an important feature of

the standard layer-by-layer simulation. Therefore, it should be taken into accounts numerically when the ELLM is developed.

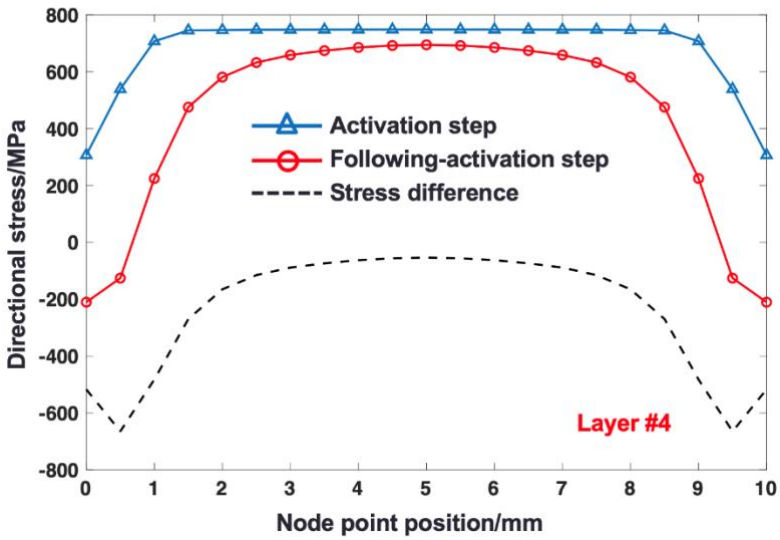

Figure 5.7 Stress Relaxation Effect on the 4th Layer due to Addition of the Upper Layer in the Meso-Scale Modeling

As shown in Figure 5.7, the stress relaxation extent of different material points even in the same layer is quite different. However, for most positions especially in the middle region, the stress relaxation amount is nearly flat. In order to further investigate the stress relaxation phenomenon, stress evolution histories of several special points in the 4th layer are extracted. The positions of the concerned points are shown in Figure 5.8. Note Node #1 represents the positions attach to the outer surface of the meso-scale model.

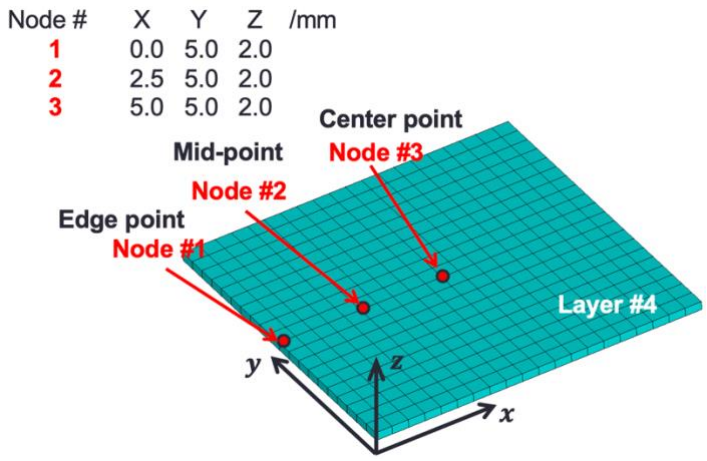

Figure 5.8 Positions of the Concerned Points in the 4th Layer for Stress Evolution Observation

Accordingly, directional stress evolution history curves of the three sample points are shown in Figure 5.9. It is shown that the material points (mid-point and center point) far away from the edges experience nearly linear stress reduction due to the stress relaxation effect caused by the shrinkage of the upper deposition layers (Layer #5~10).

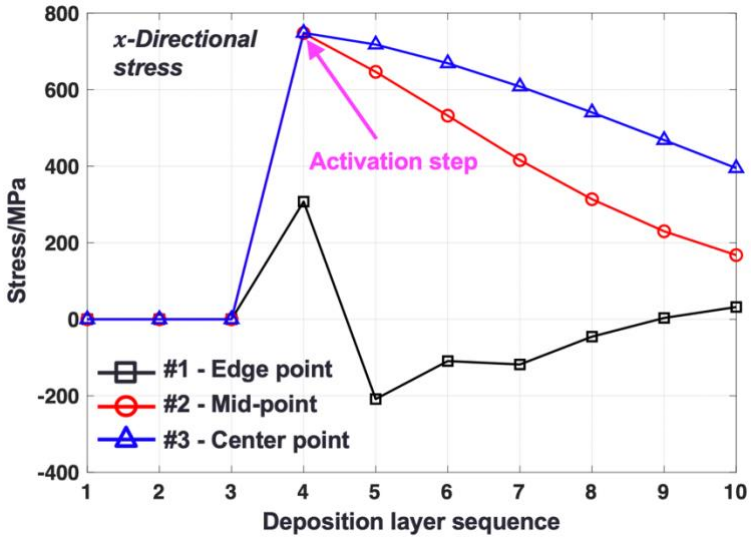

Figure 5.9 Directional Stress Evolution History of Three Sample Points in the 4th Layer

In addition, the elastic and plastic strain evolution history curves of the three sample points are shown in Figure 5.10. It seems that except the sample point on the edge, the remaining two material points experience nearly linear elastic stress relaxation since their plastic strain keep the same in the deposition process. Moreover, the elastic strain tends to be flat with depositing of 9th and 10th layer. It indicates that the shrinkage-related stress relaxation influence on the 4th layer by those two layers already becomes weak.

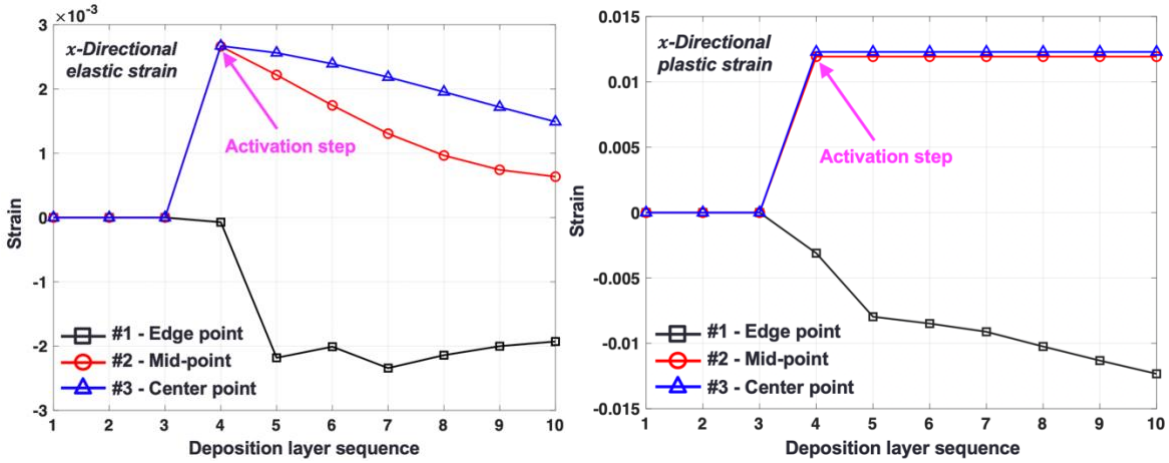

(a) (b)

Figure 5.10 Directional (a) Elastic and (b) Plastic Strain Evolution History of Three Material Points in the Meso-Scale Model

It is noted the stress and strain evolution history curves of the edge point show quite different features as seen in Figure 5.10. According to the simulation experience, the edge effect on the residual stress usually occurs in a limited region compared with the much larger bulk volume area in the large-scale metal builds. Therefore, the behavior of edge point (Node #1) cannot represent typical evolution feature for most of the material points in the deposition layers. Moreover, compared with the center material point (Node #3) which is right in the middle of the

layer, mid-point (Node #2) is more typical to represent many points in the bulk volume of the meso-scale model. Therefore, in the following it is focused on the stress/strain evolution history of the mid-point to reveal more features of the layer-by-layer simulation. Elastic and plastic strain evolution history of the mid-point are plotted in Figure 5.11, specifically. The plastic strain keeps flat against the upper layer depositing sequence. Based on this phenomenon, it is assumed that the material addition from some upper layers contributes linearly to the elastic stress reduction of the lower layers. The reduction amount of elastic strain due to the layer-by-layer material addition behavior is also annotated in the figure. It is worth clarifying that only x-directional stress/strain evolution history is shown in this section. Two reasons can be counted for this. One the one hand, due to symmetry of the meso-scale model, the y-directional stress/strain evolution history is quite similar to those results demonstrated in Figure 5.9 and 5.10. On the other hand, it is found the vertical/z-directional stress/strain is relatively insignificant regarding the magnitude. Thus, the stress/strain evolution feature in the vertical build direction is neglected in this dissertation.

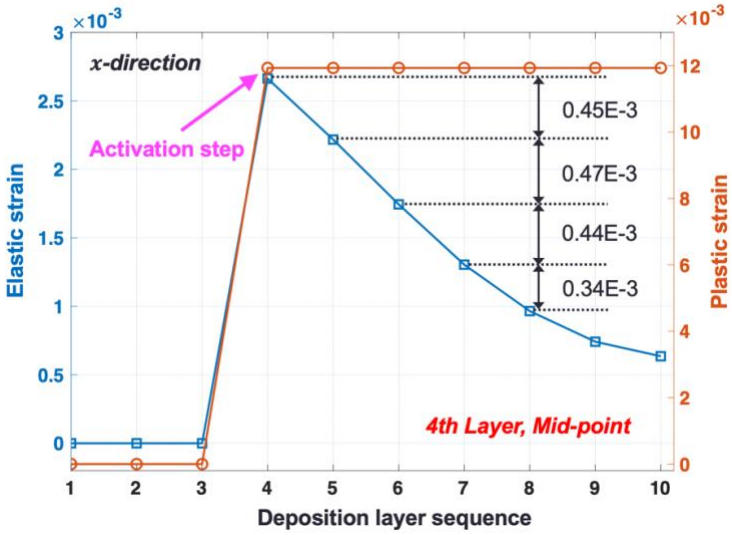

Figure 5.11 Typical Directional Strain Evolution History for a Material Point in Bulk Volume of the Meso-Scale Model

Based on the above findings, for any layer numbered by N in a metal build, typical directional stress evolution history of a material point inside the concerned layer can be illustrated by the black curve in Figure 5.12 as follows. In particular, linear reduction for the stress in the end of the evolution history is caused by the material addition of the $N+1$ and $N+2$ layer, respectively. Therefore, a feasible idea is proposed that for the 2-layer lumping case, since N and $N+1$ layer would be activated at the same load step, the stress evolution history should behave like what the blue dashed line shows. In this way, it can ensure that the stress level in the lower layer of the two lumped layers may reach the lower value compared with the case where only single equivalent layer is activated. This suggests the specific constitutive material model tuning for 2-layer ELLM. Moreover, for the 3-layer ELLM case, the N, $N+1$ and $N+2$ layers are activated at the same time. The stress evolution history of the bottom layer (Layer N) should behave as the red dashed line shows, while the middle (Layer $N+1$) and top layer (Layer $N+2$) should behave as the blue dash and black solid line (without stress reduction) elucidate, respectively. Specific material constitutive models, especially having different yield stress criterion, should be employed for different layers in the 2-layer and 3-layer ELLM. This manner can guarantee that different equivalent layers in the lumping super layer may reach different stress level as they should in the benchmark layer-wise simulation though they are activated and deformed at the same load step. In addition, the components of ISV in the in-plane directions should also be adjusted by the corresponding amount given the strain reduction effect as shown in Figure 5.11 and 5.12.

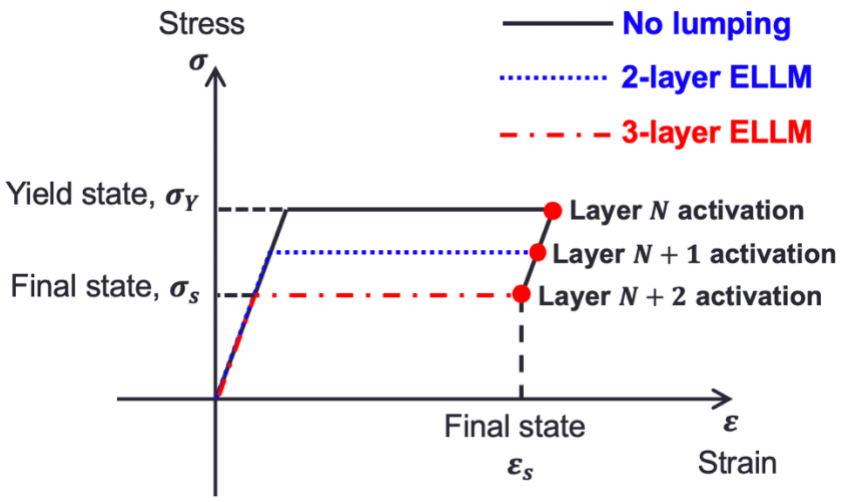

Figure 5.12 Residual Stress Evolution and Equivalent Material Models due to 2-Layer and 3-Layer Lumping

The critical issue is how to determine the different artificial material property models (MPMs) used for different equivalent layers lumped in the ELLM. A preliminary idea is to combine the stress relaxation effect into the inherent strain values and yield stress. Inherent strain values of the lower layers in a lumped super layer should be reduced by the amount as shown in Figure 5.11. To make the ELLM easy to implement, the first three strain reductions as shown in Figure 5.11 are averaged, and as a result, uniform reduction amount of 0.45×10^{-3} is adopted to tune the inherent strain values for the MPMs. Moreover, uniform reduction amount of 112 MPa is adopted based on Figure 5.9 to tune the yield stress values in the MPMs to control the residual stress level in the ELLM. The elastic modulus can keep the same for all the lumped layers as observed in Figure 5.12. Numerical examples including the 4-layer ELLM case are employed to validate the ELLM in the following section. Therefore, at most three adjusted MPMs will be involved later. All the four MPMs including the real one for IN718 are listed in Table 5.2 in order to facilitate understanding for the material property adjustment in the ELLM implementation. Note the inherent strain component in the vertical direction keeps constant (0.015) in order to make the

ELLM simplified for implementation. This manner is reasonable because it is found that influence of the vertical inherent strain component is insignificant on the predicted results in the layer-wise simulation.

Table 5.2 MPMs for IN718 Used in the ELLM Implementation

MPM #	Elastic modulus (GPa)	Yield strength (MPa)	ISV
1 (Real)	185	750	$(-0.015, -0.015, 0.015)$
2	185	638	$(-0.01455, -0.01455, 0.015)$
3	185	526	$(-0.01410, -0.01410, 0.015)$
4	185	414	$(-0.01365, -0.01365, 0.015)$

5.3 Validation Examples for ELLM

A larger cantilever beam is selected as the validation example to investigate the ELLM. Geometrical profile and finite element mesh of the cantilever beam is shown in Figure 5.13. The length, width and height of the cantilever beam is 60, 15 and 16 mm, respectively. Thickness of the teeth-like support structures is 2 mm and there are 12 bars beneath the reaching-out beam. Height of the support structures is 11 mm, indicating the height of the reaching-out beam is 5 mm. In addition, gap size between two adjacent support bars is 2 mm. Length of the base on the left of the cantilever beam is 12 mm.

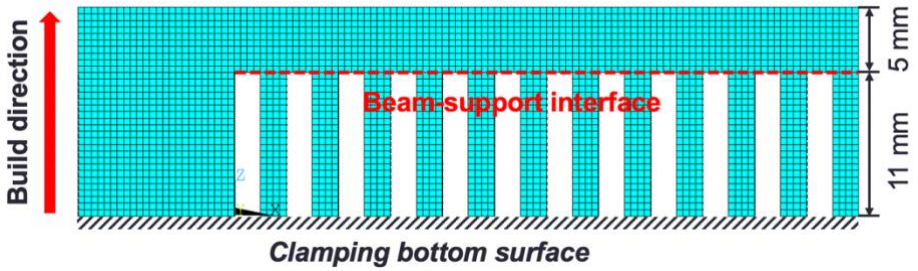

Figure 5.13 Geometrical Profile and Finite Element Mesh of the Large Cantilever Beam

Given the symmetry condition in the problem, only half of the entire deposition needs to be simulated. In this half model, there are 41760 8-node Solid185 elements. The LAT is 0.5 mm, resulting in 32 equivalent mesh layers in the layer-wise simulation. It suggests that there are 22 mesh layers in the teeth-like support structures within the height from 0 to 11 mm. There are 10 more layers in the remaining volume of the cantilever beam. Accordingly, it takes 32 load steps to finish the layer-by-layer simulation.

The dominant shrinkage deformation occurs along the beam-support interface (see Figure 5.13) in the length direction of the cantilever beam as shown in Figure 5.14(a). Moreover, the dominant residual deformation occurs at the end of the beam in the vertical build direction as shown in Figure 5.14(b). The simulation results are referred to as the benchmark no-lumping case in the following contents.

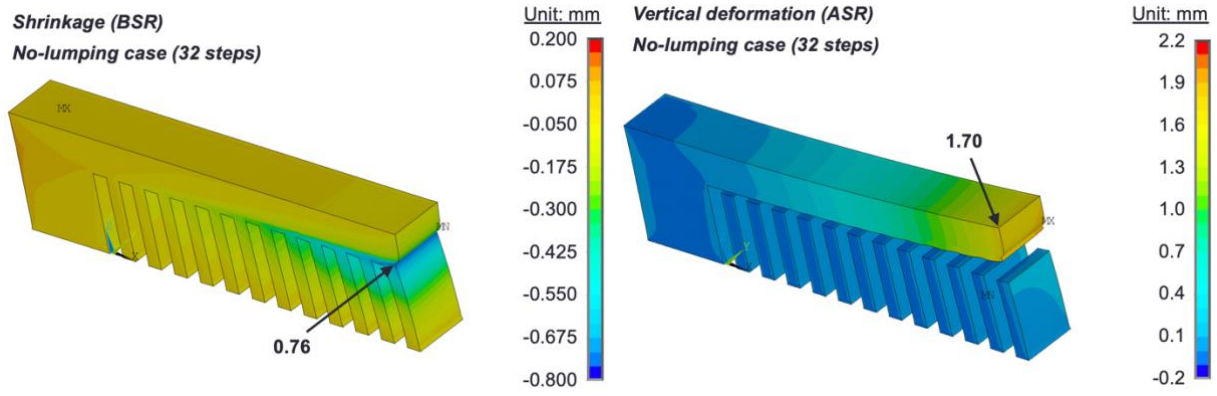

(a) (b)

Figure 5.14 Residual Deformation in the (a) Longitudinal and (b) Vertical Build Direction before (BSR) and after Support Removal (ASR) Simulated Using 32 Load Steps (Benchmark No-Lumping Case)

In order to validate the simulation results, the large cantilever beam was fabricated by PBF (EOS M290 printer) using the same process parameters involved in Section 5.2.1. After the fabrication process, W-EDM was employed in cut off the support structures along the solid-support interface. In addition, a 3D laser scanning device was used to measure the overall residual deformation of the cantilever beam before and after the support structures were removed. For the as-built cantilever beam, the maximum shrinkage occurs at the solid-support interface and is 0.80 mm through the experimental measurement. The error between the simulation result (0.76 mm) and the experimental result is 5.0%. Moreover, the vertical residual deformation obtained by the simulation and experiment along center line of the top surface of the cantilever beam was shown in Figure 5.15. Good agreement can be found between the simulation and experimental result. Therefore, good accuracy of the benchmark no-lumping case has been strongly validated.

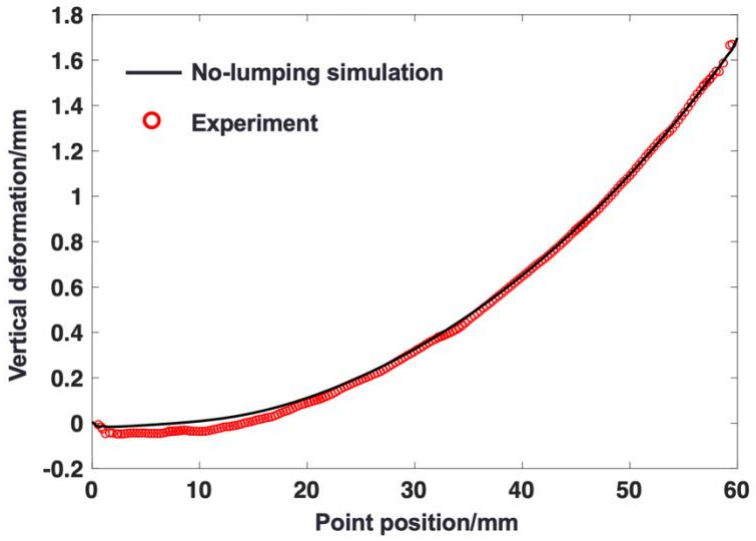

Figure 5.15 Vertical Deformation along Center Line of the Top Surface of the Cantilever Beam after Support Removal Obtained by the No-Lumping Simulation and Experiment

5.3.1 2-Layer ELLM

As discussed in Section 5.2.2, when 2-layer ELLM is involved, one tuned MPM (#2) should be adopted besides the real MPM (#1) used for IN718 in the no-lumping case. After the MPMs are set up, two adjacent mesh layers are lumped into a super layer and activated simultaneously in one load step. As a result, the 32-step simulation is reduced to 16 load steps. The second MPM for IN718 involves some adjusted material property parameters as shown in Table 5.2.

MPM #2 is the artificial constitutive model used specifically to tune the inherent strains and yield stress for the low layer in the 2-layer ELLM case. Accordingly, the entire model is divided into two sections prepared to have two sets of material property parameters. The equivalent layer-based division is shown in Figure 5.16.

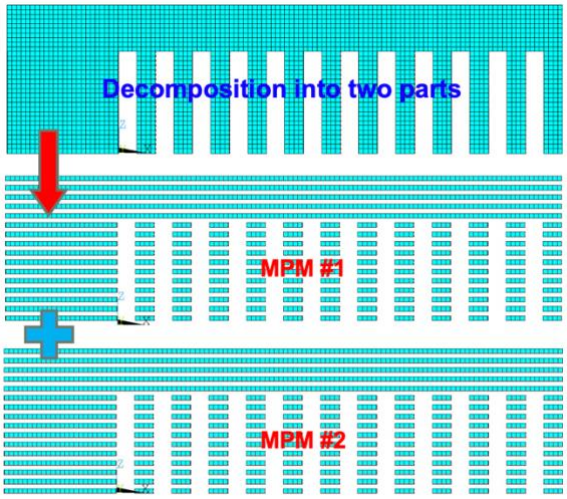

Figure 5.16 Division of the Equivalent Layers in the Cantilever Beam Ready for Assignment of Two MPMs

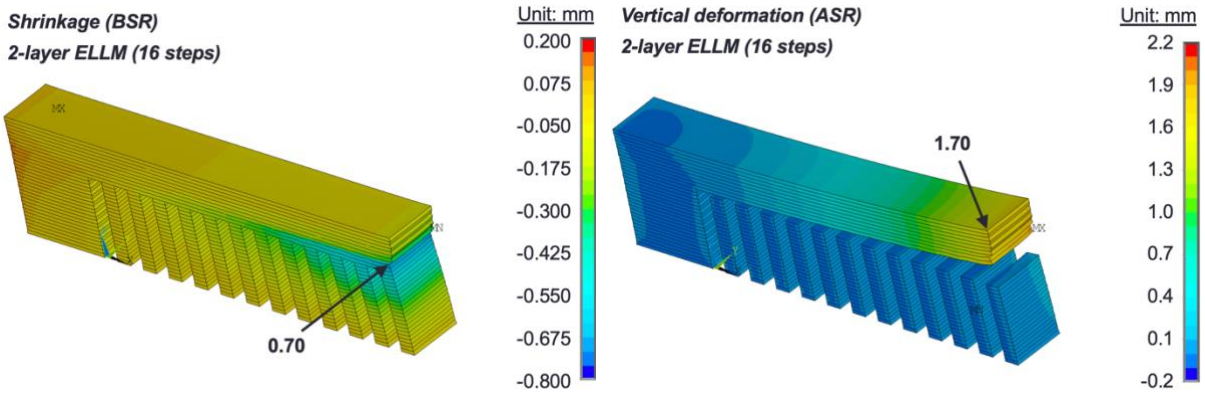

(a) (b)

Figure 5.17 The (a) Longitudinal and (b) Vertical Residual Deformation before (BSR) and after Support Removal (ASR) Using 2-Layer ELLM Involving One Tuned MPM

Certainly, it takes shorter time to finish the 16-step simulation than the 32-step no-lumping case. The obtained residual deformation before and after removal of the teeth-like support structures is shown in Figure 5.17. Compared to those results in the benchmark no-lumping case

(see Figure 5.14), the prediction error is quite small, indicating the good accuracy of the 2-layer ELLM employing one tuned MPM.

As an interesting supplement, the computed residual deformation in vertical build direction after support removal using 2-layer LLM without the tuned MPM is shown in Figure 5.18 as a comparison. It is seen that the prediction error for the maximum vertical deformation becomes larger compared to Figure 5.17(b) with reference to the benchmark results in Figure 5.14. This phenomenon strongly verifies that the material property tuning is quite necessary for the ELLM in order to improve the lumping-based simulation accuracy.

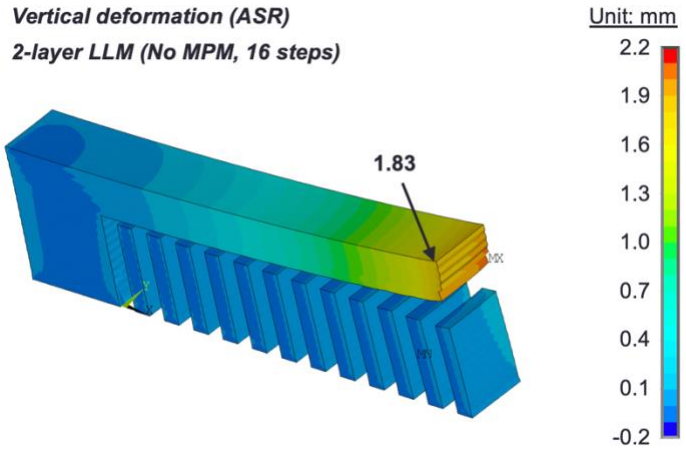

Figure 5.18 Vertical Residual Deformation after Support Removal (ASR) Using 2-Layer LLM without Tuned MPM

5.3.2 3-Layer ELLM

As a further step, the 3-layer ELLM is studied in this example. Correspondingly, two more tuned MPMs (#2 and #3) are needed in addition to the real MPM (#1) for IN718. Three adjacent equivalent layers are lumped into a super layer in the 3-layer ELLM case. As a benefit, only 11

load steps are needed for the 32-layer model. The computational time can be further reduced compared to the 2-layer ELLM case in Section 5.3.1. In addition to MPM #1 and #2 identical to those parameters in Section 5.3.1, the third MPM (#3) uses the specific material property parameters as seen in Table 5.2. Given the three MPM. Accordingly, the entire cantilever beam model is divided into three sections for layer-wise assignment of material properties.

It takes much shorter time to finish the 11-step simulation than the 2-layer ELLM case and the 32-step benchmark case. The obtained residual deformation before and after removal of the support structures is shown in Figure 5.19. Compared to those results in the benchmark case (see Figure 5.14), the prediction error is acceptable though it increases slightly due to the lumping effect compared to the 2-layer ELLM case. Note the gray color near the arrow in Figure 5.19(a) suggests shrinkage magnitude is beyond the maximum value of the legend color band.

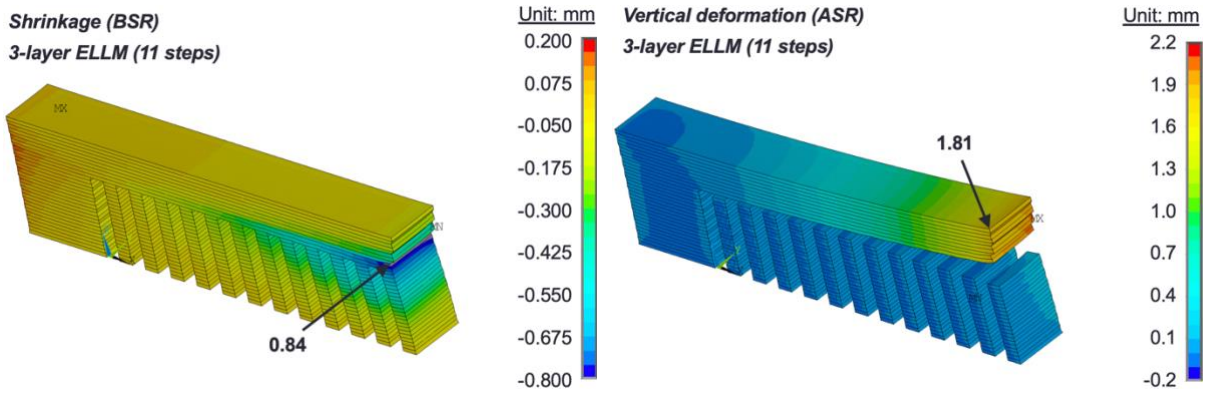

(a) (b)

Figure 5.19 The (a) Longitudinal and (b) Vertical Residual Deformation before (BSR) and after Support Removal (ASR) Using 3-Layer ELLM with Two Tuned MPMs

5.3.3 4-Layer ELLM

Another trial is to develop the 4-layer ELLM in order to accelerate the layer-wise simulation to a further extent. Correspondingly, three additional tuned MPMs (#2~#4) are needed in addition to the real MPM (#1) for IN718. Four adjacent equivalent layers are lumped into a super layer in the 4-layer ELLM case. As a benefit, only 8 load steps are needed for the 32-layer model. The computational time can be further reduced compared to the 2-layer and 3-layer ELLM case in Section 5.3.1 and 5.3.2. Adjusted parameters of the involved fourth MPM (#4) in this example are already given in Table 5.2. Since four MPMs are involved for the 4-layer ELLM case, accordingly, the entire cantilever beam model is divided into four sections.

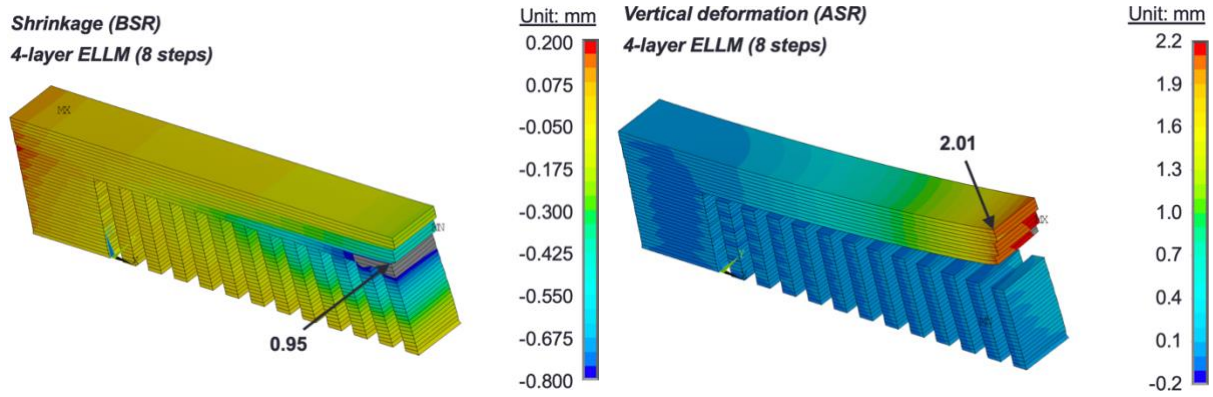

(a) (b)

Figure 5.20 The (a) Longitudinal and (b) Vertical Residual Deformation before (BSR) and after Support Removal (ASR) Using 4-Layer ELLM with Three Tuned MPMs

It takes a lot shorter time to finish the 8-step simulation than the above two ELLM cases and the 32-step benchmark case. The obtained residual deformation before and after removal of the teeth-like structures is shown in Figure 5.20. Compared to those results in the benchmark case

(see Figure 5.14), the overall trend of the residual deformation before and after removal of support structures matches well.

However, the prediction error increases more significantly due to the lumping effect. The gray color area, which suggests residual deformation magnitude beyond the maximum value of the legend color band, becomes obviously larger in Figure 5.20 compared with Figure 5.19. One possible reason for the slightly increased prediction error is attributed to the geometry of the cantilever beam. The sudden transitional change of cross sections in the build direction, like the solid-support interface of the cantilever beam, is not considered in the meso-scale modeling. However, due to layer lumping operation, four adjacent layers are deformed in the same load step including the 21st to 24th equivalent layers containing the solid-support interface. Given weak constraint of the teeth-like lower layers, the upper layers above the solid-support interface can shrink more in the longitudinal direction as shown in Figure 5.20(a). Moreover, the vertical deformation near the solid-support interface already increases a little before support removal. Thus, after support removal, vertical residual deformation becomes even larger compared with the benchmark 32-step simulation. In fact, this reason can also explain the slight increase of the simulation error in the 3-layer ELLM case in Section 5.3.2.

Therefore, in order to address this issue, a reasonable correction is to divide the entire cantilever beam into two sections in the build direction. The two-section division (TSD) is shown in the Figure 5.21. The first section consists of 22 equivalent layers and the second section contains 10 equivalent layers. The first section is simulated layer-wisely first using 6 load steps because only two remaining layers are activated in the 6th step. Starting from the 23rd layer, four MPMs are sequentially assigned to the equivalent layers in the second section layer-wisely. Three more

load steps are needed to finish the simulation while the two top layers (Layer #31 and #32) are activated in the last step.

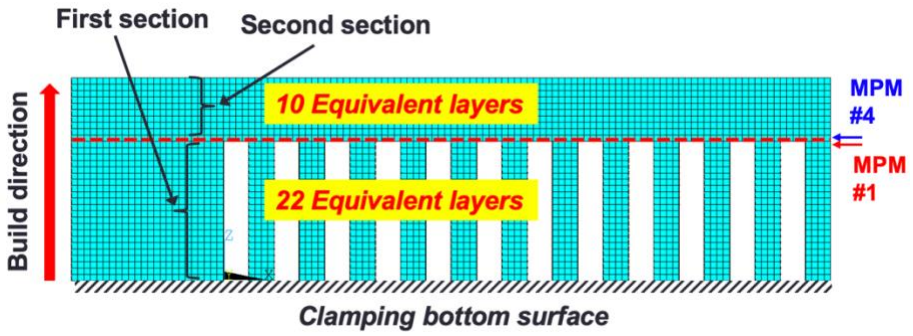

Figure 5.21 Two-Section Division (TSD) of the Cantilever Beam for the 4-Layer ELLM Case

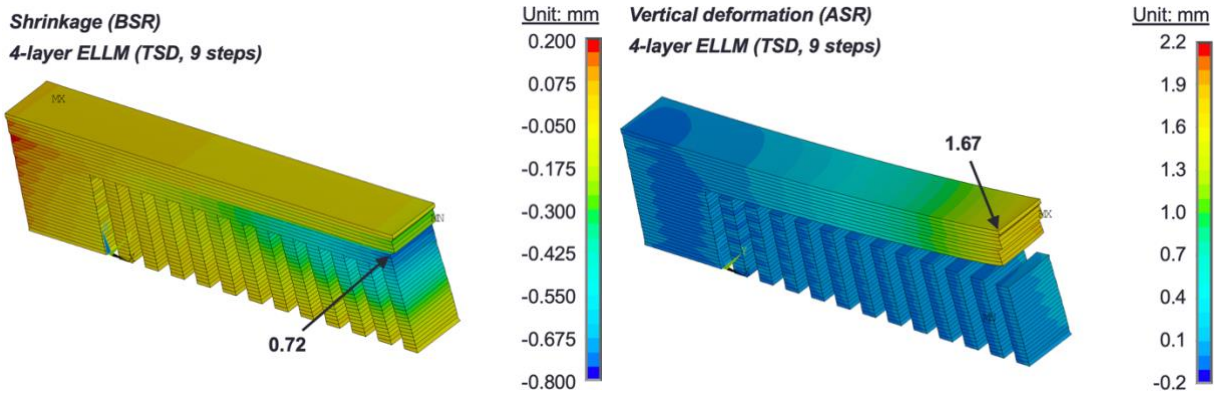

(a) (b)

Figure 5.22 The (a) Longitudinal and (b) Vertical Residual Deformation before (BSR) and after Support Removal (ASR) Using 4-Layer ELLM in Combination with Two-Section Division (TSD)

Due to TSD, computational time increases slightly compared with the previous 8-step simulation. However, the simulation accuracy is improved significantly as shown in Figure 5.22. For example, the maximum vertical displacement of the picked point is 1.67 mm. Compared with the benchmark case (1.70 mm, see Figure 5.14), the simulation error is reduced to 1.8%. In

summary, the results have validated the necessity of the TSD or multi-section division (MSD) technique especially when some metal builds with transitional cross sections in the build direction are considered using the ELLM in the layer-wise simulation.

5.3.4 Discussions

The computational time for all the involved cases is listed in Table 5.2 while the same desktop computer was used as in Section 5.2. It is shown that the computational time has been reduced significantly due to the ELLM. For example, if the 4-layer ELLM case with TSD is compared to the no-lumping case, the computational time has been decreased by 70%.

Table 5.3 Computational Time of the Five Simulation Cases for Large Cantilever Beam

Case #	Layered depositing simulation/min	Support removal simulation/min	Total time/min	Improvement (%)
No-lumping (32 steps)	9	3	12	---
2-layer ELLM (16 steps)	4	3	7	42
3-layer ELLM (11 steps)	3	2	5	58
4-layer ELLM (8 steps)	1.5	2	3.5	71
4-layer ELLM (TSD, 9 steps)	1.6	2	3.6	70

Moreover, thus far we have extended the study on layer-wise simulation acceleration far enough to the 4-layer ELLM case. The maximum displacements before and after cutting as pointed in the above figures are collected and listed in Table 4 for a detailed comparison between different cases. In addition, besides the comparisons of the overall residual deformation involved in Section

5.3.1~5.3.3, vertical residual deformations along center line of the top surface of the cantilever beam after support removal are plotted in Figure 5.23 in order to better demonstrate the performance of different ELLM cases. Generally, the ELLM cases using tuned MPMs can lead to improved accuracy of the layer-wise simulation. Though larger error is found when more layers are lumped, for example, in the 4-layer ELLM case, good accuracy can be obtained when a specific TSD technique is combined with ELLM.

Table 5.4 Maximum Displacement before (BSR) and after Support Removal (ASR) for the Large Cantilever Beam

Case #	Displacement (BSR)	Error (%)	Displacement (ASR)	Error (%)
No-lumping (32 steps)	0.76	---	1.70	---
2-layer ELLM (16 steps)	0.70	8.6	1.70	0
3-layer ELLM (11 steps)	0.84	10.5	1.81	6.5
4-layer ELLM (8 steps)	0.95	25.0	2.01	18.2
4-layer ELLM (TSD, 9 steps)	0.72	5.3	1.67	1.8

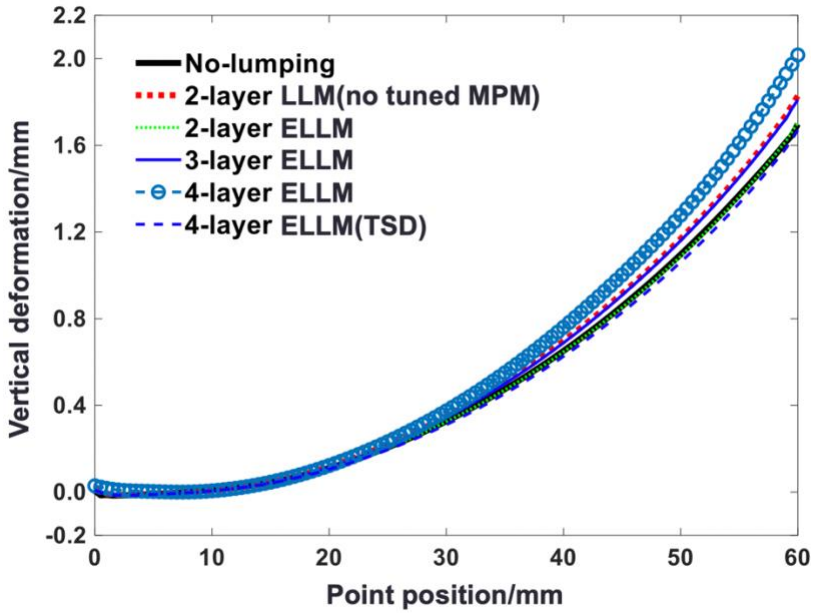

Figure 5.23 Comparison of the Vertical Deformation (ASR) along the Top Surface Center Line of the Cantilever Beam Obtained in No-Lumping and Different ELLM Cases

However, if a closer look is taken at the results (see Figure 5.20 and 5.22) obtained by the 4-layer ELLM cases in Section 5.3.3, it is found that the longitudinal shrinkage of the as-built cantilever beam shows incorrect distribution pattern, especially for those points on the outer surface nearby the solid-support interface. The shrinkage deformation does not look smooth enough compared with the simulated results in the benchmark no-lumping case (see Figure 5.14(a)). This irregular shrinkage pattern is caused by too much lumping in the ELLM. When more equivalent layers are merged into one super layer, they are activated and deformed simultaneously in one load step, which is inconsistent with the physical bottom-up nature of the PBF process. As a result, when more and more equivalent layers are lumped into one super layer, the ELLM can lead to larger error in the predicted residual deformation of the large as-built metal components. Therefore, the 4-layer ELLM case is suggested as the extreme case that is employed to accelerate the simulation to the largest extent while good simulation accuracy can be ensured.

5.4 Conclusions

In this chapter, the ELLM is developed in order to accelerate the layer-by-layer simulation as much as possible for predicting residual stress and deformation in those large components fabricated by the PBF process. A couple of conclusions have been obtained as follows:

(1) The RLT of 0.04 mm would result in underestimation of residual stress and deformation when adopted as the LAT for IN718 in the MISM-based layer-by-layer simulation. Instead, the reasonable LAT of equivalent layers is found in the range of 0.4 to 0.6 mm for the layer-wise simulation.

(2) A meso-scale model using the LAT of 0.5 mm is established to study residual stress evolution in the layer depositing process. Based on the observation, tuned MPMs are proposed in combination with the ELLM. Yield stress and inherent strains in the tuned MPMs are adjusted layer-wisely to avoid overestimation of residual stress and deformation caused by the lumping layer effect.

(3) The 2-layer, 3-layer and 4-layer ELLM have been validated based on the experimental results for a large cantilever beam containing 32 equivalent layers with a LAT 0.5mm. While good simulation accuracy is ensured, the computational time of the simulation can be reduced up to 70% by the 4-layer ELLM case.

(4) An interesting finding is that, for metal components with changing cross sections in the build direction, TSD or MSD of the component is necessary to be combined with the ELLM in order to improve layer-wise simulation accuracy.

Thus far, lumping four equivalent layers together seems to be the most we can do using the proposed method without a significant loss in accuracy. It is promising to incorporate the accelerated layer-wise simulation with high fidelity into some structural design frames, such as

iterative topological optimization of support structures to mitigate residual stress and deformation of large metal components [81]. Otherwise, it is impractical to utilize the MISM-based layer-wise simulation as the solver in the optimization process because of too expensive computational time. However, non-smooth longitudinal deformation pattern has been found in the LLM-based simulation. This phenomenon cannot be avoided when more and more equivalent layers are lumped and deformed simultaneously. In order to address this issue, layer-dependent ISV with variation in the vertical build direction can be helpful instead of the uniform ISV in this chapter, because this manner can tune the thermal expansion deformation difference between the adjacent super layers.

6.0 Conclusions

6.1 Main Contributions

The research works in this dissertation are mainly focused on development of numerical simulation methods for metal AM process including DED/LENS and PBF such as DMLS. Instead of the time-consuming conventional thermomechanical simulation method, the ISM has been considered for fast simulation. Since the original ISM is inaccurate when applied to the metal AM process, a novel numerical method named MISM has been proposed for the first time. The goal is to obtain efficient yet accurate prediction of residual stress and deformation in the final metal components. The main contributions of this dissertation are summarized as follows:

(1) **The MISM is proposed to give more accurate estimation of inherent strains considering contribution of residual strain in the intermediate and final steady state of the Ti64 depositions.** The modified inherent strain values are extracted from the detailed thermomechanical simulation of metal LENS process. The modified inherent strains are applied to the part as CTEs equivalently. Only static elastoplastic analysis needs to be employed with a unit temperature increase as the thermal load. In order to extend the MISM to larger parts containing many deposition layers, the small-scale model consisting of two deposition lines is established as the typical simulation for single-walled structures deposited by LENS process. The predicted residual deformation of single-walled structures based on the MISM is compared with both full-scale detailed thermomechanical simulation and the experimental results. Good agreement has been found and thus the accuracy of the proposed MISM is strongly validated.

Moreover, excellent efficiency of the MISM has been verified given the computational time has been reduced greatly when compared to detailed thermomechanical simulations.

(2) **A feasible way is established in order to adapt the MISM to the PBF process involving Ti64 and Inconel 718 material.** Detailed definition of the intermediate state is modified a little for any material point in the depositions given the difference between LENS and PBF process such as the powder bed and large fixed substrate. Since it is impractical to implement full-scale detailed thermomechanical simulation of a large PBF component, a small-scale 2-layer block model is built as the representative volume to simulate typical thermal and mechanical features of the PBF process. Moreover, the layer-wise rotational laser scanning strategy is also carefully considered in the small-scale detailed simulation. Based on the adapted MISM, modified inherent strains are extracted from the small-scale process modeling. Then the inherent strains are applied to the large components as CTEs in a layer-by-layer manner. A cantilever beam and a complex canonical part are investigated. The predicted residual deformation of those metal components is compared with experimental results. Good accuracy of the proposed MISM is well validated. As a result, the part-scale simulation for large PBF components becomes available for the first time. In addition, the influence of the layer activation thickness in the layer-by-layer simulation is also investigated. It is found that only a reasonable number of thin layers can be merged into an equivalent layer in the layer-by-layer simulation in order to ensure the simulation accuracy.

(3) **Application of the MISM to the thin-walled square lattice structures fabricated by the PBF process is studied.** The modified inherent strain values are obtained based on a small-scale detailed simulation on a representative volume containing only four thin walls. Asymptotic homogenization method is then employed to compute effective mechanical properties for the thin-walled square lattice structures with different volume densities, including equivalent inherent

strains and elastic modulus. With the help of effective material properties especially the homogenized inherent strains, simulation of the thin-walled square lattice structures can be performed simply through adopting solid continuum models instead of considering many details like the thin walls. Some blocks consisting of thin-walled square lattice structures are fabricated by PBF and the residual deformation of these specimens are measured experimentally. By comparison to the experimental results, good accuracy of the homogenized inherent strains and elastic modulus has been validated. Moreover, as a benefit of the MISM in combination with the asymptotic homogenization, computational time of the layer-by-layer simulation for the thin-walled square lattice structures has been reduced greatly.

(4) **In order to further accelerate the layer-by-layer simulation for any PBF component, the ELLM is developed.** First, instead of using RLT, a reasonable LAT is determined in order to guarantee good accuracy of the MISM-based layer-by-layer simulation. Then using the LAT, meso-scale modeling is employed to observe the residual stress/strain evolution features changed with layered addition in the layer-wise simulation. Based on the meso-scale modeling, tuned MPMs are proposed in order to control the residual stress level and avoid overestimation of residual stress and deformation caused by only lumping layer effect. The proposed ELLM in combination with tuned MPMs is compared with the benchmark no-lumping case. Good accuracy of the 2-layer, 3-layer and 4-layer ELLM case has been validated through the comparison. Moreover, computational time of the layer-wise simulation can be reduced significantly. For the 4-layer ELLM case, the consumed time can be decreased by 70% in comparison to the benchmark no-lumping case.

6.2 Future Works

Though the MISM for metal AM process has been fully developed and the good accuracy and computational efficiency have been fully shown in this dissertation, there are still a lot of important topics that need to be carefully investigated. The potential future works based on the research works in this dissertation are summarized as follows.

(1) **Extensive research is needed to determine how to incorporate the influence of different laser scanning strategies in the MISM for the PBF process.** Both parallel and rotational line laser scanning strategies have been commonly seen in the metal AM process. However, different material properties like directional elastic modulus and yield stress can be caused by the different laser scanning strategies. Moreover, the modified inherent strains are also different for different laser scanning strategies according to my simulation experiences. The material anisotropy should be considered in the MISM to better simulate the metal PBF process when different laser scanning strategies are employed. In particular, for those rotational laser scanning strategies, inherent strain homogenization can be employed in order to find a homogenized inherent strain vector for a certain repeated laser scanning pattern. Numerical implementation details need to be further studied.

(2) **It is necessary to consider parallelization and employing GPU to further accelerate the MISM-based simulation.** Thus far, the MISM-based simulation has been performed in a sequential layer-by-layer manner for large metal components given the bottom-up nature of the AM process. However, this may result in a limitation for further accelerating the simulation, even though the ELLM has been developed preliminarily in Chapter 5. By parallelization, the layered mechanical analysis can be implemented in a series of computers first, and then assembled simultaneously to reach the final steady state for any large component. It is highly promising to

accelerate the numerical simulation for metal AM process to the largest extent. If this future work can be realized, the MISM-based simulation can be incorporated as a powerful solver into the topology optimization framework for metal AM process in order to decrease the residual stress and deformation level.

(3) **Machine learning can be introduced into the MISM-based simulation.** Machine learning has demonstrated its powerful ability of finding the linkage of different data groups for linear and nonlinear systems. On the one hand, it is promising to employ machine learning techniques like neural networks to link the large number of specific process parameters such as laser power, laser scanning velocity and material properties to the corresponding inherent strain values for a certain metal material. On the other hand, the MISM-based nonlinear elastoplastic simulation can provide large number of data points linking the undeformed geometry with the deformed geometry after the metal AM process. The big datasets can be employed to train neural networks in order to build the relationship between undeformed and deformed metal components. Based on the trained neural networks, distortion compensation for the metal components can be figured out. In this way, the residual deformation of large components can be reduced. As a result, manufacturing precision and surface quality of the metal parts can be improved.

(4) **Further study is needed to investigate how to extend the proposed MISM to AM depositions consisting of multiple materials, e.g., metal and ceramics.** The sensitivities of AM process parameters should be investigated to show possible influence on extracted inherent strains for different materials. A straightforward solution is to apply different modified inherent strains for different regions in a metal component containing multiple materials. However, it is still challenging to figure out how to establish reasonable small-scale simulations and obtain accurate inherent strains corresponding to different regions and materials. In addition, for other materials

like ceramics, fusion and solidification phenomena in the depositing process can be quite different from metal materials. Therefore, some necessary modifications should be made to the developed thermomechanical model in this dissertation in order to better simulate the fusion and solidification of other AM materials like ceramics in the future.

Bibliography

1. Zhang, P., et al., *Efficient Design-Optimization of Variable-Density Hexagonal Cellular Structure by Additive Manufacturing: Theory and Validation.* Journal of Manufacturing Science and Engineering, 2015. **137**(2): p. 021004.

2. Cheng, L., et al., *Efficient design optimization of variable-density cellular structures for additive manufacturing: theory and experimental validation.* Rapid Prototyping Journal, 2017. **23**(4): p. 660-677.

3. Ding, J., et al., *A computationally efficient finite element model of wire and arc additive manufacture.* The International Journal of Advanced Manufacturing Technology, 2014. **70**(1-4): p. 227-236.

4. DebRoy, T., et al., *Additive manufacturing of metallic components–process, structure and properties.* Progress in Materials Science, 2018. **92**: p. 112-224.

5. Gibson, I., D.W. Rosen, and B. Stucker, *Additive Manufacturing Technologies: Rapid Prototyping to Direct Digital Manufacturing*. 2009: Springer.

6. Kruth, J.P., M. Leu, and T. Nakagawa, *Progress in additive manufacturing and rapid prototyping.* CIRP Annals-Manufacturing Technology, 1998. **47**(2): p. 525-540.

7. Murr, L., et al., *Next-generation biomedical implants using additive manufacturing of complex, cellular and functional mesh arrays.* Philosophical Transactions of the Royal Society of London A: Mathematical, Physical and Engineering Sciences, 2010. **368**(1917): p. 1999-2032.

8. Hague, R., I. Campbell, and P. Dickens, *Implications on design of rapid manufacturing.* Proceedings of the Institution of Mechanical Engineers, Part C: Journal of Mechanical Engineering Science, 2003. **217**(1): p. 25-30.

9. Hopkinson, N., R. Hague, and P. Dickens, *Rapid manufacturing: an industrial revolution for the digital age*. 2006: John Wiley & Sons.

10. Santos, E.C., et al., *Rapid manufacturing of metal components by laser forming.* International Journal of Machine Tools and Manufacture, 2006. **46**(12): p. 1459-1468.

11. Zhang, P., J. Liu, and A.C. To, *Role of anisotropic properties on topology optimization of additive manufactured load bearing structures.* Scripta Materialia, 2017. **135**: p. 148-152.

12. Bendsoe, M.P. and O. Sigmund, *Topology optimization: theory, methods, and applications*. 2013: Springer Science & Business Media.

13. Sigmund, O. and K. Maute, *Topology optimization approaches.* Structural and Multidisciplinary Optimization, 2013. **48**(6): p. 1031-1055.

14. Wang, M.Y., X. Wang, and D. Guo, *A level set method for structural topology optimization.* Computer Methods in Applied Mechanics and Engineering, 2003. **192**(1–2): p. 227-246.

15. Allaire, G., F. Jouve, and A.-M. Toader, *Structural optimization using sensitivity analysis and a level-set method.* Journal of Computational Physics, 2004. **194**(1): p. 363-393.

16. Liu, J., et al., *Current and future trends in topology optimization for additive manufacturing.* Structural and Multidisciplinary Optimization, 2018. **57**(6): p. 2457-2483.

17. Baufeld, B., O. Van der Biest, and R. Gault, *Additive manufacturing of Ti–6Al–4V components by shaped metal deposition: microstructure and mechanical properties.* Materials & Design, 2010. **31**: p. S106-S111.

18. Mudge, R.P. and N.R. Wald, *Laser engineered net shaping advances additive manufacturing and repair.* Welding Journal-New York-, 2007. **86**(1): p. 44.

19. Palčič, I., et al., *Potential of laser engineered net shaping (LENS) technology.* Materials and Manufacturing Processes, 2009. **24**(7-8): p. 750-753.

20. Li, L., *Repair of directionally solidified superalloy GTD-111 by laser-engineered net shaping.* Journal of materials science, 2006. **41**(23): p. 7886-7893.

21. Koehler, H., et al., *Influence of laser reconditioning on fatigue properties of crankshafts.* Physics Procedia, 2011. **12**: p. 512-518.

22. Van Belle, L., G. Vansteenkiste, and J.C. Boyer, *Investigation of residual stresses induced during the selective laser melting process*, in *Key Engineering Materials*. 2013, Trans Tech Publ. p. 1828-1834.

23. Neugebauer, F., et al., *Multi Scale FEM Simulation for Distortion Calculation in Additive Manufacturing of Hardening Stainless Steel*, in *International Workshop on Thermal Forming an Welding Distortion, IWOTE 14*. 2014.

24. Radaj, D., *Heat effects of welding: temperature field, residual stress, distortion*. 2012: Springer Science & Business Media.

25. Frazier, W.E., *Metal additive manufacturing: a review.* Journal of Materials Engineering and Performance, 2014. **23**(6): p. 1917-1928.

26. Schoinochoritis, B., D. Chantzis, and K. Salonitis, *Simulation of metallic powder bed additive manufacturing processes with the finite element method: A critical review.* Proceedings of the Institution of Mechanical Engineers, Part B: Journal of Engineering Manufacture, 2017. **231**(1): p. 96-117.

27. Cheng, B., S. Shrestha, and K. Chou, *Stress and deformation evaluations of scanning strategy effect in selective laser melting.* Additive Manufacturing, 2016. **12**: p. 240-251.

28. Mukherjee, T., W. Zhang, and T. DebRoy, *An improved prediction of residual stresses and distortion in additive manufacturing.* Computational Materials Science, 2017. **126**: p. 360-372.

29. Vastola, G., et al., *Controlling of residual stress in additive manufacturing of Ti6Al4V by finite element modeling.* Additive Manufacturing, 2016. **12**: p. 231-239.

30. Heigel, J., P. Michaleris, and E. Reutzel, *Thermo-mechanical model development and validation of directed energy deposition additive manufacturing of Ti–6Al–4V.* Additive manufacturing, 2015. **5**: p. 9-19.

31. Gouge, M.F., et al., *Modeling forced convection in the thermal simulation of laser cladding processes.* The International Journal of Advanced Manufacturing Technology, 2015. **79**(1-4): p. 307-320.

32. Zhang, Y. and J. Zhang, *Finite element simulation and experimental validation of distortion and cracking failure phenomena in direct metal laser sintering fabricated component.* Additive Manufacturing, 2017. **16**: p. 49-57.

33. Denlinger, E.R., J.C. Heigel, and P. Michaleris, *Residual stress and distortion modeling of electron beam direct manufacturing Ti-6Al-4V.* Proceedings of the Institution of Mechanical Engineers, Part B: Journal of Engineering Manufacture, 2015. **229**(10): p. 1803-1813.

34. Moat, R., et al., *Residual stresses in laser direct metal deposited Waspaloy.* Materials Science and Engineering: A, 2011. **528**(6): p. 2288-2298.

35. Michaleris, P., *Modeling metal deposition in heat transfer analyses of additive manufacturing processes.* Finite Elements in Analysis and Design, 2014. **86**: p. 51-60.

36. Denlinger, E.R., J. Irwin, and P. Michaleris, *Thermomechanical modeling of additive manufacturing large parts.* Journal of Manufacturing Science and Engineering, 2014. **136**(6): p. 061007.

37. Ueda, Y., K. Fukuda, and M. Tanigawa, *New measuring method of three dimensional residual stresses based on theory of inherent strain (welding mechanics, strength & design).* Transactions of JWRI, 1979. **8**(2): p. 249-256.

38. Hill, M.R. and D.V. Nelson, *The inherent strain method for residual stress determination and its application to a long welded joint.* ASME-PUBLICATIONS-PVP, 1995. **318**: p. 343-352.

39. Yuan, M. and Y. Ueda, *Prediction of residual stresses in welded T-and I-joints using inherent strains.* Journal of engineering materials and technology, 1996. **118**(2): p. 229-234.

40. Deng, D., H. Murakawa, and W. Liang, *Numerical simulation of welding distortion in large structures.* Computer methods in applied mechanics and engineering, 2007. **196**(45): p. 4613-4627.

41. Murakawa, H., et al., *Applications of inherent strain and interface element to simulation of welding deformation in thin plate structures.* Computational Materials Science, 2012. **51**(1): p. 43-52.

42. Zhang, L., P. Michaleris, and P. Marugabandhu, *Evaluation of applied plastic strain methods for welding distortion prediction.* Journal of Manufacturing Science and Engineering, 2007. **129**(6): p. 1000-1010.

43. Michaleris, P., et al., *Evaluation of 2D, 3D and applied plastic strain methods for predicting buckling welding distortion and residual stress.* Science and Technology of Welding & Joining, 2006. **11**(6): p. 707-716.

44. Wang, Y.-X., et al., *Inherent strain method and thermal elastic-plastic analysis of welding deformation of a thin-wall beam.* Journal of Mechanics, 2008. **24**(04): p. 301-309.

45. Keller, N. and V. Ploshikhin. *New method for fast predictions of residual stress and distortion of AM parts*. in *Proceedings of Solid Freeform Fabrication (SFF) Conference*. 2014.

46. Huang, G., et al., *On The Creation of a New Finite Element Simulation Environment for Additive Manufacturing*, in *NAFEMS Americas Conference, Session Reviews, Session 7/1D*. 2016.

47. Keller, N., et al., *Distortion Compensation in Laser Beam Melting Processes*, in *MSTAM 2014 - Proceedings of the 1st International Symposium Materials Science and Technology of Additive Manufacturing*. 2015.

48. Afazov, S., et al., *Distortion Prediction and Compensation in Selective Laser Melting.* Additive Manufacturing, 2017. **17**: p. 15-22.

49. Fallah, V., et al., *Temporal development of melt-pool morphology and clad geometry in laser powder deposition.* Computational materials science, 2011. **50**(7): p. 2124-2134.

50. Marimuthu, S., et al., *Finite element modelling of substrate thermal distortion in direct laser additive manufacture of an aero-engine component.* Proceedings of the Institution of Mechanical Engineers, Part C: Journal of Mechanical Engineering Science, 2013. **227**(9): p. 1987-1999.

51. Ye, R., et al., *Numerical modeling of the thermal behavior during the LENS® process.* Materials Science and Engineering: A, 2006. **428**(1): p. 47-53.

52. Wang, L., et al., *Optimization of the LENS® process for steady molten pool size.* Materials Science and Engineering: A, 2008. **474**(1): p. 148-156.

53. Goldak, J., A. Chakravarti, and M. Bibby, *A new finite element model for welding heat sources.* Metallurgical transactions B, 1984. **15**(2): p. 299-305.

54. Anca, A., et al., *Computational modelling of shaped metal deposition.* International journal for numerical methods in engineering, 2011. **85**(1): p. 84-106.

55. Yang, Q., et al., *Finite element modeling and validation of thermomechanical behavior of Ti-6Al-4V in directed energy deposition additive manufacturing.* Additive Manufacturing, 2016. **12**: p. 169-177.

56. Joshi, S., et al., *Characterization of material properties and heat source parameters in welding simulation of two overlapping beads on a substrate plate.* Computational Materials Science, 2013. **69**: p. 559-565.

57. Chiumenti, M., et al., *Finite element modeling of multi-pass welding and shaped metal deposition processes.* Computer methods in applied mechanics and engineering, 2010. **199**(37): p. 2343-2359.

58. Ueda, Y., H. Murakawa, and N. Ma, *Welding deformation and residual stress prevention*. 2012: Elsevier.

59. Liang, X., et al. *A Modified Inherent Strain Method for Fast Prediction of Residual Deformation in Additive Manufacturing of Metal Parts*. in *Proceedings of Solid Freeform Fabrication (SFF) Conference*. 2017.

60. Niebling, F., A. Otto, and M. Geiger. *Analyzing the DMLS-process by a macroscopic FE-model*. in *Proc. of 13th Solid Freeform Fabrication Symposium*. 2002.

61. Nandy, J., H. Sarangi, and S. Sahoo. *Modeling of microstructure evolution in direct metal laser sintering: A phase field approach*. in *IOP Conference Series: Materials Science and Engineering*. 2017. IOP Publishing.

62. Mercelis, P. and J.-P. Kruth, *Residual stresses in selective laser sintering and selective laser melting.* Rapid Prototyping Journal, 2006. **12**(5): p. 254-265.

63. Fu, C. and Y. Guo, *Three-dimensional temperature gradient mechanism in selective laser melting of Ti-6Al-4V.* Journal of Manufacturing Science and Engineering, 2014. **136**(6): p. 061004.

64. Li, Z., et al., *A lightweight and support-free design method for selective laser melting.* The International Journal of Advanced Manufacturing Technology, 2017. **90**(9-12): p. 2943-2953.

65. Gong, X., T. Anderson, and K. Chou. *Review on powder-based electron beam additive manufacturing technology*. in *ASME/ISCIE international symposium on flexible automation*. 2012. American Society of Mechanical Engineers.

66. Sahoo, S. and K. Chou, *Phase-field simulation of microstructure evolution of Ti–6Al–4V in electron beam additive manufacturing process.* Additive manufacturing, 2016. **9**: p. 14-24.

67. Yan, W., et al., *Multiscale modeling of electron beam and substrate interaction: a new heat source model.* Computational Mechanics, 2015. **56**(2): p. 265-276.

68. Yan, W., et al., *Data-driven multi-scale multi-physics models to derive process–structure–property relationships for additive manufacturing.* Computational Mechanics, 2018. **61**(5): p. 521-541.

69. Denlinger, E.R., et al., *Effect of inter-layer dwell time on distortion and residual stress in additive manufacturing of titanium and nickel alloys.* Journal of Materials Processing Technology, 2015. **215**: p. 123-131.

70. Hussein, A., et al., *Finite element simulation of the temperature and stress fields in single layers built without-support in selective laser melting.* Materials & Design (1980-2015), 2013. **52**: p. 638-647.

71. Lundbäck, A. and L.-E. Lindgren, *Modelling of metal deposition.* Finite Elements in Analysis and Design, 2011. **47**(10): p. 1169-1177.

72. Li, C., J. Liu, and Y. Guo. *Efficient multiscale prediction of cantilever distortion by selective laser melting*. in *Annual International Solid Freeform Fabrication Symposium*. 2016.

73. Li, C., et al., *A multiscale modeling approach for fast prediction of part distortion in selective laser melting.* Journal of Materials Processing Technology, 2016. **229**: p. 703-712.

74. Alvarez, P., et al., *Computationally efficient distortion prediction in Powder Bed Fusion Additive Manufacturing.* International Journal of Engineering Research & Science, 2016. **2**(10): p. 39-46.

75. Setien, I., et al., *Empirical methodology to determine inherent strains in additive manufacturing.* Computers & Mathematics with Applications, 2018. **78**(7): p. 2282-2295.

76. Liang, X., et al., *A modified method for estimating inherent strains from detailed process simulation for fast residual distortion prediction of single-walled structures fabricated by directed energy deposition.* Additive Manufacturing, 2018. **23**: p. 471-486.

77. Peng, H., et al., *Fast prediction of thermal distortion in metal powder bed fusion additive manufacturing: Part 2, a quasi-static thermo-mechanical model.* Additive Manufacturing, 2018. **22**: p. 869-882.

78. Levine, L., et al., *Outcomes and Conclusions from the 2018 AM-Bench Measurements, Challenge Problems, Modeling Submissions, and Conference.* Integrating Materials and Manufacturing Innovation, 2020. **9**(1): p. 1-15.

79. Hussein, A., et al., *Advanced lattice support structures for metal additive manufacturing.* Journal of Materials Processing Technology, 2013. **213**(7): p. 1019-1026.

80. Strano, G., et al., *A new approach to the design and optimisation of support structures in additive manufacturing.* The International Journal of Advanced Manufacturing Technology, 2013. **66**(9-12): p. 1247-1254.

81. Cheng, L., et al., *On utilizing topology optimization to design support structure to prevent residual stress induced build failure in laser powder bed metal additive manufacturing.* Additive Manufacturing, 2019. **27**: p. 290-304.

82. Jiang, J., X. Xu, and J. Stringer, *Support structures for additive manufacturing: a review.* Journal of Manufacturing and Materials Processing, 2018. **2**(4): p. 64.

83. Denlinger, E.R., et al., *Thermomechanical model development and in situ experimental validation of the Laser Powder-Bed Fusion process.* Additive Manufacturing, 2017. **16**: p. 73-80.

84. Parry, L., I. Ashcroft, and R.D. Wildman, *Understanding the effect of laser scan strategy on residual stress in selective laser melting through thermo-mechanical simulation.* Additive Manufacturing, 2016. **12**: p. 1-15.

85. Ali, H., H. Ghadbeigi, and K. Mumtaz, *Effect of scanning strategies on residual stress and mechanical properties of Selective Laser Melted Ti6Al4V.* Materials Science and Engineering: A, 2018. **712**: p. 175-187.

86. Chen, Q., et al., *An inherent strain based multiscale modeling framework for simulating part-scale residual deformation for direct metal laser sintering.* Additive Manufacturing, 2019. **28**: p. 406-418.

87. Liang, X., et al., *Modified inherent strain method for efficient prediction of residual deformation in direct metal laser sintered components.* Computational Mechanics, 2019. **64**(6): p. 1719-1733.

88. Hollister, S.J. and N. Kikuchi, *A comparison of homogenization and standard mechanics analyses for periodic porous composites.* Computational Mechanics, 1992. **10**(2): p. 73-95.

89. Bendsøe, M.P. and N. Kikuchi, *Generating optimal topologies in structural design using a homogenization method.* Computer methods in applied mechanics and engineering, 1988. **71**(2): p. 197-224.

90. Bensoussan, A., J.-L. Lions, and G. Papanicolaou, *Asymptotic analysis for periodic structures*. Vol. 374. 2011: American Mathematical Soc.

91. Cheng, L., J. Bai, and A.C. To, *Functionally graded lattice structure topology optimization for the design of additive manufactured components with stress constraints.* Computer Methods in Applied Mechanics and Engineering, 2019. **344**: p. 334-359.

92. Terada, K., et al., *A method of two-scale thermo-mechanical analysis for porous solids with micro-scale heat transfer.* Computational Mechanics, 2010. **46**(2): p. 269-285.

93. Gibson, L.J. and M.F. Ashby, *Cellular solids: structure and properties*. 1999: Cambridge university press.

94. Cheng, L., et al., *Efficient Design Optimization of Variable-Density Cellular Structures for Additive Manufacturing: Theory and Experimental Validation.* Rapid Prototyping Journal, 2017. **23**(4): p. 660-677.

95. Cheng, L., et al., *Coupling lattice structure topology optimization with design-dependent feature evolution for additive manufactured heat conduction design.* Computer Methods in Applied Mechanics and Engineering, 2018. **332**: p. 408-439.

96. Zhang, Y., S. Shang, and S. Liu, *A novel implementation algorithm of asymptotic homogenization for predicting the effective coefficient of thermal expansion of periodic composite materials.* Acta Mechanica Sinica, 2017. **33**(2): p. 368-381.

97. Cheng, G.-D., Y.-W. Cai, and L. Xu, *Novel implementation of homogenization method to predict effective properties of periodic materials.* Acta Mechanica Sinica, 2013. **29**(4): p. 550-556.

98. Deng, J., J. Yan, and G. Cheng, *Multi-objective concurrent topology optimization of thermoelastic structures composed of homogeneous porous material.* Structural and Multidisciplinary Optimization, 2013. **47**(4): p. 583-597.

99. ASTM International, *ASTM E8/E8M-16a Standard Test Methods for Tension Testing of Metallic Materials*. 2016, ASTM International: West Conshohocken, PA.

100. Han, Q., et al., *Manufacturability of AlSi10Mg overhang structures fabricated by laser powder bed fusion.* Materials & Design, 2018. **160**: p. 1080-1095.

101. Lefky, C.S., et al., *Dissolvable Supports in Powder Bed Fusion-Printed Stainless Steel.* 3D Printing and Additive Manufacturing, 2017. **4**(1): p. 3-11.

102. Tran, H.T., et al., *A New Method for Predicting Cracking at the Interface between Solid and Lattice Support During Laser Powder Bed Fusion Additive Manufacturing.* Additive Manufacturing, 2020. **32**: p. 101050.

103. Denlinger, E.R., et al., *Thermal modeling of Inconel 718 processed with powder bed fusion and experimental validation using in situ measurements.* Additive Manufacturing, 2016. **11**: p. 7-15.

104. Irwin, J. and P. Michaleris, *A line heat input model for additive manufacturing.* Journal of Manufacturing Science and Engineering, 2016. **138**(11): p. 111004.

105. Siewert, M., et al., *Validation of Mechanical Layer Equivalent Method for simulation of residual stresses in additive manufactured components.* Computers & Mathematics with Applications, 2018. **78**(7): p. 2407-2416.

106. Bugatti, M. and Q. Semeraro, *Limitations of the Inherent Strain Method in Simulating Powder Bed Fusion Processes.* Additive Manufacturing, 2018. **23**: p. 329-346.

107. Lu, Q., E. Beauchesne, and T. Liszka, *Enhancements to the inherent strain method for Additive Manufacturing analysis.* International Journal for Multiscale Computational Engineering, 2019. **17**(1): p. 65-81.

108. Hajializadeh, F. and A. Ince, *Short review on modeling approaches for metal additive manufacturing process.* Material Design & Processing Communications, 2020. **2**(2): p. e56.

109. Mayer, T., et al., *Simulation and validation of residual deformations in additive manufacturing of metal parts.* Heliyon, 2020. **6**(5): p. e03987.

110. Li, M., et al., *Dimensional Deviation Management for Selective Laser Melted Ti6Al4V Alloy Blade.* Frontiers in Materials, 2020. **7**(42): p. 1-10.

111. Li, J. and Q. Wang, *An analytical computation of temperature field evolved in directed energy deposition.* Journal of Manufacturing Science and Engineering, 2018. **140**(10).

112. Li, C., et al., *Estimation of part-to-powder heat losses as surface convection in laser powder bed fusion.* Additive Manufacturing, 2019. **26**: p. 258-269.

113. Soylemez, E., E. Koç, and M. Coşkun, *Thermo-mechanical simulations of selective laser melting for AlSi10Mg alloy to predict the part-scale deformations.* Progress in Additive Manufacturing, 2019. **4**(4): p. 465-478.

114. Malmelöv, A., A. Lundbäck, and L.-E. Lindgren, *History Reduction by Lumping for Time-Efficient Simulation of Additive Manufacturing.* Metals, 2020. **10**(1): p. 58.

115. Liang, X., et al., *Inherent strain homogenization for fast residual deformation simulation of thin-walled lattice support structures built by laser powder bed fusion additive manufacturing.* Additive Manufacturing, 2020. **32**: p. 101091.